Simulated mid and early Holocene climate in ECHAM6-FESOM: focus on North Atlantic variability

DISSERTATION
zur Erlangung des akademischen Grades eines
Doktor der Naturwissenschaften
— Dr. rer. nat. —

Vom Fachbereich für Physik und Elektrotechnik,
Universität Bremen

von

Xiaoxu Shi

• Supervisor: Prof. Dr. Gerrit Lohmann

Eingereicht am: Juni.20.2016

Erklärung

Hiermit versichere ich, dass ich die vorliegende Arbeit selbstständig verfasst und keine anderen als die angegebenen Quellen und Hilfsmittel benutzt habe, dass alle Stellen der Arbeit, die wörtlich oder sinngemäß aus anderen Quellen übernommen wurden, als solche kenntlich gemacht sind und dass die Arbeit in gleicher oder ähnlicher Form noch keiner Prüfungsbehörde vorgelegt wurde.

Bremerhaven, den Juni.20.2016 .....

Abstract

In the first part of the thesis, changes of the Atlantic meridional overturning circulation (AMOC) in the mid-Holocene compared to the pre-industrial state are explored in different coupled climate models. Using time-slice integrations by a newly developed global finite-element model ECHAM6-FESOM with unstructured mesh and high resolution, our simulations show an enhanced mid-Holocene AMOC, accompanied by an increase in the ocean salinity over regions of deep water formation. We identify two different processes affecting the AMOC: 1) a more positive phase of North Atlantic Oscillation (NAO) increases water density over the Labrador Sea through anomalous net evaporation and surface heat loss; 2) a decreased import of sea ice from the Arctic causes a freshwater reduction in the northern North Atlantic Ocean. Using the coupled model ECHAM6-MPIOM in T63GR15 and T31GR30 grids, we find that the simulated AMOC is strongly affected by the model resolution. In detail, stronger-than-present mid-Holocene AMOC is revealed by simulations with the T63GR15 grid, which resembles the result of ECHAM6-FESOM, while a decline of the mid-Holocene AMOC is simulated by the low resolution model with the T31GR30 grid. Such discrepancy can be attributed to different changes in Labrador Sea density which is mainly affected by 1) NAO-induced net precipitation, 2) freshwater transport from the Arctic Ocean, and 3) the strength of AMOC itself. Finally, we analyzed available coupled climate models showing a diversity of responses of AMOC to mid-Holocene forcings, most of which reveal positive AMOC changes related to northern high latitudes salinification.

Sensitivity of the simulated climate to the early-Holocene (9k) insolation, greenhouse gases (GHGs) and topography is examined in the second part of the thesis, by performing timeslice experiments under pre-industrial and 9k regimes using ECHAM6-FESOM. Under the early-Holocene orbit and GHGs, the ECHAM6-FESOM simulation shows a warming in boreal summer and a cooling in boreal winter from over mid and high latitudes compared to pre-industrial, with amplification over the continents; as well as a reduction of sea ice in the Arctic and Southern Oceans. A reduced sea ice transport through the Fram Strait leads to a stronger-than-present Atlantic Meridional Overturning Circulation (AMOC) in the early-Holocene. Including the early-Holocene topography and continental ice sheet over North America leads to an additional re-

gional cooling year-round. The resulted enhanced sea ice thermodynamic production over Baffin Bay and North Atlantic subpolar gyre is the cause for a more saline surface over the region of deep water formation. There are big discrepancies in the oceanic responses to different locations of freshwater discharge. Laurentide Ice Sheet (LIS) coastal melting only leads to a freshening over the Gulf Stream and Canary Current, with no meltwater advection to the deep water formation sites, therefore not affecting the strength of the thermohaline circulation. In contrast, adding freshwater into the Labrador Sea produces a significant decrease in ocean salinity over the North Atlantic region from sea surface to 200 m depth, contributing to a decline of the Atlantic meridional overturning circulation (AMOC). All early-Holocene experiments reveal a change of the westerlies over the North Atlantic section, accompanied by a more positive North Atlantic Oscillation (NAO) phase, which is led by the corresponding divergence anomalies of the Eliassen-Palm (E-P) flux. The enhanced westerly wind at 50 °N provides a barrier which prevents the Arctic cold air from invading into the lower latitudes. This circulation change in the atmosphere leads to less frequent episodes of blocking patterns which further results in decreased cold surges over most parts of the Northern Hemisphere continents, in particular the Europe and Asia in the early-Holcene compared to pre-industrial. Finally, the reduced cold air outbreak events, together with a relatively dry atmospheric condition, are the causes for a reduced snowfall over Europe and Asia.

Another aim of the thesis (the third part) is to examine to what degree the area-thickness distribution of new ice formed in open water affects the ice and ocean properties. Two sensitivity experiments are performed which modify the horizontal-to-vertical aspect ratio of open-water ice growth. The resulting changes in the Arctic sea-ice concentration strongly affect the surface albedo, the ocean heat release to the atmosphere, and the sea-ice production. Furthermore, our simulations show a positive feedback mechanism among the Arctic sea ice, the Atlantic Meridional Overturning Circulation (AMOC), and the surface air temperature in the Arctic, as the Fram Strait sea ice import influences the freshwater budget in the North Atlantic Ocean. Anomalies in sea-ice transport lead to changes in sea surface properties of the North Atlantic and the strength of AMOC. For the Southern Ocean, the most pronounced change is a warming along the Antarctic Circumpolar Current (ACC), especially for the Pacific sector. Another insight of this study lies on the improvement of FESOM-ECHAM6. FESOM-ECHAM6 is a newly developed global climate model with an unstructured mesh and multi-resolution. It has relatively high ability for producing many aspects of the observed climate, but also has shortcomings when simulating the subpolar sea-ice boundary in the Northern Hemisphere and the strength of AMOC. We find that such disadvantages can be improved by tuning the process of open-water ice growth, which strongly influences the sea ice concentration in the marginal ice zone and affects the North Atlantic circulation through regulating the import of Arctic sea ice volume. In reality, the distribution of new ice on open water relies on many uncertain parame-

ters, for example, surface albedo, wind speed and ocean currents. Knowledge of the detailed processes is currently too crude for those processes to be implemented realistically into models. Our sensitivity experiments indicate a pronounced uncertainty related to open-water sea ice growth which could significantly affect the climate system sensitivity.

Contents

1 Introduction

There are multiple lines of evidence that variations in the North Atlantic meridional overturning circulation (AMOC) is a major source of decadal and multidecadal variability in the climate system. Prominently, this is manifested in the sea surface temperature and salinity over North Atlantic. An abundance of studies [e.g., *Schlesinger and Ramankutty*, 1994; *Rühlemann et al.*, 2004; *Knight et al.*, 2005; *Dima and Lohmann*, 2007; *Zhang*, 2007, 2008; *Chylek et al.*, 2009] provided rigorous evidence of the widely hypothesized link between the AMOC and the Northern Hemisphere mean surface temperature, as well as the Arctic surface air temperature (SAT). Using observational data, *Polyakov et al.* [2005] demonstrated that temperature and salinity from the 0-300 m to 1000-3000 m layers vary in opposition: prolonged periods of cooling and freshening (warming and salinification) in one layer are generally associated with opposite tendencies in the other layer, which may be associated with a change in the strength of AMOC. Parker et al. (2007) analyzed modeling results and represented a mechanism feedback between weak (strong) AMOC and cooler (warmer) North Atlantic.

The mid-Holocene (6k) is one of the key times in the past. The most prominent difference between 6k and present arises from the orbital configuration, which leads to an increase in insolation in the Northern Hemisphere (NH) and a decrease in the tropical and subtropical Southern Hemisphere [*Lohmann et al.*, 2013]. Reproducing AMOC of 6k is not only scientifically interesting in itself, but also of crucial importance to increase our understanding of the climate responses to different condition states. So far, some efforts have been made to simulate the 6k AMOC, most of which indicated an decrease

in mid-Holocene AMOC compared to its present phase. For example, *Ganopolski et al.* [1998] and *Otto-Bliesner et al.* [2006] produced a weaker-than-present AMOC for the mid-Holocene with the climate models CLIMBER and CCSM3 respectively. *Wei and Lohmann* [2012] simulated a difference of -2 Sv between the AMOC of mid-Holocene and pre-industrial using the coupled model ECHAM5-MPIOM with a coarse resolution grid. The same result is also found by *Fischer and Jungclaus* [2010] who performed similar simulations using ECHAM5-MPIOM with a different vegetation code and without the implementation of 6k greenhouse gases. *Zheng and Yu* [2013] simulated the climate condition of 6k with different versions of the coupled model FGOALS, and found a weakened (enhanced) AMOC during 6k with old (new) version of the model. Furthermore, different results are shown by *Renssen et al.* [2005] who demonstrated a long-term reduction from the Holocene to present in maximum meridional overturning with the model ECBilt-CLIOVECODE.

Given above, most previous studies illustrated a weaker-than-present 6k AMOC, which is generally associated with a warming and freshening in the upper layer of the North Atlantic Ocean, leading to a decrease in water mass density over the deep water formation regions in the Nordic Sea. However, there are reconstruction records suggesting an increase of ocean salinity over those regions [e.g., *de Vernal and Hillaire-Marcel*, 2006; *Came et al.*, 2007; *Thornalley et al.*, 2009; *Rasmussen and Thomsen*, 2010]. Besides, proxy-based observational evidence shows a brief decline in meridional overturning circulation from the mid-Holocene to present [*McManus et al.*, 2004].

In the present paper, we are specifically interested in the sensitivity of AMOC to different model components and resolutions. The importance of model resolution has been described in several studies [e.g., *Boville*, 1991; *Buizza et al.*, 1998]. So far the simulations of the mid-Holocene AMOC were based on coarse resolution models, and in the convection areas the water masses might not be well represented. Utilization of a newly developed global climate model ECHAM6-FESOM with unstructured mesh and high resolution [*Sidorenko et al.*, 2014] allows a more comprehensive simulation for examining the mid-Holocene AMOC, and for exploring the mechanism behind the AMOC change. Furthermore, we investigate the response of AMOC to model resolutions by analyzing results of the climate model ECHAM6-MPIOM with two different resolutions.

The early-Holocene (11.5 to 7 ka B.P.) in our present interglacial period is marked by pronounced seasonality and the presence of the Laurentide ice sheet (LIS). Even though recent data syntheses have improved our understanding of reconstructed data for paleo-periods [*Bigelow et al.*, 2003; *Mügler et al.*, 2010], it is still a difficulty to have a comprehensive view of the early-Holocene climate change due to the discrepancies between the various records *Bradley* [1990]. Numerical climate model simulations can be used to improve our understanding of the mechanism behind the early-Holocene climatic changes and to provide a coherent and physically consistent overview of the climate on all timescales.

One of the main applications of climate models has been to explore the climatic effects of the changed orbital parameters of the Earth. *Kutzbach* [1981] finds an intensified continent-scale monsoon circulation when applying estimated early-Holocene precession and obliquity of the earth. Using an atmospheric model coupled to a mixed layer ocean, *Mitchell et al.* [1988] find Northern Hemisphere warming throughout the year. *Kutzbach and Gallimore* [1988] perform a similar simulation, that indicates warmer continents in summer and intensified northern summer monsoons at early-Holocene compared to the present. Simulations with climate models have shown that the wetter conditions at the Sahel and Sahara regions were probably caused by changes in Earth's orbital parameters that increased the amplitude of the seasonal cycle of solar radiation in the Northern Hemisphere [*Kutzbach et al.*, 1996]. In a transient simulation of the Holocene climate with ECBilt orbital forcing, *Weber* [2001] observes that summer warming over land induces a stronger monsoon circulation in the subtropics and associated adjustment in precipitation patterns. An Earth system model of intermediate complexity, MoBidiC, has been used to simulate the transient variations in continental temperature, sea-surface temperature (SST), thermohaline circulation and sea-ice cover over the last 9000 years [*Crucifix et al.*, 2002]. Synthetic glacier length records are generated for the Holocene epoch using a process-based glacier model coupled to the intermediate-complexity climate model ECBilt, forced by the insolation change due to variations in the Earth's orbital parameters *Weber and Oerlemans* [2003]; *Weber et al.* [2004]. *Carlson et al.* [2008] suggests that increased ablation due to enhanced early Holocene boreal summer insolation was the predominant cause of Laurentide ice-sheet (LIS) retreat.

Another important impacting factor is the greenhouse gases (GHGs). The response of the climate at high northern latitudes to slowly changing external forcings and atmospheric CO2 and CH4 content was studied in a transient simulation with the coupled model ECBilt-CLIO-VECODE [*Renssen et al.*, 2005], which reveals a decrease in global mean annual temperatures, a reduction in summer precipitation and an expansion of sea-ice cover from early-Holocene to the present. A reduced ENSO intensity in the early-Holocene, in agreement with paleoclimate record, is simulated by FOAM [*Liu et al.*, 2000].

Positioned in mid-latitude of North Hemisphere, the LIS is of crucial importance to the climate conditions. The impact of continental ice sheets on the climate change is potentially important in climate-sensitivity studies *Oerlemans* [1980]; *Zhang et al.* [2014]; *Liu et al.* [2014]. Moreover, the effect of LIS meltwater forcing on the early Holocene climate is investigated with a variety of coupled models. For example, a fix amount of freshwater into the Labrador Sea at three different rates is applied in a global coupled atmosphere-sea ice-ocean model model ECBilt-CLIO-VECODE by [*Renssen et al.*, 2002], the results demonstrated that several types of recovery may exist with the same kind of meltwater perturbation. Among their simulations, a scenario with a 20-year pulse produced a model response in agreement with proxy records [*Renssen et al.*, 2009, 2001], a more gradual release (0.03 Sv) as proposed by *Klitgaard-Kristensen et al.* [1998] results in no significant thermohaline circulation change *Renssen et al.* [2001]. A freshwater forcing of 0.09 Sv is prescribed by *Wei and Lohmann* [2012] into the North Atlantic Ocean between 40 °N and 60 °N, leading to a significant surface cooling and decline of the Atlantic meridional overturning circulation. More recently, *Zhang et al.* [2015] performed transient simulations from the early-Holocene to present using the climate model LOVECLIM with varying freshwater flux applied, indicating that the Holocene temperature evolution varies between different regions. *Liu et al.* [2014] reported that climate models simulate a robust global annual mean warming in the Holocene, mainly in response to rising CO2 and the retreat of ice sheets.

Most of the above studies focus on the effects of the redistributed solar radiation and GHGs, and the influence of the orbital change. Some of them investigate the respective role of early-Holocene topography and LIS meltwater flux on the simulated climate [*Mitchell et al.*, 1988; *Wei and Lohmann*, 2012; *Renssen et al.*, 2005], however, with a

relatively coarse resolution applied. The focus of previous studies is mainly on processes of seasonal to Millennial time scale, therefore there is a lack of studies on small-time scale climate movements, for example the transient eddy flux, blocking event and cold air outbreak. To fill the above mentioned gaps in our understanding of early-Holocene climate variability, we have therefore applied a finite-element climate model ECHAM6-FESOM with unstructured mesh and high resolution to simulate the early-Holocene climate. In our experiment, we have prescribed the early-Holocene solar insolation the GHGs content. We also discuss the results of a sensitivity experiment in which we investigate the effect of the early-Holocene topography on the early-Holocene climate. Two different types of hosing experiments are performed by adding freshwater flux into either the LIS coastal region or the Labrador Sea. In addition, daily output is analyzed to examine the Eliassen-Palm flux which affects the atmospheric circulation, and the Northern Hemisphere cold air outbreak which influences the winter climate of North America and Eurasia. To our knowledge, this is the first early-Holocene simulation with a triangle-mesh high-resolution climate model.

Sea ice is one of the most visible indicators of our changing climate owing to its reflecting and insulating properties [*IPCC*, 2013]. On one hand, sea ice reflects part of the incoming solar radiation due to its high surface albedo; on the other hand, sea ice reduces the heat exchange between the atmosphere and the ocean. Therefore, the concentration of sea ice regulates the air-ocean interaction and thus plays an important role in the climate system. It has been argued that a reduction in the high-latitude ice concentration has impacts on the atmosphere and ocean characteristics [e.g., *Royer et al.*, 1990; *Deser et al.*, 2010; *Semmler et al.*, 2012]. For example, *Deser et al.* [2010] used an atmospheric general circulation model (CAM3) to investigate the atmospheric response to projected Arctic sea ice loss at the end of the 21st century, and found an increase in snowfall over North America, Asia and the northern part of Europe. *Semmler et al.* [2012] used the atmospheric general circulation model EC-EARTH-IFS to carry out sensitivity experiments with reduced ice cover, and found negative sea level pressure (SLP) anomalies over the western Arctic and positive anomalies over Siberia, affecting surface temperatures over Europe. An extreme scenario experiment with no Arctic sea ice in winter was conducted by *Royer et al.* [1990] using an atmosphere stand-alone model; they found strongly enhanced surface latent and sensible heat fluxes in

winter, and corresponding effects on temperature and circulation.

Given these results, there is no doubt that ice concentration is crucial to any realistic modeling of the Earth's climate. Changes in sea ice conditions are affected by processes involving complex feedback mechanisms, such as ocean-atmosphere interactions, surface albedo and desalination processes of sea ice. Since some processes related to sea ice conditions are too complicated or not sufficiently understood to be resolved by the models' governing equations, it is necessary to apply parameterizations to empirically describe such processes. However, the representation of some of these factors in numerical models is still subject to large uncertainties [e.g., *Notz*, 2012]. One of these uncertain parameterizations is the open-water ice growth, which is a key element contributing to sea ice concentration. During the ice accretion period, new ice volume generated on open water is distributed into growth in vertical and horizontal directions, contributing to both ice thickness and concentration. So far much effort has been made to simulate open-water ice growth. *Hibler* [1979] introduced a demarcation between thin and thick ice at $h_0 = 0.5m$. It is assumed that in the freezing case, the fraction of open water is allowed to decay exponentially with a time constant of $h_0/\dot{h}_{ow}$, with $\dot{h}_{ow}$ being the growth rate of ice on open water. Reasoning and sensitivity studies were presented by *Mellor and Kantha* [1989], who suggested an aspect ratio of $\Phi_F = 4$ to divide open-water ice growth between increase in ice thickness and in ice area. *Dorn et al.* [2009] parameterize the increase rate of ice concentration due to freezing on open water based on a reference thickness for lateral melting. In a similar way, *Vancoppenolle et al.* [2010] used a thickness of $0.05 < h_0 < 0.15$ m in the model LIM3 to limit new ice in open water when transforming new ice volume to thickness and concentration. However, it is a great challenge to simulate the open-water ice growth since this process is only partly understood and currently not realistically represented in models [*Notz*, 2012], therefore there is room for calibration and improvement. The new ice formed on open water can be parameterized as in the left panel of Fig. 1.1 (with relatively less thickness and more concentration) or as the right panel (with more thickness but less concentration, i.e., more open water).

One of the main purposes of this study is to investigate to what extent the lateral-vertical ice growth ratio within open water can affect the simulation results, which has only been done mostly in stand-alone sea ice models [e.g., *Hibler*, 1979; *Fichefet and*

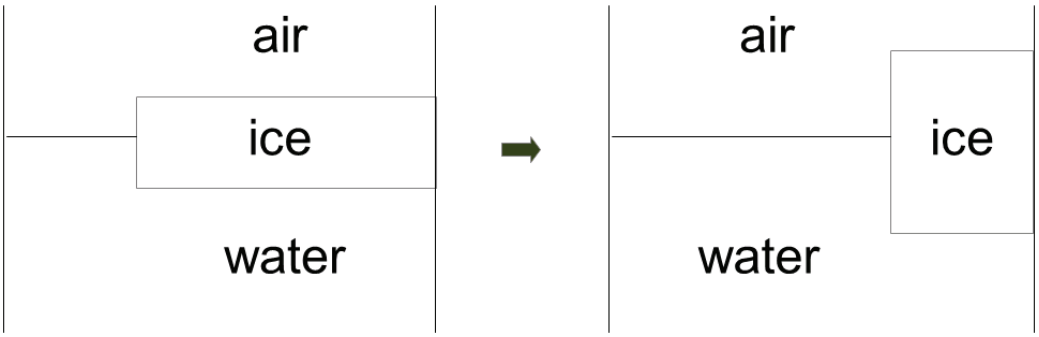

Fig. 1.1: *Two different kinds of newborn ice on open water. Left panel shows ice with actual thickness h_1 and area A_1, right panel shows ice with actual thickness h_2 and area A_2 ($h_2 > h_1, A_2 < A_1$), and $h_1 A_1 = h_2 A_2$.*

Maqueda, 1997; *Biggs et al.*, 2000; *Wang et al.*, 2010; *Smedsrud*, 2011]. For example, when the aspect ratio is large enough for producing a lead-free ice region, a drastical reduction in sea ice volume is given by the LIM2 model [*Fichefet and Maqueda*, 1997]. Using the same model, *Wang et al.* [2010] reveals simple relations between ice conditions and the lateral-vertical ice growth ratio. Furthermore, there are studies on the interaction of Arctic sea ice with climate states over lower latitudes [e.g., *Aagaard and Carmack*, 1989; *Goosse and Fichefet*, 1999]. To sum up, we have previous understanding of 1) how open-water ice growth parameterization affects the sea ice propertes, and 2) how changes in ice volume affect global patterns in the ocean and in the atmosphere. In the present paper, for the first time we look at these two things in combination in a high resolution climate model.

For such purpose, we modify the horizontal ice accretion on open water in a coupled climate model FESOM-ECHAM6 [*Sidorenko et al.*, 2014]: when ice forms over sea water, the added ice concentration becomes larger (smaller), while, the increase in ice thickness is (smaller) larger (Fig. 1.1). The uncertainty related to this process is studied in ECHAM6-FESOM.

Content of the thesis

The structure of the thesis is organized in 3 main chapters 3-5, besides the general introduction (chapter 1), model description (chapters 2 and the conclusions and future

perspectives (chapter 6).

Chapter 2:

Chapter 2 introduces the climate models used in my PhD work and the experimental design.

Chapter 3:

Chapter 3 examines the simulated response of the mid-Holocene Atlantic Meridional Overturning Circulation in ECHAM6-FESOM/MPIOM.

Chapter 4:

Chapter 4 presents the North Hemisphere oceanic and atmospheric circulation under different early-Holocene regimes in ECHAM6-FESOM.

Chapter 5:

The aim of chapter 5 is to investigate the sensitivity of simulated climate to lateral-vertical ratio of open-water ice growth.

2 Model and data description

2.1 ECHAM6-FESOM

ECHAM6-FESOM is a newly developed global coupled climate model which has been established at the Alfred Wegener Institute (AWI). The ocean-sea ice component is the Finite Element Sea Ice-Ocean Model (FESOM) [*Danilov et al.*, 2004; *Timmermann et al.*, 2009; *Sidorenko et al.*, 2011; *Wang et al.*, 2013; *Sidorenko et al.*, 2014] which is discretized on a triangular grid with a continuous conforming representation of model variables, whereas the atmospheric module is represented by the general circulation model ECHAM6 [*Stevens et al.*, 2013], mainly developed by the Max Planck Institute for Meteorology (MPI-M).

ECHAM6 is the sixth generation of the atmospheric general circulation model ECHAM, focusing on the coupling between diabatic processes, which is often associated with small-scale fluid dynamics, and large-scale circulations. The model is branched from an early release of the European Center (EC) for Medium Range Weather Forecasts (ECMWF) model [*Roeckner et al.*, 1989]. Like most models, the dynamics of ECHAM6 is based on the hydrostatic primitive equations (HPEs) with traditional approximation. Gaussian grid is used in the model to calculate non-linear equation terms and some physical representation. The boundary layer and turbulence parameterization is based on the eddy diffusivity/viscosity approach. Momentum transport arising from boundary effects is parameterized using the subgrid orography scheme as described by *Lott* [1999]. Subgrid-scale cloudiness is represented using the assumed humidity distribution

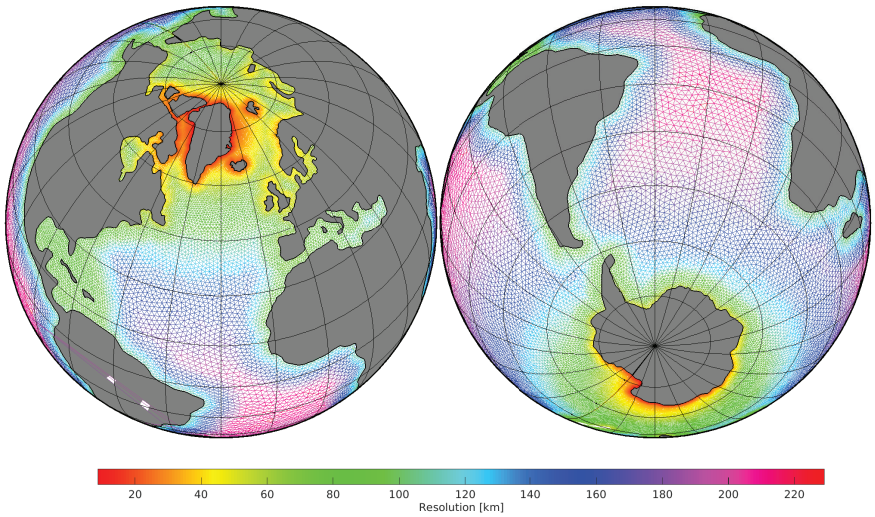

Fig. 2.1: *FESOM mesh resolution applied in our experiments, with higher resolution along the coastlines and at polar regions.*

function scheme developed by *Sundqvist et al.* [1989]. Radiative transfer in ECHAM6 is represented using the rapid radiation transfer [*Iacono et al.*, 2008]. ECHAM6 also includes a Land-Surface Model (JSBACH) which includes dynamic vegetation with 12 plant functional types and two types of bare surface [*Loveland et al.*, 2000; *Raddatz et al.*, 2007]. ECHAM6-FESOM is configured on T63L47 grid for the atmosphere, which is 1.9° degree for horizontal resolution and 47 levels in vertical direction.

FESOM is a hydrostatic ocean circulation model based on the finite-element approach and designed to work on unstructured meshes, therefore is different in many important ways from models formulated on regular meshes. The mesh nodes are vertically aligned to avoid difficulties in resolving the hydrostatic balance. The model uses variable resolution from about 200 km in the open ocean to 20 km along coastlines as shown in Fig. 2.1, with 40309 surface nodes. A no-slip boundary condition along the coast is implemented in the model. Additionally, the mesh is refined in the equatorial belt to about 40 km. There are 46 vertical levels. Surface stress and buoyancy fluxes are derived from the ice-ocean coupling. The FESOM sea ice component

is a dynamic-thermodynamic sea ice model with the *Parkinson and Washington* [1979] thermodynamics. The model consists of subgrid-scale processes based on *Redi* [1982], a so-called zero-layer approach of [*Semtner*, 1976] and a submodel of ice dynamics according to an elastic-viscous-plastic rheology [*Hunke and Dukowicz*, 1997]. The model also includes a prognostic snow layer [*Owens and Lemke*, 1990]. The paramerization of snow-ice conversion is based on *Leppäranta* [1983]. FESOM model has been validated in *Timmermann et al.* [2009] and *Scholz et al.* [2013].

2.2 ECHAM6-MPIOM

Besides ECHAM6-FESOM, we also conduct experiments using the coupled model ECHAM6-MPIOM [*Stevens et al.*, 2013; *Jungclaus et al.*, 2013]. The ocean general circulation model MPIOM is based on the primitive equations with representation of dynamic and thermodynamic processes. MPIOM uses a curvilinear orthogonal grid which allows for a variety of configurations. A detailed description is given by *Marsland et al.* [2003]. The coupled model has been developed for many resolutions, for example, the atmosphere component can be configured on T31, T63, T127 and T255 grids, associated with Gaussian grids of approximately 3°, 1.9°, 0.95° and 0.47° resolution, respectively [*Stevens et al.*, 2013]. In terms of MPIOM, there are several grid options such as GR30, GR15, TP04 and TP6M etc., with resolution varying from about 3° to as high as 0.1° [*Marsland et al.*, 2003; *Storch et al.*, 2012]. In addition, ECHAM6-MPIOM a subsystem model for land and vegetation JSBACH [*Reick et al.*, 2013; *Schneck et al.*, 2013]. In this study, ECHAM6-MPIOM applies 31 and 40 vertical levels for the atmosphere and ocean, respectively.

2.3 Other CMIP5 model data used

We process pre-industrial and mid-Holocene climatology data from other 9 climate models in the CMIP5 archive [*Taylor et al.*, 2012] to have a further view of the AMOC change, with a focus on the ECHAM6-MPIOM model of T63GR15 grid. Detailed information of the 10 models we used here is summarized in Table 2.

Table 2.1: *List of CMIP5 model data*

Name	Reference	Resolution (atmosphere, ocean)
BCC-CSM1-1	*Wu et al.* [2008, 2010]	($1° \times 1°$, $1.5° \times 1.5°$)
CCSM4	*Gent et al.* [2011]	($1° \times 1°$, $0.5° \times 1.1°$)
CNRM-CM5	*Voldoire et al.* [2013]	($1.4° \times 1.4°$, $1° \times 1°$)
CSIRO-Mk3-6-0	*Collier et al.* [2011]	($1.9° \times 1.9°$, $1° \times 2°$)
FGOALS-g2	*Li et al.* [2013]	($2.8° \times 2.8°$, $1° \times 1°$)
FGOALS-s2	*Bao et al.* [2013]	($1.65° \times 2.8°$, $1° \times 1°$)
GISS-E2-R	*Schmidt et al.* [2014]	($2° \times 2.5°$, $1° \times 1°$)
MIROC-ESM	*Watanabe et al.* [2011]	($2.8° \times 2.8°$, $1° \times 1.4°$)
MRI-CGCM3	*Yukimoto et al.* [2012]	($1.1° \times 1.1°$, $1° \times 0.5°$)

3 Mid-Holocene climate

3.1 Experimental design

In the following we describe the experimental setup of our simulations. A summary of the experiment characteristics is also provided in Table 1.

For each model configuration we have two timeslice experiments, a pre-industrial control experiment and a mid-Holocene one. Integrations of ECHAM6-FESOM are initialized by the mean climatology from an Atmospheric Model Intercomparison Project (AMIP) and the data from the World Ocean Atlas (WOA). The boundary conditions, orbital parameters and Greenhouse gases (GHGs) are prescribed according to the Paleoclimate Modeling Intercomparison Project (PMIP) [*Crucifix et al.*, 2005]. ECHAM6-FESOM experiments are integrated for 460 years in T63 resolution ($1.9° \times 1.9°$) for the atmosphere component and varying resolution as shown in Fig. 2.1 for the ice-ocean component. The model has run into quasi-equilibrium with trends in sea surface temperature that do not exceed 0.05°C/century for the model years 300-460. Therefore, the average of the last 160 model years is considered to represent the climatology in both simulations. For comparison with the result of ECHAM6-FESOM, we conduct another two experiment EM31-CTR (a pre-industrial control setup) and EM31-6k (a mid-Holocene setup) using the ECHAM6-MPIOM model with low-resolution grid (T31GR30). The simulations are integrated for 700 model years with final trends in sea surface temperature being less than 0.01°C/century. Furthermore, in order to highlight the importance of model resolution, we also analyze in detail the ECHAM6-MPIOM

Table 3.1: *List of experiments and boundary conditions*

Experiment	EF-CTR	EF-6k	EM31-CTR	EM31-6k	EM63-CTR	EM63-6k
Model	ECHAM6-FESOM	ECHAM6-FESOM	ECHAM6-MPIOM	ECHAM6-MPIOM	ECHAM6-MPIOM	ECHAM6-MPIOM
Resolution	T63-high	T63-high	T31GR30	T31GR30	T63GR15	T63GR15
CO2 (ppm)	280	280	280	280	280	280
CH4 (ppb)	760	650	760	650	760	650
N2O (ppb)	270	270	270	270	270	270
Eccentricity	0.016724	0.018682	0.016724	0.018682	0.016724	0.018682
Obliquity	23.446	24.105	23.446	24.105	23.446	24.105
Precession	282.04	180.87	282.04	180.87	282.04	180.87
Time (a)	460(160)	460(160)	700(100)	700(100)	3000(100)	3000(100)

output in T63GR15 grid from the Coupled Model Intercomparison Project Phase 5 (CMIP5) data set. More detailed information about the experimental configuration is presented in Table 3.1.

In this section, we concentrate on the behavior of the high-resolution model ECHAM6-FESOM (experiments EF-CTR and EF-6k). For comparison, we also show results of ECHAM6-MPIOM in low-resolution grid T31GR30 (experiments EM31-CTR and EM31-6k) as well as ECHAM6-MPIOM with T63GR15, which is referred to as EM63-CTR for pre-industrial and EM63-6k for mid-Holocene (part of CMIP5). Moreover, the results of other CMIP5 models are shown in Section 3.5.

The seasonsal and annual mean climatology is calculated by averaging the climate parameters over the integration periods given in Table 3.1.

3.2 Atlantic Meridional Overturning Circulation

In EF-CTR, the Atlantic meridional overturning circulation (AMOC) streamfunction, defined as the zonally integrated stream function over the Atlantic basin, has the maximum of 13.4 Sv (1 Sv = 10^6 m^3/s) at 1000 m depth of 35°N (Fig. 3.1a), consistent with the estimates of global circulation from the hydrographic data (15±3 Sv) [*Ganachaud and Wunsch*, 2000]. This value increases by 1-2 Sv in the EF-6k (Fig. 3.1b), and the position of the maximum AMOC shifts northward.

Regarding the behavior of ECHAM6-MPIOM, the maximum AMOC streamfunction

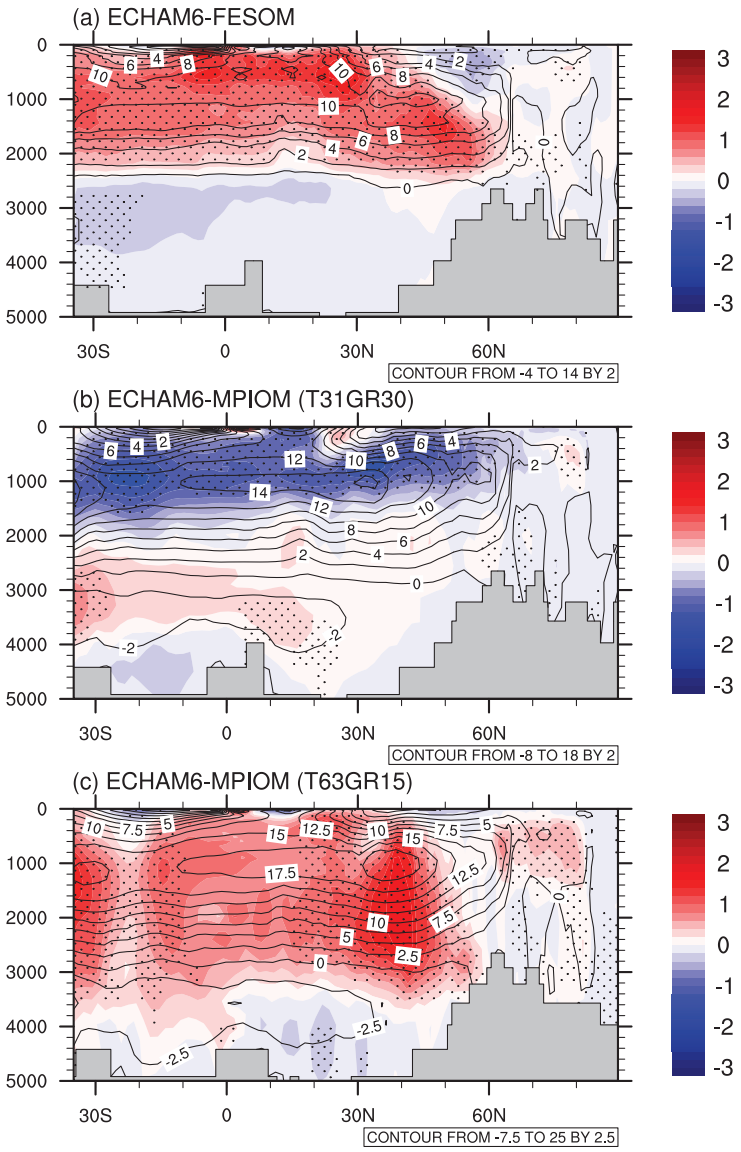

Fig. 3.1: *Simulated annual mean Atlantic meridional overturning circulation (contour lines) and its anomalies in mid-Holocene compared to pre-industrial (shading colors) based on (a) ECHAM6-FESOM, (b) ECHAM6-MPIOM with T31GR30 grid, and (c) ECHAM6-MPIOM with T63GR15 grid. Regions with >95% significance level (based on Student's T test) are hatched by black dots, auto-correlation has been taken into account. Units are Sv.*

happens at 1000 m depth between 30°N and 35°N, with the magnitude of 14 Sv and 20 Sv for coarse and higher resolution model, respectively. Different AMOC tendencies are observed as depicted in Fig. 3.1c,d: with coarse resolution (T31GR30), EM31-6k reproduces a decline in AMOC with a magnitude of about -2 Sv compared to EM31-CTR, similar to the T31GR30 setup by ECHAM5-MPIOM [*Fischer and Jungclaus*, 2010; *Wei and Lohmann*, 2012]. In contrast, the T63GR15 version of ECHAM6-MPIOM shows an increase in AMOC (2 Sv), which is similar to the result of ECHAM6-FESOM.

In summary, we detect big discrepancies of simulated AMOC anomalies between models with coarse (T31GR30) and higher (T63GR15) resolutions. Therefore, model resolution is an important factor which is explored in the following.

3.3 Properties of the North Atlantic Ocean

The North Atlantic Ocean is a critical region for the AMOC since its variability can change sea-water properties in particular the density in the sinking region of the North Atlantic deep-water formation sites and thus affects the strength of the AMOC.

The simulated North Atlantic temperature, salinity and density and their respective difference distributions in mid-Holocene compared to pre-industrial are given in Fig. 3.2. The distribution of sea surface temperature (SST) anomalies in ECHAM6-FESOM is characterized by a warming over the North Atlantic Ocean, Baffin Bay and Nordic Sea (Fig. 3.2a). It is attributed mainly to increased insolation in boreal summer, which is induced by a larger tilt of the orbital plane. The most intriguing change happens over the Gulf Stream, where the largest SST gradient occurs. The sea surface salinity (SSS) anomalies in ECHAM6-FESOM (Fig. 3.2d) presents a freshening Arctic Ocean (up to -0.5 psu), which is related to a smaller sea ice production. Compared to pre-industrial conditions, more saline sea water is simulated in the GIN (Greenland, Iceland, Norwegian) Sea, and the North Atlantic subpolar region (0.5 psu). More pronounced salinification is observed over the the Gulf Stream (more than 0.5 psu), which is connected to the strengthening of surface northward current. The corresponding density change in ECHAM6-FESOM resembles the SSS pattern, with negative anomalies over the Arctic Ocean and positive anomalies over the North Atlantic Ocean and Nordic Sea (Fig. 3.2g).

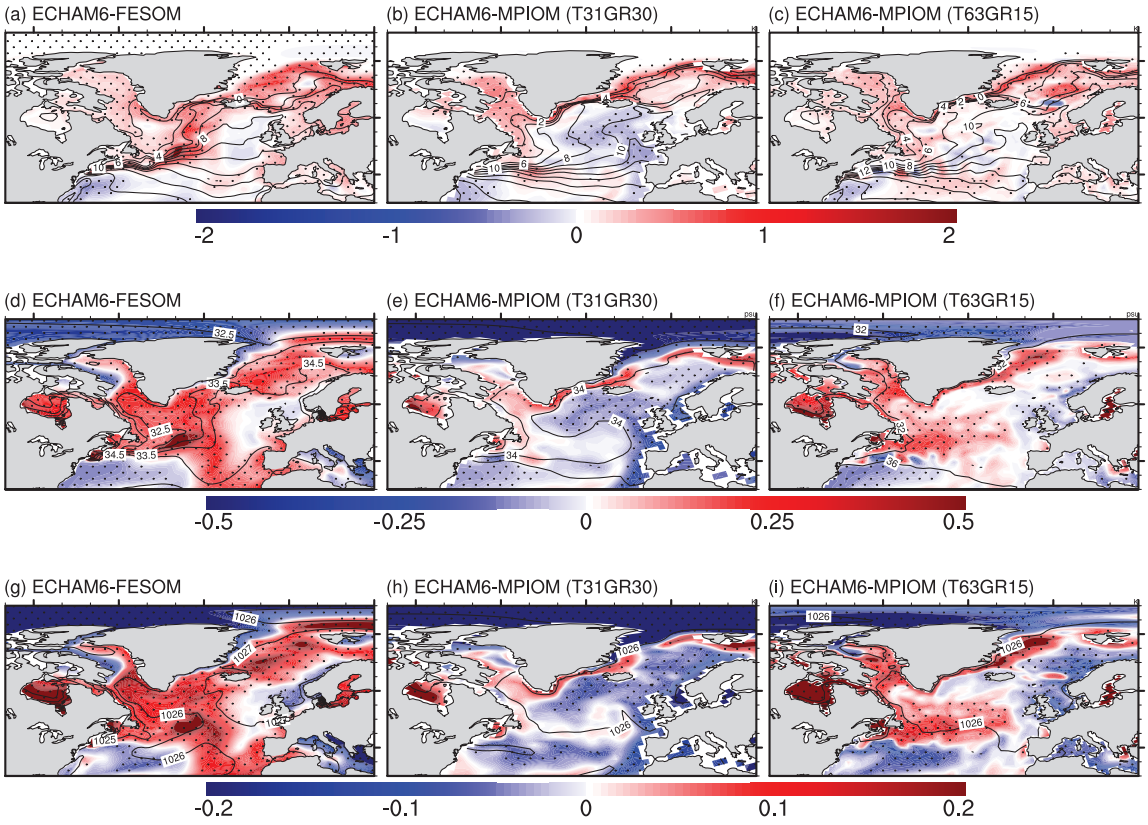

Fig. 3.2: *As in Fig. 3.1, but for (a-c) sea surface temperature, (d-f) sea surface salinity, and (g-i) sea surface salinity over the North Atlantic Ocean. Units are °C, psu and Kg/m^3, respectively.*

ECHAM6-MPIOM in both grids reveal a general warming in 6k over the Baffin Bay and Nordic Sea (Fig. 3.2b,c), compared to the pre-industrial conditions. A significant cooling is simulated by EM31-6k over the North Atlantic, particularly the northeastern part, while EM31-6k shows no obvious change over that region. A decrease in the Arctic SSS in 6k compared to pre-industrial (Fig. 3.2e,f) is revealed by both ECHAM6-MPIOM models with low and higher resolution. However, different SSS patterns are simulated over the North Atlantic Ocean. In EM31-6k, the surface sea water of North Atlantic and Nodic Sea is significantly freshened, whereas EM63-6k presents an increase of about 0.3 psu in the salinity of the Greenland Sea and North Atlantic subpolar gyre, which is consistent with the result of ECHAM6-FESOM, even though smaller in magnitude. The density anomalies, similar to the SSS patterns in both models, present a less dense North Atlantic in EM31-6k, and the opposite case for EM63-6k (Fig. 3.2h,i).

Deep convection in subpolar regions is the main driving mechanism for AMOC. As the deepest Northern Hemisphere mixed layer depth (MLD) happens in March, here we depict the distributions of March MLD in the three models (Fig. 3.3). Identified by deep MLD, three main deep water formation sites simulated by the three models are located at (1) the Labrador Sea (shown in the red box of Fig. 3.3), (2) the northeastern North Atlantic (blux box), and (3) the Nordic Sea (green box), in good agreement with observations and most climate models [*Danabasoglu et al.*, 2014]. Differences in the modeled MLD are also noticed. For example, ECHAM6-FESOM depicts extreme MLD in the eastern North Atlantic. Deep convection in the Labrador Sea is much less pronounced, owing to an excessive simulated sea ice cover extending into the northwestern North Atlantic Ocean. ECHAM6-MPIOM with T63GR15 grid show the deepest mixed layer at the Labrador Sea and Nordic Sea, while MLD of ECHAM6-MPIOM T31GR30 is deeper in the Nordic Sea than other regions. Besides, the deep water formation sites of the Labrador Sea and northeastern North Atlantic in ECHAM6-MPIOM T31GR30 are much smaller and shallower than in other two models.

To further demonstrate the relationship between the North Atlantic density and AMOC, we define in the model three regions as shown in boxes in Fig. 3.3, which cover the three deep water formation sites, respectively. We calculate the lag correlation coefficients between the AMOC indices and the averaged surface density over the respective deep MLD region as shown in Fig. 3.4. For the Labrador Sea, the correla-

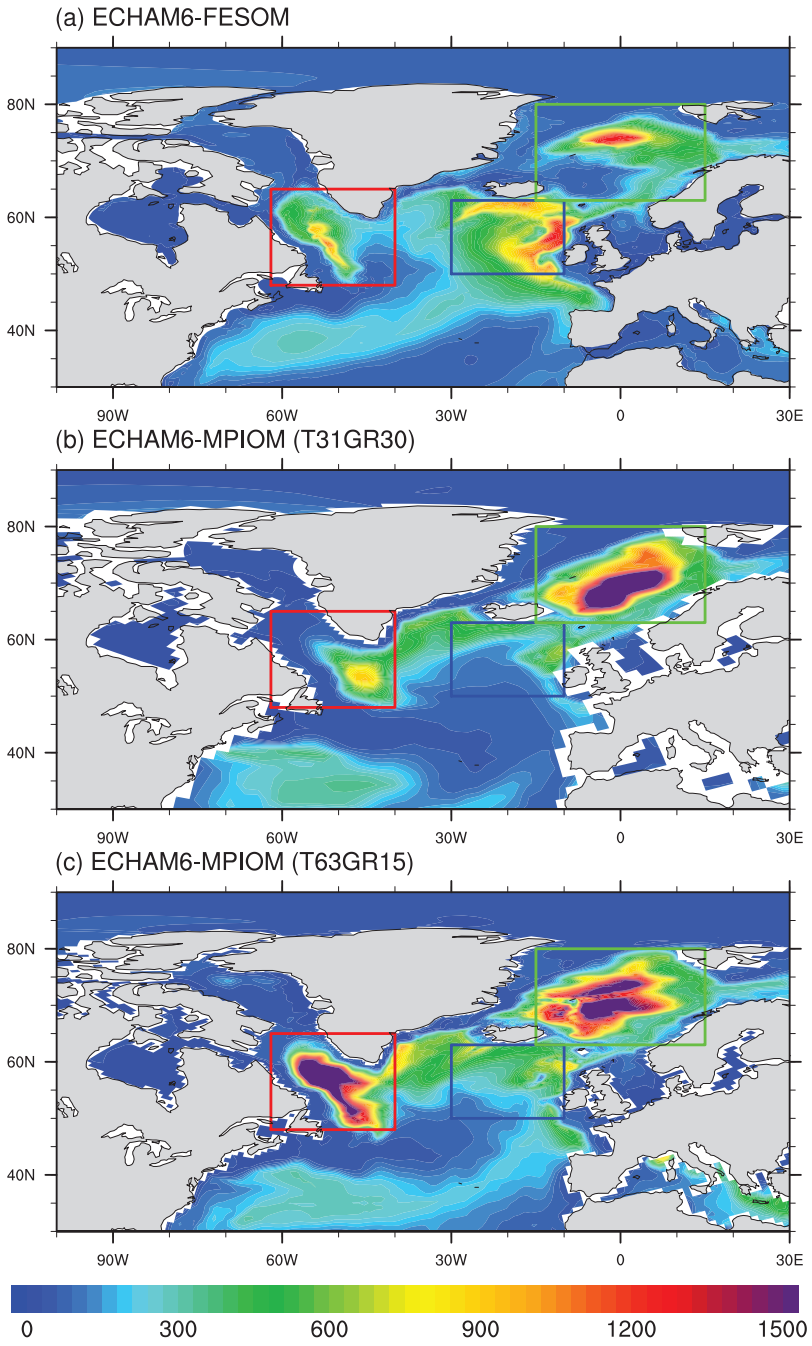

Fig. 3.3: *Mixed layer depth simulated by (a) ECHAM6-FESOM, (b) ECHAM6-MPIOM with T31GR30 grid, and (c) ECHAM6-MPIOM with T63GR15 grid. Units are m.*

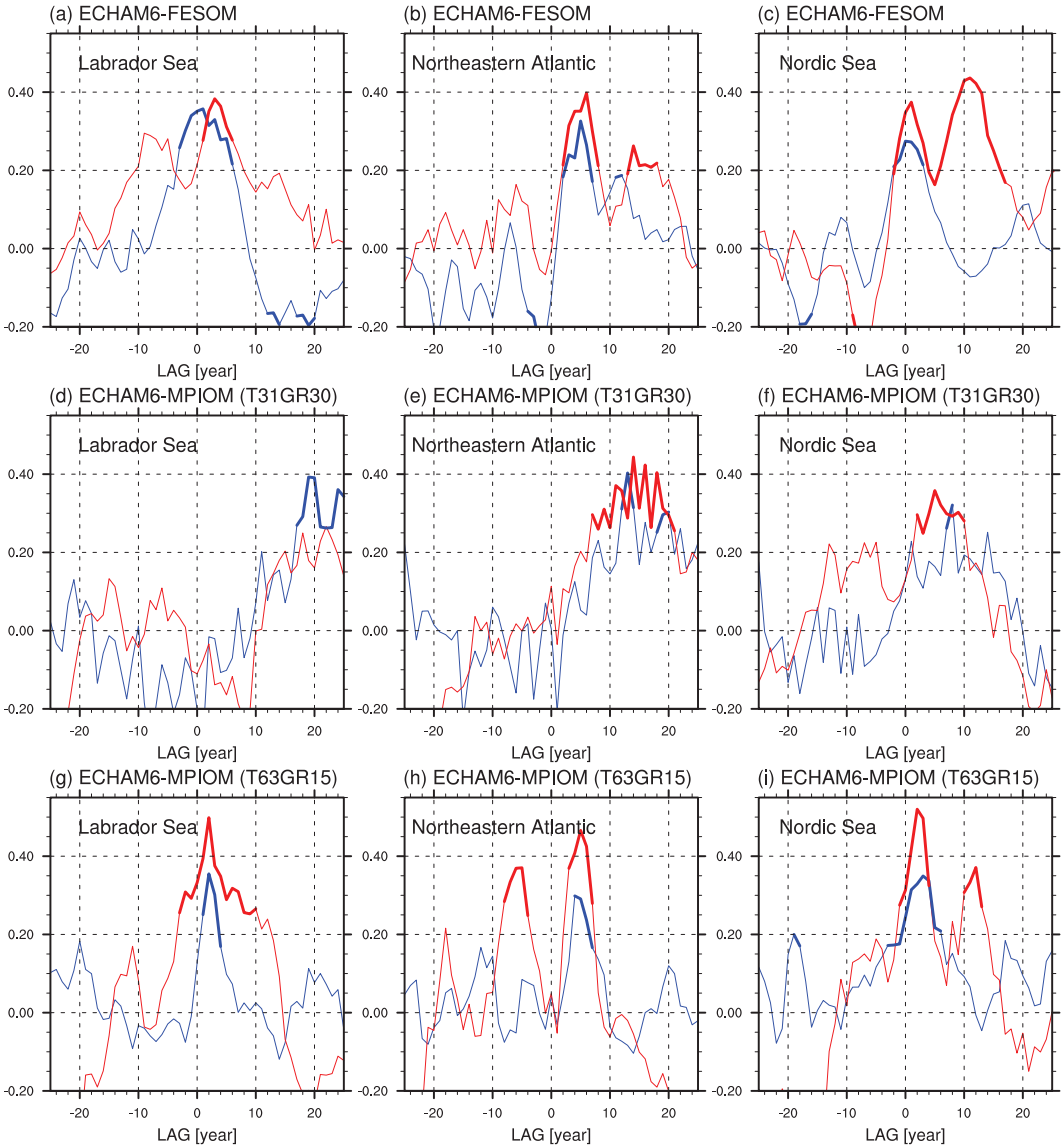

Fig. 3.4: *(a-c) Lag correlation coefficients between AMOC indices and averaged surface density over (a) Labrador Sea, (b) northeastern Atlantic, and (c) Nordic Sea in ECHAM6-FESOM. (d-f) As in (a-c), but for ECHAM6-MPIOM (T31GR30). (g-i) As in (a-c), but for ECHAM6-MPIOM (T63GR15). Blue lines are for pre-industrial, and red lines for mid-Holocene. The AMOC indices are derived from the maximum meridional streamfunction at 500-2000 m depth and 30-50°N in the Atlantic Ocean. Taking into account the auto-correlation, thick segments indicate > 97.5% significance level based on Pearson's R test given N degrees of freedom, where N equals to the number of data points divided by two times e-folding time of auto-correlation. Positive lags (yr) indicate that the density leads the AMOC and vice versa.*

tion coefficients reach the maximum with significant values when the density leads the AMOC by 1 and 3 years in EF-CTR and EF-6k, respectively. Coarse-resolution model ECHAM6-MPIOM show no obvious relationship between the Labrador density and the overturning circulation, even though a small coefficient value (< 0.3) is found when density lagging the AMOC 18 years. This is might due to the relatively narrow and shallow MLD in EM31-CTR and EM31-6k. ECHAM6-MPIOM in T63GR15 shows the maximum correlation coefficients when the Labrador density leads the AMOC 2 years.

The density over the northeastern North Atlantic has a peak correlation with AMOC when lagging about 6, 15 and 5 years in ECHAM6-FESOM, ECHAM6-MPIOM (T31GR30) and ECHAM6-MPIOM (T63GR15), respectively. Besides, another peak is as well detected by EM63-6k when the AMOC leads the density 5 years. This is reasonable, as a stronger AMOC brings more saline and dense sea water from the mid-latitudes to the north, and causes a heat loss which provides for a Labrador Sea cooling.

Two peak correlation coefficients are noticed in EF-6k, when the density over Nordic leads the AMOC indices 2 and 12 years. For EF-CTR, only one maximum value is found, with a lag of 1 year. In terms of ECHAM6-MPIOM, the coarse-resolution version shows the most maximum correlation value when the Nordic Sea density leads the AMOC 5-8 years, and the T63GR15 version indicates a lag of 2-4 years when the correlation coefficients reach the maximum. However, the correlation magnitude is very small for EM63-CTR (< 0.2), even though it slightly exceeds the 97.5% significance level.

Lag correlation coefficients between AMOC indices and averaged SSS over the deep MLD sites are similar to Fig. 3.4 (not shown), as salinity is the most important contributor to sea water density. In summary, all experiments show a clear response of the simulated AMOC to the averaged density/salinity over the main deep water formation sites, with a lag of varying years.

3.4 Atmospheric processes related to AMOC

a. North Atlantic Oscillation (NAO)

There are a broad range of evidences, including observations and model simulations, suggest that the changes in the AMOC are likely to be the result of natural multi-decadal climate variability and are driven by low-frequency variations of the North Atlantic Oscillation (NAO) — a leading mode of natural atmospheric variability [*Hurrell*, 1995] — through changes in the deep convection of Labrador Sea [e.g., *Houghton*, 1996; *Dickson*, 1997; *Curry et al.*, 1998; *Eden and Willebrand*, 2001; *Latif et al.*, 2006; *Latif and Keenlyside*, 2011; *Scholz et al.*, 2014]. In this section we focus on the hydrological budget and convection state in the deep water formation sites, which is linked to the atmospheric NAO variability.

There is generally a consistent distribution in the December-to-February (DJF) anomalies in 6k mean sea level pressure (SLP) compared to pre-industrial (Fig. 4.10). Common features in the three models include a anomalous higher SLP north of 50°N certering at Iceland, a lower SLP south of 50°N, and a tendency toward an increased latitudinal gradient in mean SLP, forming a positive NAO-like mode.

b. Net precipitation

As depicted in Fig. 4.6, the distribution of Precipitation minus Evaporation (P-E) anomalies is characterized by: (1) drier conditions over Baffin Bay, Nordic Sea, and western North Atlantic including the Labrador Sea; (2) wetter conditions over north-eastern North Atlantic and the coastal region of America. One exception is that a local increased P-E is simulated by EM31-6k over a small part of the Labrador Sea, even though not significant.

The differences of P-E as illustrated in Fig. 4.6 contribute to the SSS and density anomalies as in Fig. 3.2d-i. In detail, the saltier and denser Labrador Sea, North Atlantic subpolar gyre and Nordic Sea in EF-6k is partly owing to the reduced P-E over those regions. Similarly, EM63-6k produces a more dense sea water over Labrador Sea, North Atlantic subpolar gyre and Greenland Sea, which can be induced by the corresponding P-E anomalies distributions. In contrast, the wetter conditions over

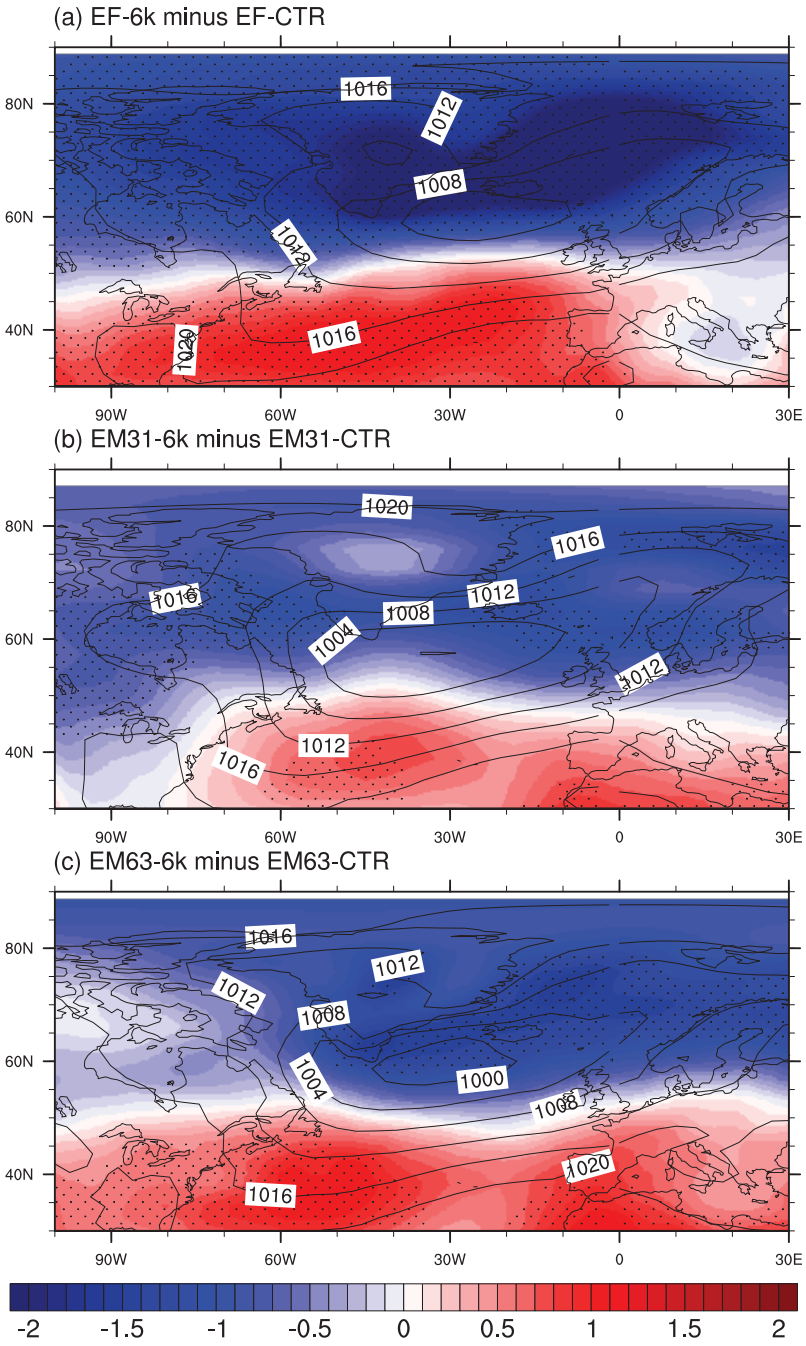

Fig. 3.5: *As in Fig. 3.1, but for DJF sea level pressure. Units are hPa.*

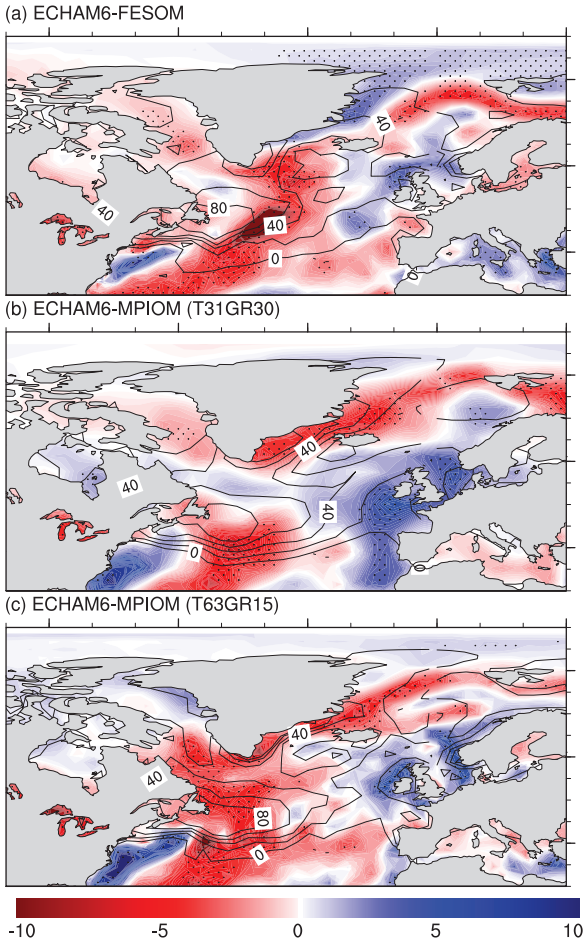

Fig. 3.6: *As in Fig. 3.1, but for annual mean precipitation minus evaporation (P-E). Units are mm/month.*

Labrador Sea and northeastern North Atlantic in EM31-6k contribute to a decreased salinity and density over the respective region.

The behaviors of the three models in terms of their P-E anomalies distributions in the Labrador Sea are associated with a response to the NAO Index variability (NAOI, not shown). In summary, the main difference in model behavior regarding the P-E anomalies (6k minus 0k) happens mainly over the Labrador Sea, which lies on the different P-E responses to NAO variability between low and higher resolution models. The composite maps of P-E in respect to high NAOI are shown in Fig. 3.7. In good agreement with previous studies [e.g., *Hurrell*, 1995; *Hurrell et al.*, 2003] for present climate, evaporation exceeds precipitation over much of Baffin Bay and Labrador Sea during high NAOI years, one clear exception is in EM31-CTR, where net precipitation occurs in part of the Labrador Sea during high NAOI years, similar to the P-E anomalies pattern. Moreover, the responses of 6k P-E to the NAO indices show similar patterns (not shown here).

c. Surface heat fluxes

Fig. 3.8 presents the surface heat flux changes between 6k and pre-industrial runs. There is no obvious difference in conductive heat flux (CHF, positive downward) over the central Arctic Ocean (Fig. 3.8a-c), indicating no significant influence of sea ice change on CHF. Enhanced loss of conductive heat happens over Greenland and Barents Seas, which dominates the patterns of net surface heat flux (Fig. 3.8g-i). There is a general increase in net surface radiative flux (SRF, positive downward) for the whole Arctic region and Northern Hemisphere continents (Fig. 3.8d-f), dominating the enhanced total heat flux in the Arctic Ocean (Fig. 3.8g-i). Such SRF anomaly is mainly owing to the re-distributed solar insolation in boreal summer, and to the reduction of the Arctic sea ice (i.e., ice-albedo feedback). The warming of Arctic SAT in 6k compared to pre-industrial in ECHAM6-FESOM (not shown here) is mainly a result of enhanced net surface heat flux. A more pronounced feature of CHF and total heat flux in EF-CTR and EM63-CTR is the negative and positive anomalies over Northwestern Atlantic and Northeastern Atlantic, respectively, which is similar to the NAO-related heat flux distribution (ig. 3.92a,c). However, a reversed pattern is found for EM31-CTR (ig. 3.92b), which leads to an increased CHF and total heat flux over the Labrador Sea.

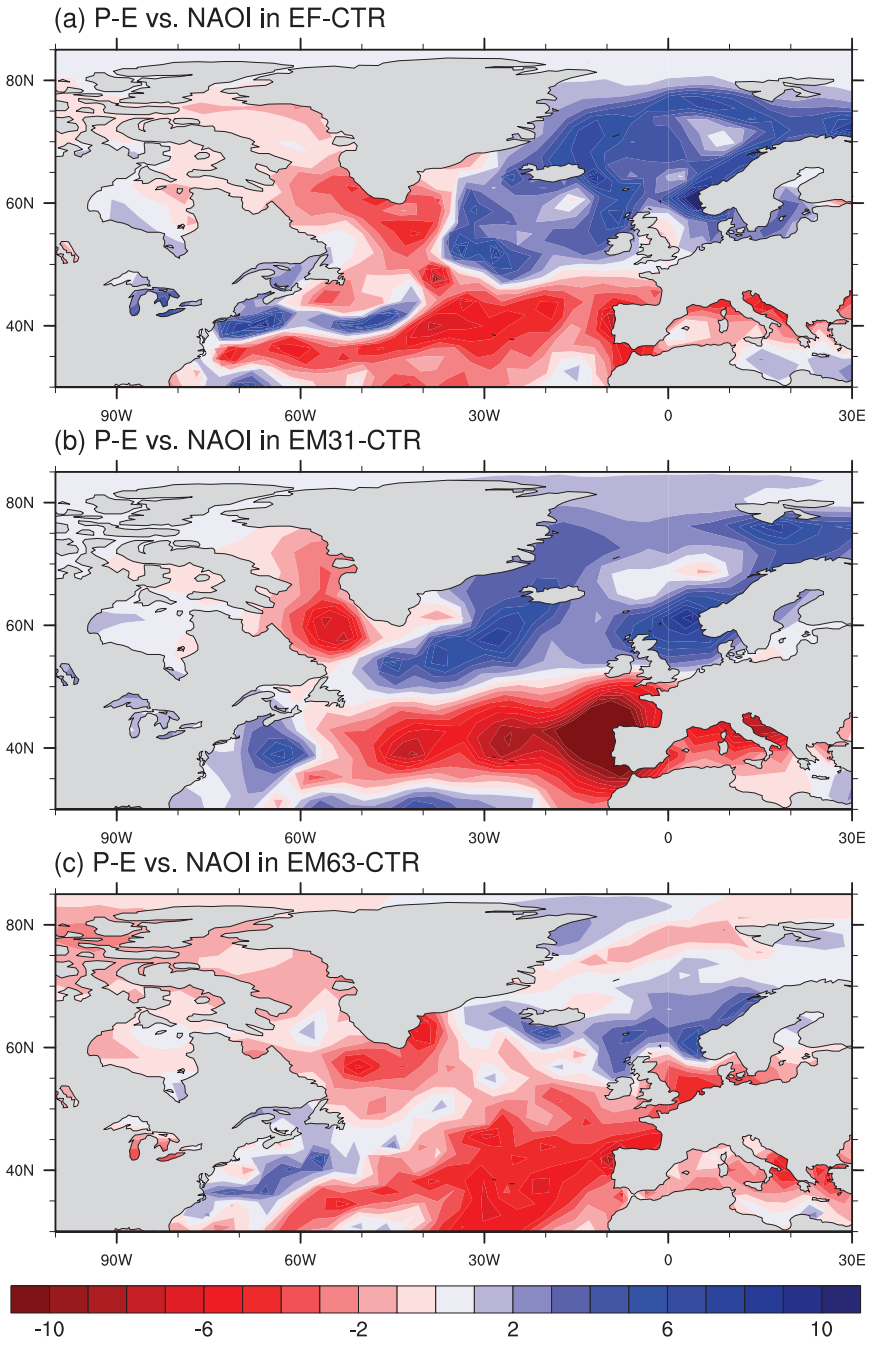

Fig. 3.7: *Averaged P-E anomalies (depature from the annual mean state) during years when the NAOI exceeds one standard deviation, for the three pre-industrial experiments. Units are mm/month.*

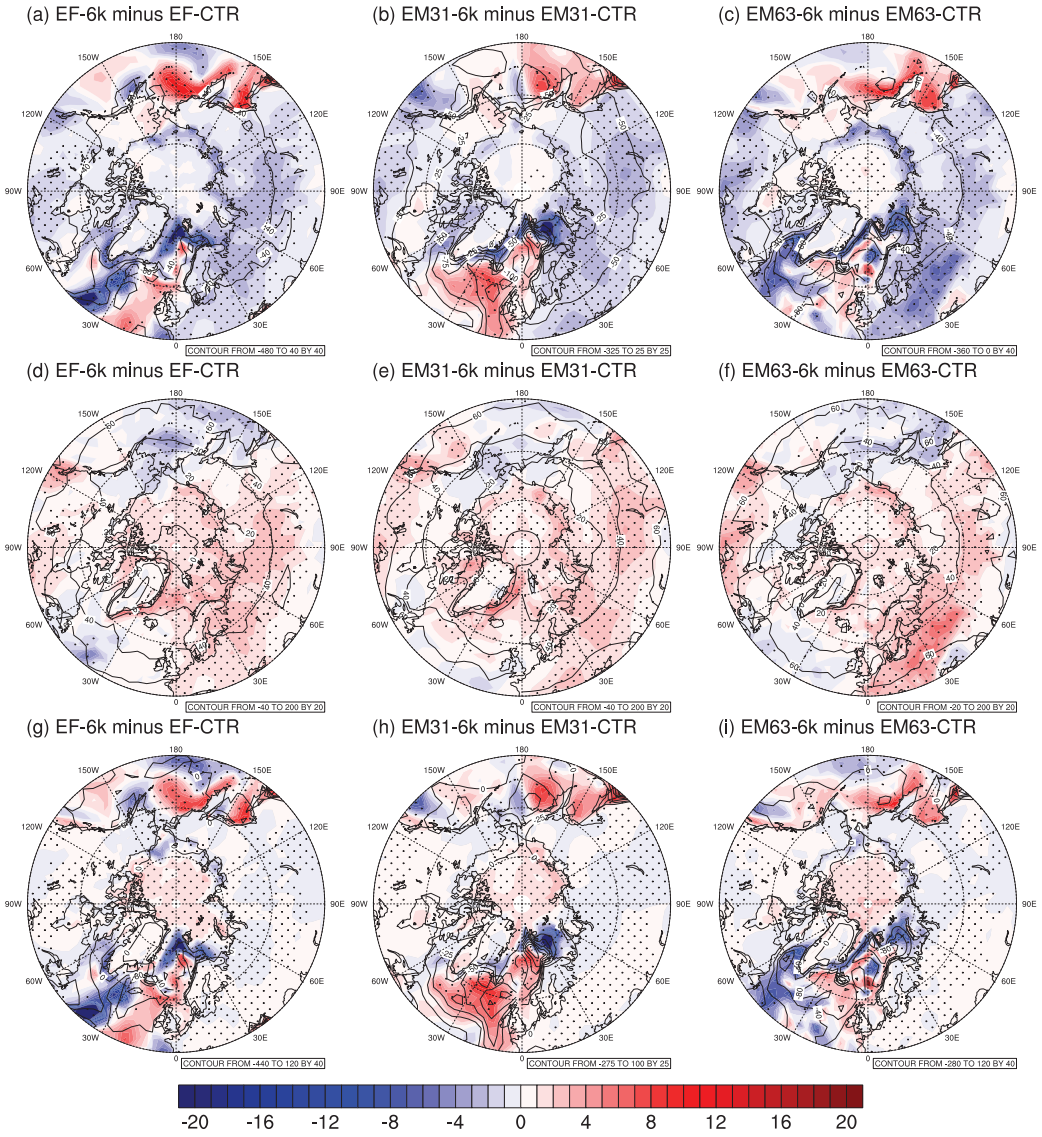

Fig. 3.8: *As in Fig. 3.1, but for (a-c) surface conductive heat flux, i.e., the sum of surface latent and sensible heat fluxes, (d-f) net surface radiative flux, i.e., the sum of net surface longwave and shortwave fluxes, and (g-i) net surface heat flux, i.e., the sum of surface conductive heat flux and net surface radiative flux. Blue means net heat loss, and red represents net heat gain. Units are* W/m^2.

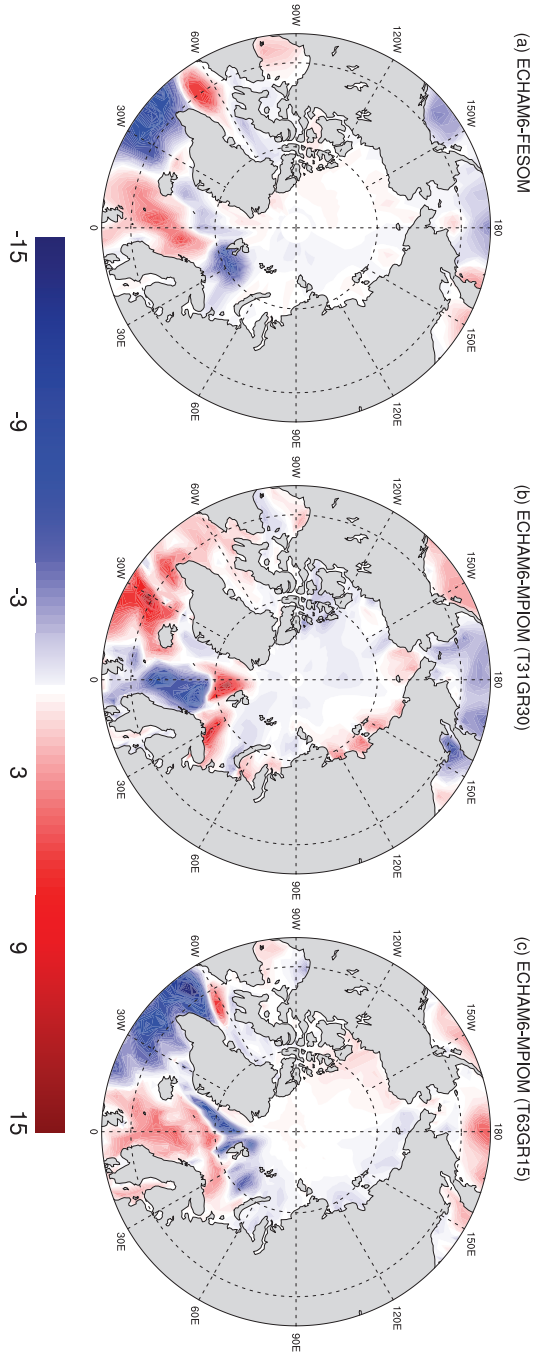

Fig. 3.9: *Averaged surface heat flux anomalies (depature from the annual mean state) during years when the NAOI exceeds one standard deviation, for the three pre-industrial experiments. Units are* W/m^2.

Ocean model simulations reveal that NAO-related net loss of surface heat flux over the Labrador Sea can induce a fast response (lag 2-3 years) of the AMOC [*Häkkinen*, 1999; *Eden and Willebrand*, 2001], through boundary wave processes which rapidly formed between subpolar and tropical latitudes[*Getzlaff et al.*, 2005]. Such mechanism is also detected on longer time scales [*Visbeck et al.*, 1998; *Latif et al.*, 2004]. Thus we conclude that the simulated discrepancy in 6k AMOC in coarse and higher resolution models is likely owing to the different response of the Labrador Sea surface heat flux to NAO variations.

3.5 Oceanic processes related to AMOC

a. Growth/melt of sea ice

Fig. 3.10a depicts the change of annual mean sea ice thickness in the Arctic. Compared to EF-CTR, a notable feature in EF-6k is a significant decrease in sea ice thickness, coinciding with the increased boreal summer insolation. The maximum change is about -1 m on an annual average, occurring over the north of Greenland, this is simply a reflection of the increased advection of sea-ice volume from the central Arctic by the Beaufort Gyre. Similarly, ECHAM6-MPIOM in both resolutions indicates a pronounced decrease in Arctic sea ice (Fig. 3.10b,c), while the response is more pronounced in the coarse-resolution model.

The freshened Arctic Ocean is led by the smaller net sea ice formation during mid-Holocene compared to present. Moreover, the coastal region of Greenland is found to be less dense in 6k, which is also a result of the reduced sea ice volume over there.

b. Transport of sea ice

In this section, we focus on the link of sea ice dynamics with density over the region of deep water formation. Multiyear sea ice originating in the Arctic Ocean is being exported through the Fram Strait into the Greenland Sea and represents a large amount of drain in the freshwater balance of the Arctic Ocean. As shown in Fig. 3.10, less sea ice, associated with an increase in summer solar insolation, is simulated in our mid-Holocene experiments. Relating to the loss of sea ice in the Central Arctic Ocean, there

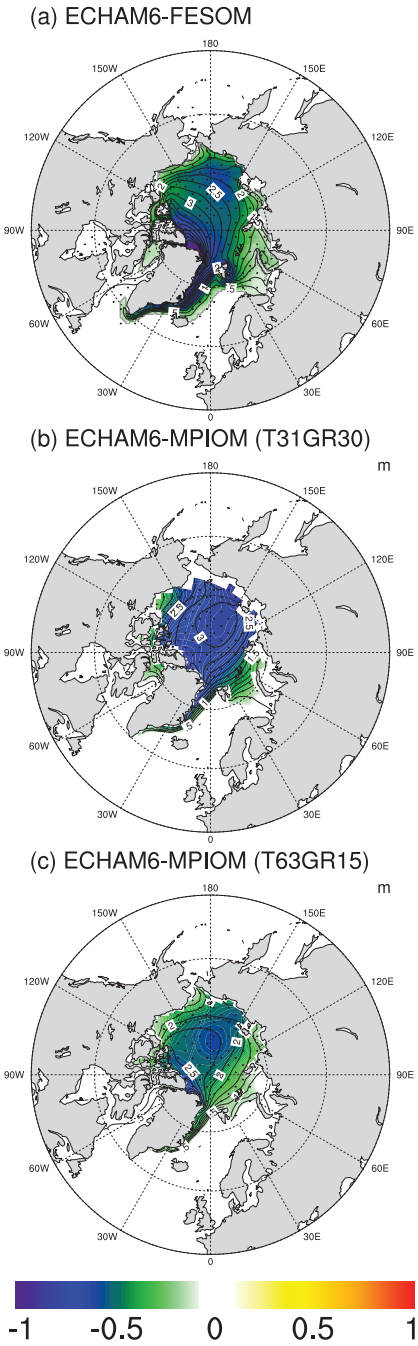

Fig. 3.10: *As in Fig. 3.1, but for the Arctic mean sea ice thickness. Units are m.*

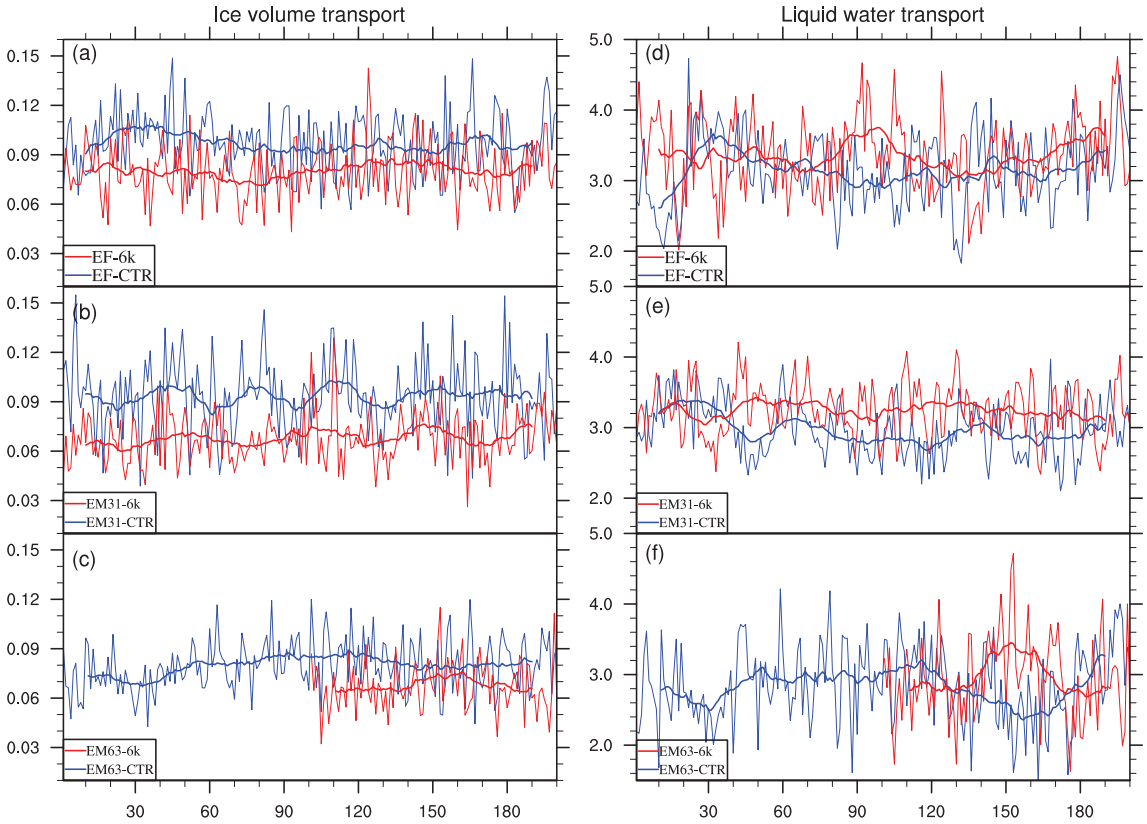

Fig. 3.11: *(a-c) Time series of sea ice volume transport through Fram Strait in (a) ECHAM6-FESOM, (b) ECHAM6-MPIOM in T31GR30 grid and (c) ECHAM6-MPIOM in T63GR15 grid. For the thick lines, a 21 years filter is applied. Units are Sv. (d-f) As in (a-c), but for sea water volume transport through the Fram Strait. Units are Sv.*

is a reduction of sea ice volume import through Fram Strait (ICEFS) (Fig. 3.11a-c), with the annual mean anomaly being -0.016 Sv, -0.026 Sv and -0.012 Sv for EF-6k, EM31-6k and EM63-6k, respectivly, which is significant on 99% level. Such change results in a pronounced decrease of salinity over the associated subpolar regions (Fig. 3.2d-i).

To further investigate the influence of the Fram Strait sea ice import on deep water formation, composite analyses are calculated as depicted in Fig. 3.12, by averaging the density anomalies fields that have less than one standard deviation with respect to indices of ICEFS. It is noteworthy that such composite maps of density during low phase of ICEFS (Fig. 3.12) are very similar to the distributions of density anomalies as shown in Fig. 3.2g-i. When small ICEFS occurs in EF-CTR, there is a pronounced increase in the density over subpolar North Atlantic Ocean and Greenland Sea with a delay of 2 years. Similar pattern is revealed by EM63-CTR except three specific features: 1) the values are of smaller magnitude, 2) the most pronounced response happens over 40°N-50°N, resembling the density anomalies (Fig. 3.2i), and 3) heavier sea water occurs over the northeastern North Atlantic. Considering the regions of deep water formations (Fig. 3.3) and the AMOC resonse to sea water density (Fig. 3.4), we see that the reduction in Fram Strait sea ice import to lower latitudes in mid-Holocene causes an increase in density over deep water formations sites, further leading to a stronger deep water formation and hence a strengthening in AMOC.

In contrast, EM31-CTR indicates increased density over the Labrador Sea and coast of Greenland when led 1 year by low ICEFS, while other regions (e.g., northeastern North Atlantic) experience a general decrease in sea water density (Fig. 3.12). However, the sea water over south of Greenland is freshened by increased P-E, which compensates the influence of reduced sea ice trasnport. Therefore, the combined effect of these two processes leads to the density anomalies as in Fig. 3.2h. The weakened AMOC in EM31-6k is a consequence of the dilutive Nordic Sea and northeastern North Atlantic (Fig. 3.2h).

The composite maps between density anomalies and low ICEFS in the mid-Holocene experiments are similar to Fig. 3.12, therefore is not shown here.

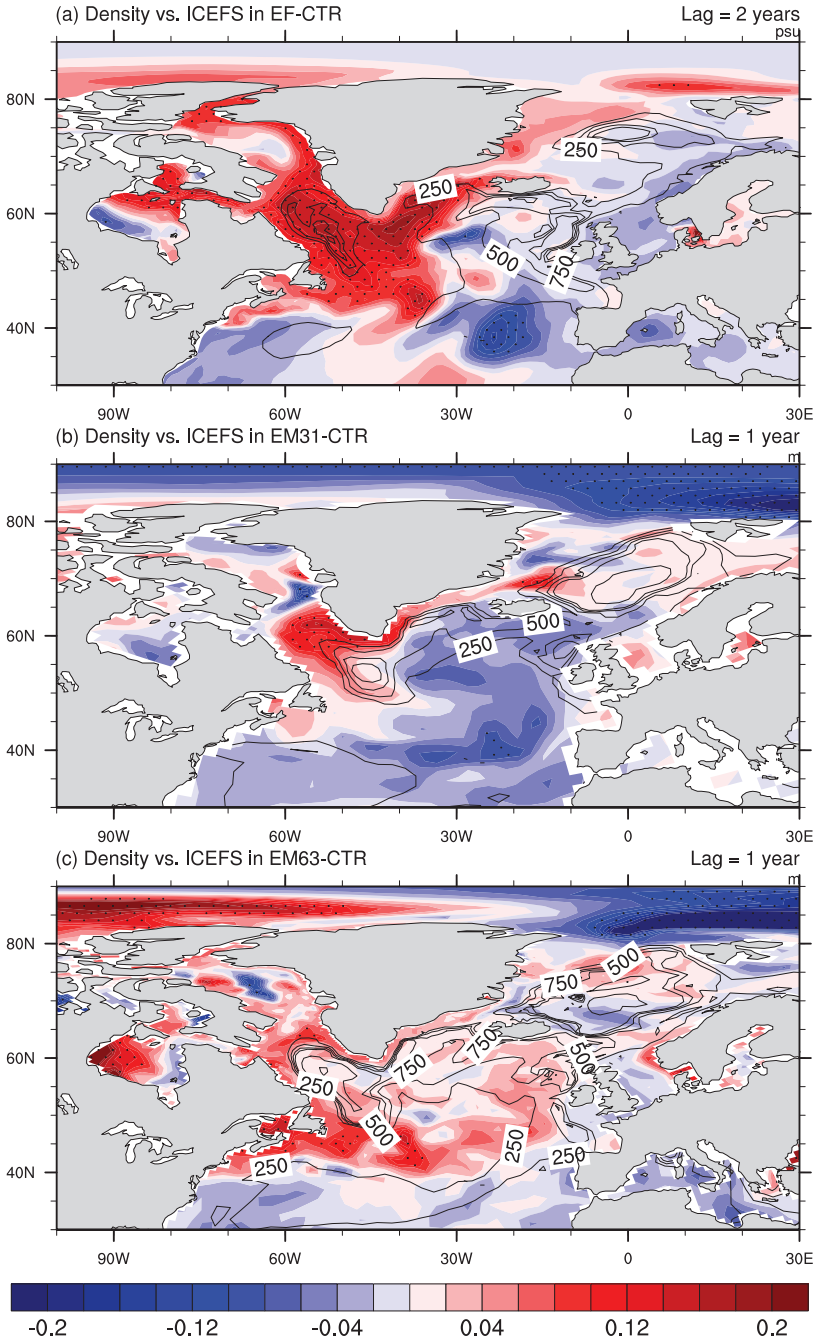

Fig. 3.12: *Averaged sea surface density anomalies (depature from the annual mean state) during years when ICEFS is below one standard deviation, with a lag of 1-2 years (ICEFS leads), based on the three pre-industrial experiments. Units are kg/m^3. Contour lines present the pre-industrial mixed layer depth in March.*

c. Transport of sea water

Ocean current is one of the main causes for density advection. From the north, the North Atlantic exchanges sea water with the Arctic Ocean through the Canadian Archipelago, Fram Strait and Barents Opening. From the south, the warmer and saltier water mass flows into the North Atlantic Ocean, which forms the upper branch of meridional overturning circulation.

Here we focus on the liquid water volume import through Fram Strait (LWFS) in the three models, as no significant differences are found for the transport of Arctic sea water through Canadian Archipelago and Barents Opening. Fig. 3.11d-f illustrate the time series of annual mean LWFS, it can be seen that all mid-Holocene experiments tend to simulate larger amount of LWFS than their pre-industrial counterparts, with the averaged difference being 0.24 Sv (significance level $> 99\%$), 0.27 Sv ($> 99\%$), and 0.1 Sv (90%) in ECHAM6-FESOM, ECHAM6-MPIOM (T31GR30) and ECHAM6-MPIOM (T63GR15), respectively. The negative anomalies in LWFS contribute to a freshening Greenland Sea and Labrador Sea (Fig. 3.13). For EM31-CTR, such freshening mainly occurs at the northeastern Atlantic Ocean (Fig. 3.13b).

With enhanced AMOC, the relatively warmer and saltier sea water which orgins from lower latitudes advects to the North Atlantic Ocean. The AMOC response in turn generates positive salinity (and density) anomalies. This well-known salinity-advection mechanism is a positive feedback on the thermohaline circulation response [*Stommel*, 1961]. Therefore, the positive/negative salinity anomalies in the North Atlantic simulated in different models is partly a consequence of the change in AMOC strength.

3.6 Results of other coupled climate models

The simulated AMOC may differ from model to model, here we have a supplementary analysis of the climatology data of different models from CMIP5 [*Taylor et al.*, 2012] (Table 2) to have a further view of the AMOC change.

Fig. 3.14 depicts the annual mean sea ice thickness anomalies in different models (c.f., Fig. 3.10). Most of the models represent an obvious decrease in the sea ice thickness. FGOALS-g2 show a general decrease in sea ice but in some parts of the Arctic, for example, regions to the north and west of Greenland, and in the western Barents Sea,

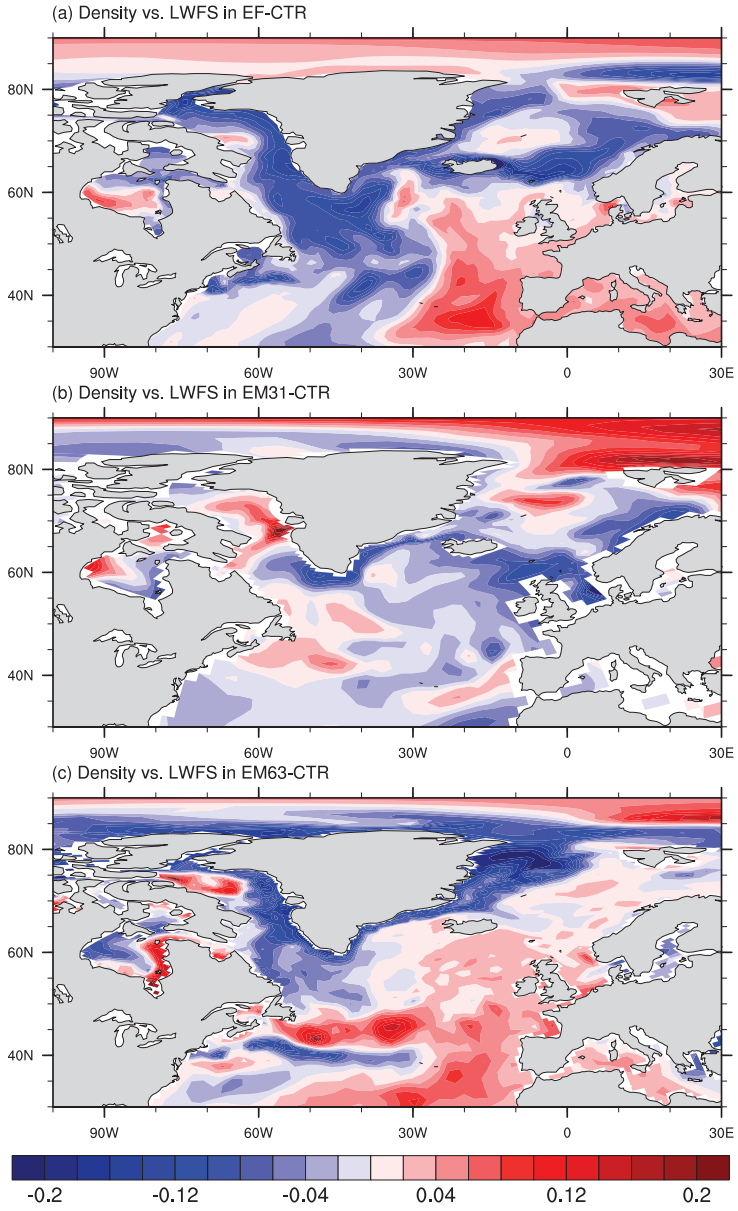

Fig. 3.13: *As in Fig. 3.12, but for sea surface density anomalies during high LWFS years. Units are* kg/m^3.

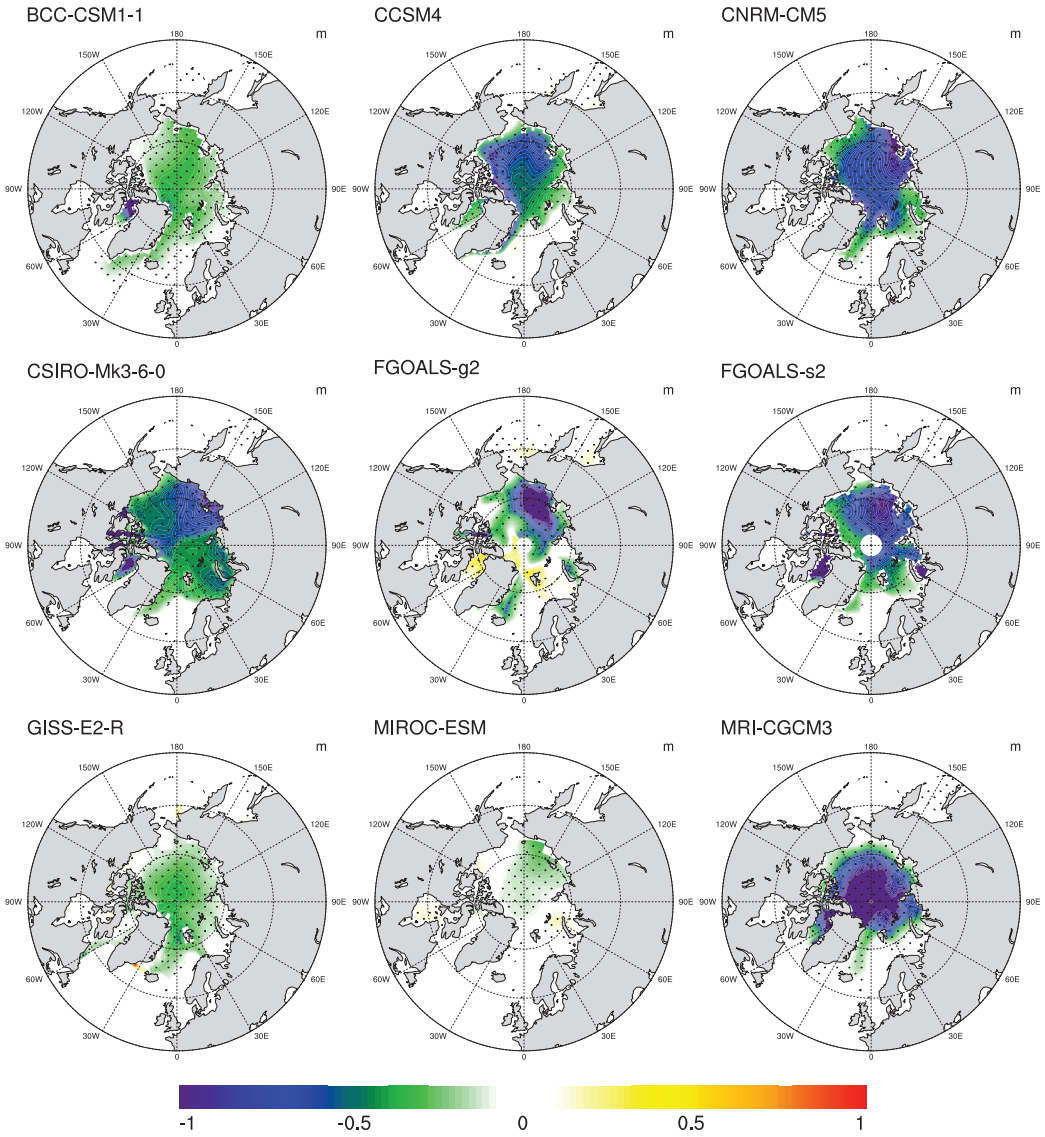

Fig. 3.14: *Simulated annual mean ice thickness anomalies in different models. Units are m.*

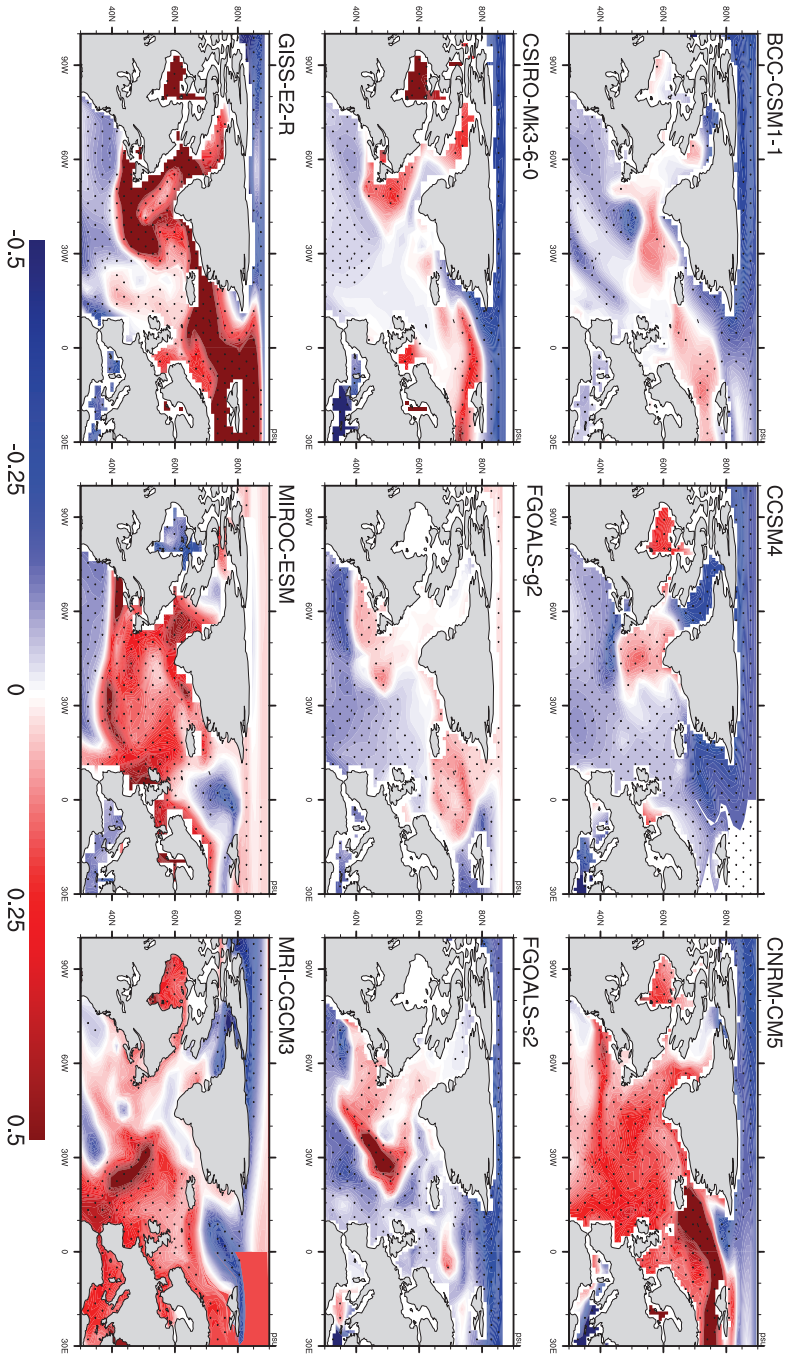

Fig. 3.15: *Simulated annual mean sea surface salinity anomalies in different models. Units are psu.*

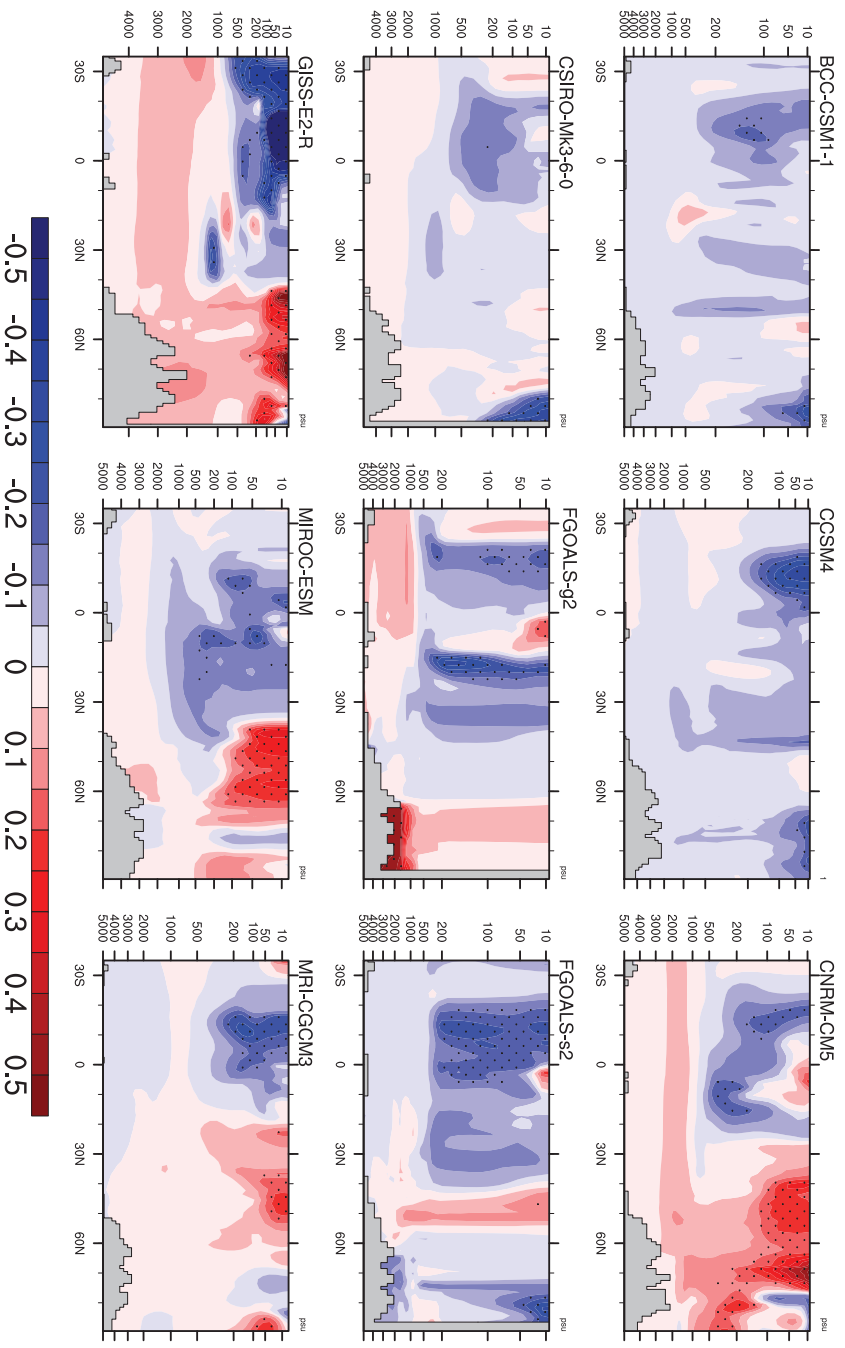

Fig. 3.16: *Simulated annual mean ocean salinity anomalies for the Atlantic region in different models. Units are psu.*

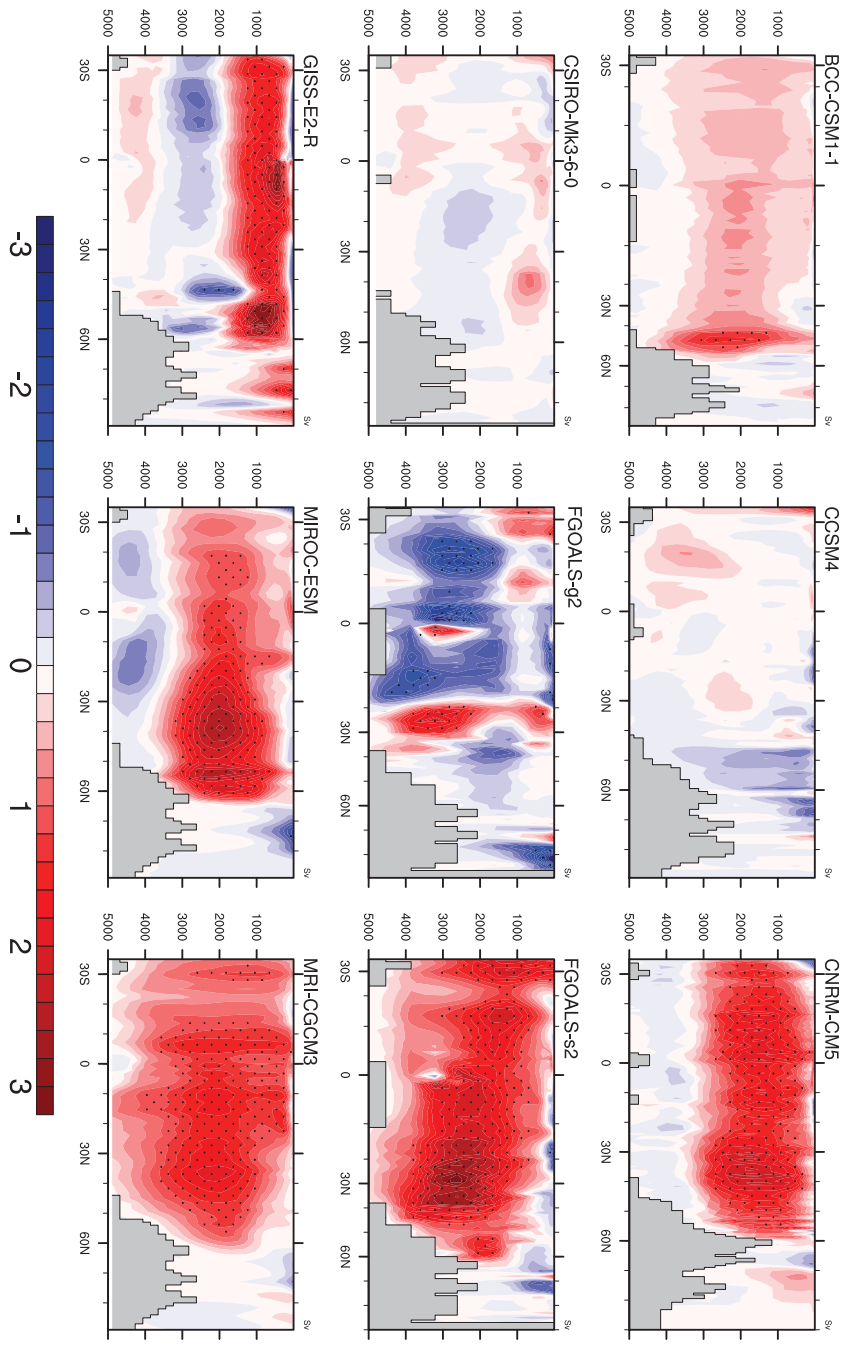

Fig. 3.17: *Simulated AMOC anomalies in different models. Units are Sv.*

thicker sea ice is found. MIROC-ESM also simulates increased ice in some regions, but at a smaller magnitude.

The SSS anomalies in different CMIP5 models, as well as the main three models used in this study, are depicted in Fig. 3.15 (c.f., Fig. 3.2d-f). BCC-CSM1-1, CCSM4, CSIRO-Mk3-6-0 and FGOALS-s2 simulate fresher sea water in the whole Arctic. FGOALS-g2 shows no obvious change in SSS over mid and high latitudes. MIROC-ESM presents a maximum change of about 0.5 psu in the Northern Atlantic Ocean, but no significant change in the Central Arctic. There are 3 models (i.e., CNRM-CM5, GISS-E2-R and MRI-CGCM3) show decreased salinity in the Central Arctic and increased SSS over the GIN Sea and North Atlantic subpolar region.

The zonal profiles of ocean salinity in CNRM-CM5, GISS-E2-R, MIROC-ESM and MRI-CGCM3 are similar to ECHAM6-FESOM and ECHAM6-MPIOM (T63GR15) (Fig. 3.16, c.f., Fig. 3.18), with denser and fresher sea water over the northern and southern Atlantic, respectively. ECHAM6-MPIOM (T31GR30) indicates the opposite pattern. Besides, BCC-CSM1-1, CCSM4, CSIRO-Mk3-6-0, FGOALS-s2 and FGOALS-g2 show a general decrease in ocean salinity.

Owing to the salinity anomalies of sea water in CNRM-CM5, GISS-E2-R, MRI-CGCM3 and MIROC-ESM, the associated AMOC is enhanced in these models (Fig. 3.17, c.f., Fig. 3.1). FGOALS illustrates different results in its two versions, as weakened AMOC is presented in FGOALS-g2 and stronger AMOC in FGOALS-s2, which is in agreement with *Zheng and Yu* [2013]. There is only a slight change of AMOC in BCC-CSM-1, CCSM4 and CSIRO-Mk3-6-0.

3.7 Discussion

The ice-ocean component in FESOM has the advantage in the ability to provide a regional focus in an otherwise global setup [*Sidorenko et al.*, 2011]. In our paper, FESOM applies even higher resolution in the high latitudes, is therefore suitable for investigating polar properties particularly sea ice characteristics.

Simulations by ECHAM6-FESOM show an increase of 1-2 Sv in mid-Holocene AMOC compared to the pre-industrial state, and the position of the maximum AMOC shifts northward. Such northward displacement is likely linked to the crossover between the

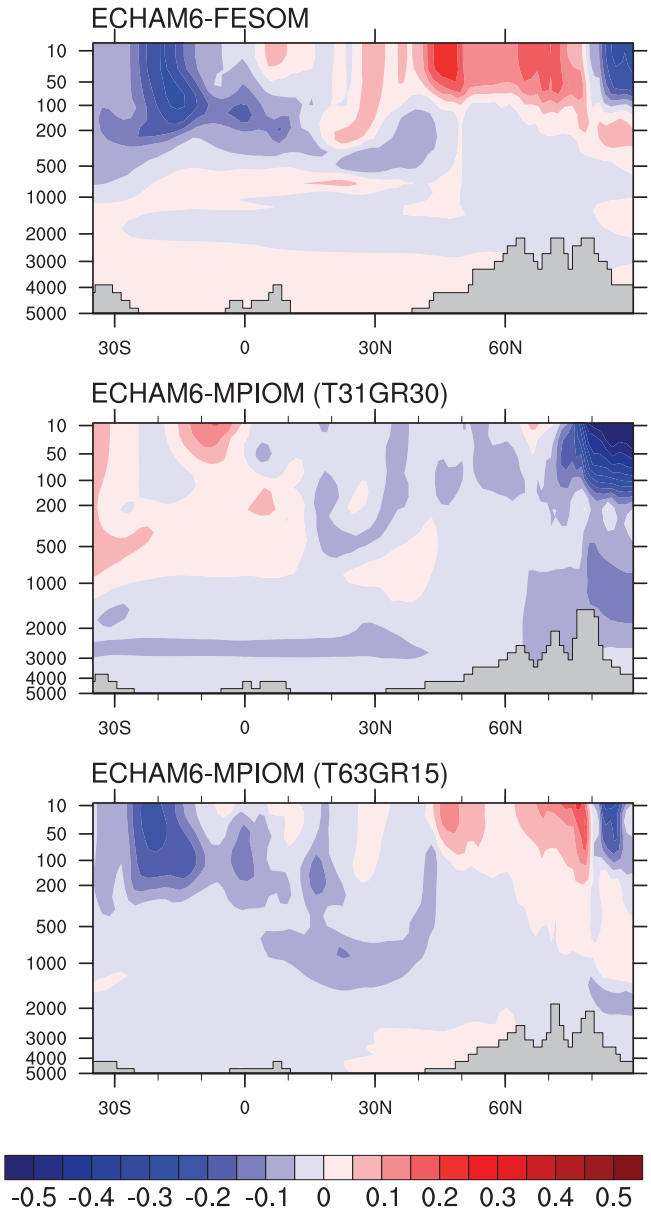

Fig. 3.18: *Simulated annual mean ocean salinity anomalies for the Atlantic region in the three models. Units are psu.*

equatorward deep western boundary current and the northward Gulf Stream [e.g., *Kwon and Frankignoul*, 2014]. In contrast, some former studies [e.g., *Ganopolski et al.*, 1998; *Otto-Bliesner et al.*, 2006; *Fischer and Jungclaus*, 2010; *Wei and Lohmann*, 2012], show a weakened AMOC in the mid-Holocene compared to that of the pre-industrial. The main reason for this inconsistency in AMOC change between our results and those others, lies on the different ocean salinity patterns simulated over the North Atlantic Ocean. The past studies show an decrease in ocean salinity in the upper layer of the North Atlantic Ocean, causing an increase in water mass density in the deep water formation sites, while our simulations indicate an increase in the water salinity/density over the regions of deep mixed layer owing to a change of precipitation minus evaporation which is linked to a tendency of positive North Atlantic Oscillation (NAO) mode, and to a sea ice dynamic process, namely, the decreased import of sea ice from the Arctic reduces the incoming fresh water to the Greenland Sea and Nordic Sea. In addition, by performing model simulation with mid-Holocene setup, *Rimbu et al.* [2003]; *Lohmann* [2016] associate such NAO tendencey with tropical warming during winter induced by increasing in solar insolation, similar to our results.

The main three models used in the present study all produce a tendency towards a positive NAO state in 6k, however, the response of Labrador Sea P-E to the NAO+ mode in ECHAM6-MPIOM (T31GR30) is opposite to that in other models, as precipitation exceeds evaporation happens in ECHAM6-MPIOM with T31GR30 grid, and the higher reasolution models (i.e., ECHAM6-MPIOM (T63GR15) and ECHAM6-FESOM) show the opposite case. There are clear indications that the North Atlantic Ocean varies significantly with the overlaying atmosphere, in particular the NAO [*Visbeck et al.*, 2003; *Scholz et al.*, 2014]. *Curry et al.* [1998] indicate that NAO variability has an influence on deep convection in the Labrador Sea. Changes in the mean circulation patterns over North Atlantic associatd with NAO are companied by changes in the intensity and number of storms, which are reflected in pronounced changes in the transport and convergence of atmospheric moisture and hence the P-E distribution [*Hurrell*, 1995; *Dickson et al.*, 2000]. In this paper, we argue that the NAO-induced P-E change leads to a response in the North Atlantic hydrological budget and further affects the overturning circulation. By ocean model simulations, *Häkkinen* [1999]; *Eden and Willebrand* [2001] suggest that NAO-related variations in the Labrador Sea heat flux induce a fast

response of the AMOC, with a delay of 2-3 years. Based on analyses of ocean observations and model simulations, *Latif et al.* [2006] conclude that the changes in the thermohaline circulation during last century is driven by low-frequency variations of NAO through changes in Labrador Sea convection. More recently, a delayed Oscillator model suggests that NAO forces AMOC on a 60 year cycle [*Sun et al.*, 2015; *Scholz et al.*, 2014].

Until recently, some (very sparse) efforts have been made to reconstruct the NAO and AMOC of mid-Holocene. For example, paleoenvironmental proxy data suggest a prominent role of NAO-like atmospheric variability during the Holocene beyond interannual to interdecadal timescales [*Lamy et al.*, 2006], which is attributed to the solar forcing. Using temperatures reconstructed from pollen data *Davis et al.* [2003] suggest a strongly negative NAO regime during the early Holocene (9-12ky BP) rising to a slightly positive NAO regime during the mid-Holocene, then decreasing to pre-industrial NAO. According to the ratio of Pa/Th, *McManus et al.* [2004] shows a brief decline in meridional overturning circulation from the mid-Holocene to 3000 years ago, and the AMOC at 6k and at present are of similar magnitudes. But there is uncertainty in the interpretation of AMOC by Pa/Th [*Keigwin and Boyle*, 2008], and a subsequent set of Pa/Th records suggested that a complete AMOC cessation during HS1 (Heinrich stadial event 1) was unlikely [*Gherardi et al.*, 2009]. The paleo reconstructions indicate that the uncertainties in the proxies data need to be reduced significantly to come to a final data-based conclusion about the past AMOC conditions [e.g., *Huybers et al.*, 2007; *Burke et al.*, 2011]. Moreover, there are reconstruction records suggesting an increase of ocean salinity over the North Atlantic Ocean [e.g., *de Vernal and Hillaire-Marcel*, 2006; *Came et al.*, 2007]. However, these reconstructions are based on a simple relationship between salinity and $\delta^{18}O$, which is an under-debate assumption [e.g., *Xu et al.*, 2013]. More recently, *Thornalley et al.* [2009] and *Rasmussen and Thomsen* [2010] show a slight decrease in North Atlantic salinity in 6k compared to the present. Based on the discrepancy of the reconstructed salinity, we discuss here that so far there is no robust conclusion for the 6k salinity change over North Atlantic. A better indicator might be the significant warming over the Gulf Stream, as observed by proxy data [*Lohmann et al.*, 2013], the 6k warming over the Gulf Stream is more pronounced than other regions in the North Atlantic Ocean. One can expect that with enhanced AMOC, the

associated northward transport of the relatively warmer and saltier sea water, largely increases the temperature and salinity over the region of Gulf Stream, where the maximum SST gradient occurs. Such interpretation is agreed by *Latif et al.* [2004] who uses the dipole SST anomaly pattern as a fingerprint to detect change in the North Atlantic thermohaline circulation.

The simulated AMOC anomalies are affected by changes in P-E, surface heat flux, sea ice growth/melt, transport of sea ice and liquid sea water from the Arctic, and the salinity-advection feedback related to AMOC itself. Here we propose a positive feedback between the Arctic sea ice and AMOC. The high phase of AMOC is found correlated to the increasing Northern Hemisphere surface air temperature (SAT) by numerous studies [e.g., *Schlesinger and Ramankutty*, 1994; *Rühlemann et al.*, 2004; *Knight et al.*, 2005; *Dima and Lohmann*, 2007; *Zhang*, 2007, 2008; *Chylek et al.*, 2009; *Mahajan et al.*, 2011; *Zhang*, 2015] by transferring advective heat flux into the Arctic interior through Fram Strait and the northern boundary of Barents Sea and Kara Sea. Therefore, the decreased mid-Holocene sea ice, can be both a cause and consequence of the enhanced AMOC. Moreover, the advective heat flux from the North Atlantic to the Arctic interior is found to be primarily confined to the Atlantic water, which is below the shallow mixed layer and the Arctic halocline in the Arctic basin, limiting the direct contact between ocean and atmosphere [e.g., *Steele and Boyd*, 1998]. Modeling studies suggest that multi-decadal variability in the AMOC strongly affects sea ice in the Arctic and particularly in the Barents Sea [*Delworth et al.*, 1997; *Jungclaus et al.*, 2005]. All of the three models used in this study exhibits sea-ice reduction in the Barents Sea, however, only T63-versions show a positive AMOC response. Therefore, the AMOC-sea ice-SAT feedback is not conclusive in the simulations analyzed in the present paper. Besides, a similar temperature-sea-ice-AMOC positive feedback has been also identified in hosing experiments in the North Atlantic Ocean [*Lohmann and Gerdes*, 1998], but without sea ice transport.

Another important component contributing to the positive feedback is the Fram Strait sea ice import into the GIN Sea. As a transition zone with no sea ice in the south and permanent ice cover in the north, the GIN region is a very important area in regulating the air-ocean interactions and heat exchange in horizontal direction. *Koenigk et al.* [2009] found that the interannual variability of sea ice volume in such transition

region is mainly determined by variations in sea ice import from the Central Arctic, which is governed by local winds, and dynamic process for sea ice growth/melt is of minor importance compared to dynamic sea ice transport. This finding to a centain degree coincides with our result, which reveals that the freshwater budget in the subpolar region depends on the Artic sea ice/freshwater transport, and the local radiation induced sea ice change plays a second role on the subpolar freshwater budget. The Fram Strait sea ice and water volume transport is sensitive to the atmospheric circulation in particular the surface wind over the Arctic Ocean [*Proshutinsky et al.*, 2015]. However, we observe no significant change in the surface wind and surface wind stress, therefore the reduction in sea ice volume import is mainly a consequence of the reduced Arctic sea ice. Analyzing paleoclimate data, *Müller et al.* [2009] conclude that changes in sea ice conditions in the Norwegian Sea are linked to regional and global climate anomalies and oceanographic circulation in the North Atlantic. A proper representation of these processes is therefore essential for simulating the climate response to external forcing.

Most CMIP5 models, as discussed in Section 3.5, show an enhanced AMOC in the mid-Holocene compared to present, in line with the result of ECHAM6-FESOM, but very few of them has been analyzed in previous studies [e.g., *Fischer and Jungclaus*, 2010; *Wei and Lohmann*, 2012; *Zheng and Yu*, 2013]. Results show a clear relationship between AMOC and SSS, as well as the vertical salinity profile. However, it is noted that the CMIP5 models show no obvious relationship with resolutions. In this paper we focus on the behavior of ECHAM6-FESOM, and ECHAM6-MPIOM in different resolutions. Therefore, exploring the specific mechanism for mid-Holocene AMOC change in other CMIP5 models is beyond the scope of this study.

3.8 Conclusions

In the present section, the climate conditions of the mid-Holocene and pre-industrial are simulated and compared. In good agreement with past studies [e.g., *Berger*, 1978; *Fischer and Jungclaus*, 2010; *Wei and Lohmann*, 2012; *Zheng and Yu*, 2013], we observe reduced sea ice and increased sea surface temperature in the polar regions, mainly induced by an increase in boreal summer solar insolation in 6k. However, we detect big discrepancies of simulated AMOC anomalies between models with coarse and higher res-

olutions. In detail, ECHAM6-FESOM and ECHAM6-MPIOM (T63GR15) both reveal a stronger-than-present AMOC in mid-Holocene, while ECHAM6-MPIOM T31GR30 shows the opposite case. Such model behavior lies on the different simulated salinity/density anomalies over the deep water formation sites, as the coarse resolution model (ECHAM6-MPIOM T31GR30) produces a freshening/less dense Nordic Sea and most part of the North Atlantic Ocean, while other two higher-resolution models depict pronounced salinification over the North Atlantic in particular the Labrador Sea, and the Greenland Sea. In addition, an earlier version of ECHAM6-MPIOM with T31GR30 grid (COSMOS, i.e., ECHAM5-MPIOM) shows very similar results to ECHAM6-MPIOM T31GR30 [*Fischer and Jungclaus*, 2010; *Wei and Lohmann*, 2012]. We thus conclude that the simulated AMOC response is closely related to model resolution.

The reason for such discrepancy in simulated AMOC anomaly (6k minus 0k) between models with different resolution is associated with both atmospheric and oceanic processes: First of all, all models produce a tendency towards a positive NAO state in 6k, however, the response of Labrador Sea P-E and surface heat flux to the NAO+ mode in ECHAM6-MPIOM (T31GR30) is opposite to that in other models, as positive P-E and net heat flux anomalies happen in ECHAM6-MPIOM with T31GR30 grid, and the T63 models show the opposite case. Secondly, all models produce a reduction in Fram Strait sea ice mass export, however, unlike other two models, the salinification induced by the reduced sea-ice transport in ECHAM6-MPIOM (T31GR30) only occurs over a small region in the Labrador Sea, and is partly compensated by the increased P-E over there. Finally, the coarse resolution model simulates much larger import of relatively fresh sea water from the Arctic to lower latitudes through Fram Strait in mid-Holocene compared to pre-industrial, whereas such anomaly in ECHAM6-MPIOM (T63GR15) is not significant.

Other CMIP5 models, although have approximately similar resolutions, show very different response of the AMOC to 6k boundary conditions. However, exploring the nature of such association in every specific CMIP5 model is beyond the scope of this study. A logical next step would be the comparison of CMIP5 model scenarios with different resolution to identify the resolution-dependent mechanisms for the Holocene AMOC change, and to identify which resolution is the key influencing factor—the atmospheric resolution, the oceanic resolution, or both.

4 Early-Holocene climate

4.1 Experimental design

In the following we describe the experimental setup of three simulations. A summary of the experiment characteristics is also provided in Table 4.1.

Using the circulation model ECHAM6-FESOM we perform several timeslice experiments: a pre-industrial control experiment (CTR) and four different early-Holocene runs (EH0k, EH9k, FWFC and FWFL), by prescribing the appropriate boundary conditions (Table 4.1). Orbital parameters are calculated according to *Berger* [1978]. In the CTR experiment, the GHGs are prescribed according to the Paleoclimate Modelling Intercomparison Project (PMIP) [*Crucifix et al.*, 2005]. For the early-Holocene simulations, the GHGs are taken from the ice cores [*Indermühle et al.*, 1999; *Brook et al.*, 2000; *Sowers et al.*, 2003]. In EH0k, we keep the topography the same as in the CTR, whereas the other early-Holocene experiments uses the topography at the early-Holocene based on reconstruction from the ice sheet model ICE-5G (VM2) [*Peltier*, 2004] which includes the prescribed Laurentide Ice Sheet (LIS) (Fig. **??**) and its feedback, involving surface albedo, elevation, and vegetation.

The effects of freshwater flux are examined in the group of simulations labelled FWFC and FWFL, in which we additionally prescribe a forcing of freshwater perturbation by adding 0.15 Sv (1 Sv $= 1 \times 10^6\ m^3/s$) freshwater pulse into the coastal region of LIS and the whole area of Labrador Sea, respectively. The total amount of released freshwater is about $4.67 \times 10^{14}\ m^3$, a value at the higher end of estimates of meltwater releases

Table 4.1: *List of experiments and boundary conditions*

Experiment	CTR	EH0k	EH9k	FWFC	FWFL
CO_2 (ppm)	280	260	260	260	260
CH_4 (ppb)	760	660	660	660	660
N_2O (ppb)	270	260	260	260	260
Eccentricity	0.016724	0.01928	0.01928	0.01928	0.01928
Obliquity	23.446	24.229	24.229	24.229	24.229
Precession	282.04	131.26	131.26	131.26	131.26
Topography	Present	Present	9ka B.P.	9ka B.P.	9ka B.P.
Freshwater flux	0	0	0	0.15 Sv (LIS coastal region)	0.15 Sv (Labrador Sea)
Integration Time	700	500	500	100 (hosing) +100 (recover)	100 (hosing) +100 (recover)

reconstructed for the 8.2 kyr BP event [*Von Grafenstein et al.*, 1998]. These different early-Holocene experiments enable us to distinguish the climate influences of the LIS and its melting.

The control experiment is initialized by the mean climatology from an Atmospheric Model Intercomparison Project (AMIP) and the data from the World Ocean Atlas (WOA). It is integrated for 460 years in T63L47 resolution (aboout $1.9° \times 1.9°$ degree, 47 vertical levels) for the atmosphere component, and varying resolution as shown in Fig. 2.1 with 46 vertical levels for the ice-ocean component. Both EH0k and EH9k simulations start from a 460-year mid-Holocene run, and are integrated for additional 500 years. Trends in sea surface temperature do not exceed $0.03°C/century$ for the last 200 model years, which is considered to represent the climatology in the respective simulation (Table 1). The FWFC and FWFL experiments starts from the EH9k experiment, integrates for 100 model years with freshwater perturbation, and another 100 years in which we stop the hosing and allow the disturbed ocean state to recover.

4.2 Surface temperature

The seasonal and annual mean climatology is calculated by averaging the corresponding parameters over the whole valid integration periods.

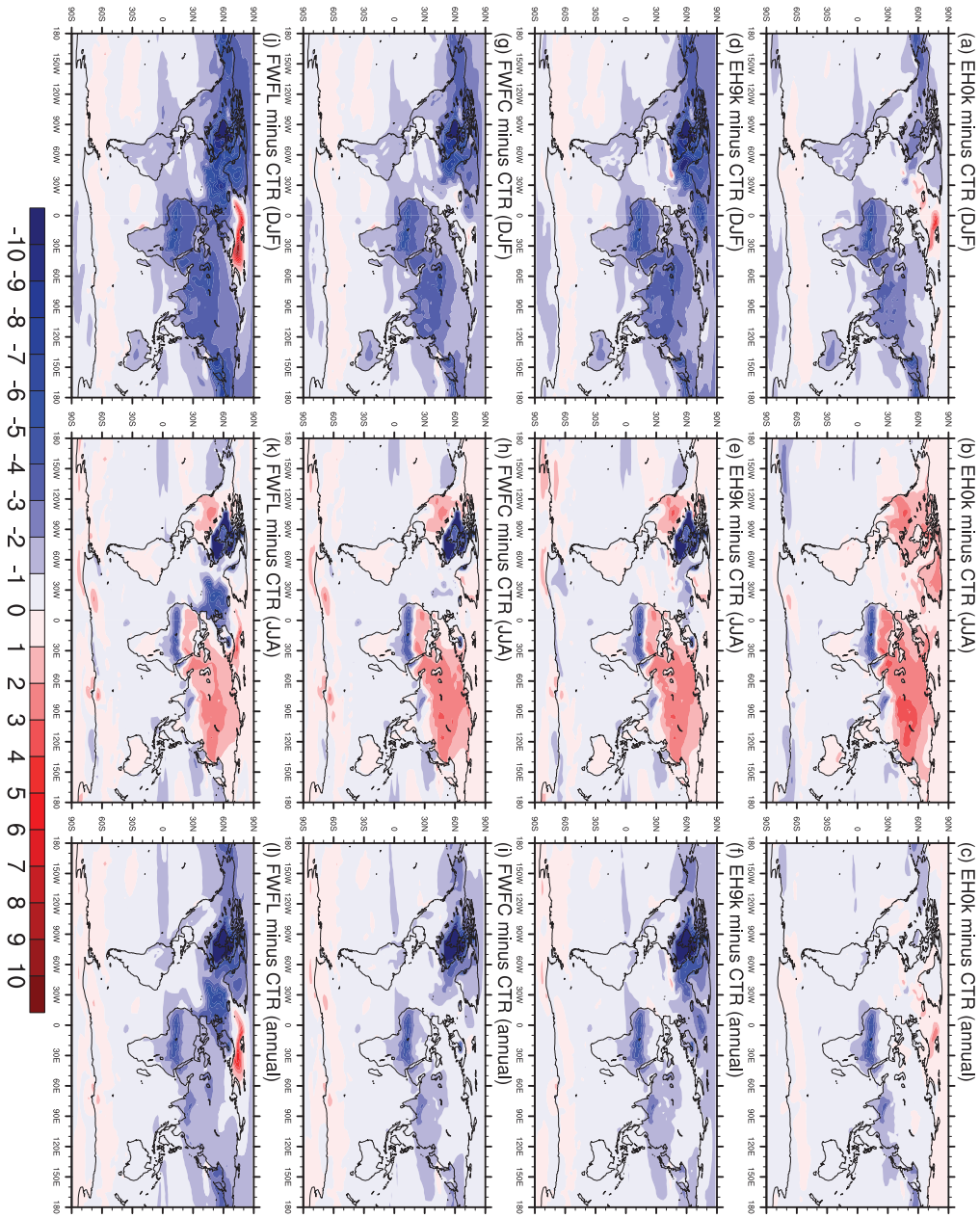

Fig. 4.1: *Simulated surface temperature anomalies relative to CTR in (a-c) EH0k, (d-f) EH9k, (g-i) FWFC and (j-l) FWFL for (left) DJF (December-February), (middle) JJA (June-August) and (right) annual mean. Units are K.*

The simulated surface temperatures are depicted in Fig. 4.1. Compared to the pre-industrial condition, a significant boreal-winter cooling up to -4 K forced by the negative DJF insolation anomalies is found over the North Hemisphere in EH0k (Fig. 4.1a), especially over North America, Eurasia and northern Africa. In boreal summer, the key feature possessed by EH0k is a general warming of about 3 K, which is more expressed over the Northern Hemisphere continents (Fig. 4.1b). The dominated cooling in the annual mean values results from a combined effect of the solar anomalies and the reduced GHGs (Fig. 4.1c), and the most pronounced cooling is found over the Sahel zone, which is related to both reduced insolation in boreal winter and increased precipitation in boreal summer. The above features resemble the mid-Holocene (6k) surface temperature anomalies [*Berger*, 1978; *Fischer and Jungclaus*, 2010; *Wei and Lohmann*, 2012] even though with a larger magnitude. This is reasonable, as the orbital forcing pattern is similar from early-to-mid Holocene, while gradually becoming smaller in amplitude.

Changes in the topography have a considerable global influence. In the EH9k experiment, a large cooling (more than -10 K) occurs over the prescribed continental ice sheet of North America throughout the year (Fig. 4.1d-f), which is attibuted to higher elevation and high surface albedo of the LIS. In boreal winter, the strong LIS cooling overcompensates the positive insolation anomaly and spreads further to the Baffin Bay, North Atlantic and the Arctic Ocean (Fig. 4.1d), dominating the annual mean values (Fig. 4.1f). Similar to EH0k, no significat change is found for the Antarctic continent and Southern Ocean in EH9k, indicating a minor effect of the increased Antarctic elevation. Similar results is revealed by a coarse resolution model COSMOS [*Wei and Lohmann*, 2012], except that a general Northern Hemisphere warming can be seen in their early-Holocene simulation, which is attributed to the sea level change in early-Holocene compared to the present.

The locations of freshwater forcing, as Laurentide meltwater input to the coastal region (FWFC), or iceberg discharges into the Labrador Sea (FWFL), lead to different responses of the modeled oceanic properties. In FWFC, the background melting of the LIS has no significant influence on the simulated surface temperature (Fig. 4.1g-i), since the anomalies distributions are very similar to the EH9k patterns. Adding freshwater into the whole Labrador Sea contributes to an additional cooling over the

North Atlantic Ocean, which leads to up to -5 K over this area as well as Scandinavia (Fig. 4.1j-l). Another intriguing feature is a local warming over the northern Nordic Sea. The mechanism for the different behaviors of these glacial freshening experiments lies on their different hosing routes, which is explored in the following section.

4.3 Large scale ocean circulation

The pre-industrial Atlantic meridional overturning circulation streamfunction, defined as the zonally integrated stream function over the Atlantic basin, has the averaged value of about 13.3 Sv ($1Sv = 10^6 m^3/s$) (Fig. 4.2), consistent with the estimates of global circulation from the hydrographic data [*Ganachaud and Wunsch*, 2000]. This value increases by 2.1 Sv and 2.6 Sv in the EH0k and EH9k experiment, respectively, indicating an important role of early-Holocene insolation and LIS on the strengthening of AMOC. No significant response of the overturning circulation is found when there is freshwater perturbation over the Laurentide coastal region. In contrast, we observe a spin-down of AMOC when the meltwater release occurs over the Labrador Sea, with a reduction to 60% of its pre-hosing strength within the first decade, and then a more gradual but continued decline over the next 90 years. In contrast to the gradual response during hosing period, the initial recover of AMOC is fast, reaching its pre-hosing state within 20 years. The strengthing of AMOC continues, with the maximal magnitude of 26 Sv happening after the next two decades. Then the AMOC spins down to its pre-hosing strength. To exmaine the AMOC responses to different early-Holocene forcings, in the following we perform an analysis on the elements affecting the freshwater budget of deep water formation sites of North Atlantic, involving the ocean temperature and salinity properties, net precipitaion, surface heat fluxes, as well as sea ice thermodynamic and dynamic processes.

4.3.1 Ocean temperature and salinity properties

The response of sea surface temperature (SST) to early-Holocene insolation and GHGs is depicted in Fig. 4.3a. The model produces a pronounced warming up to 2 K over the Nordic Sea and Labrador Sea, corresponding to the orbital anomaly in boreal summer.

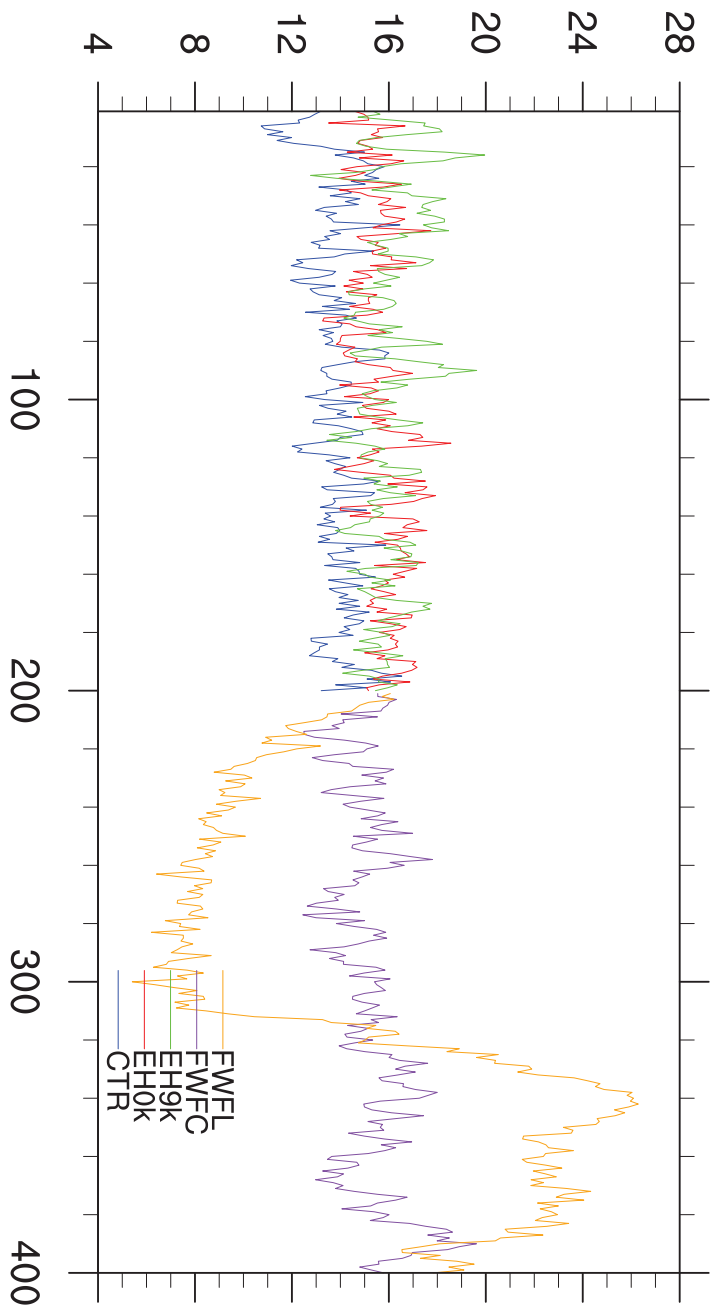

Fig. 4.2: *Simulated annual mean AMOC streamfuction distribution. Units are Sv.*

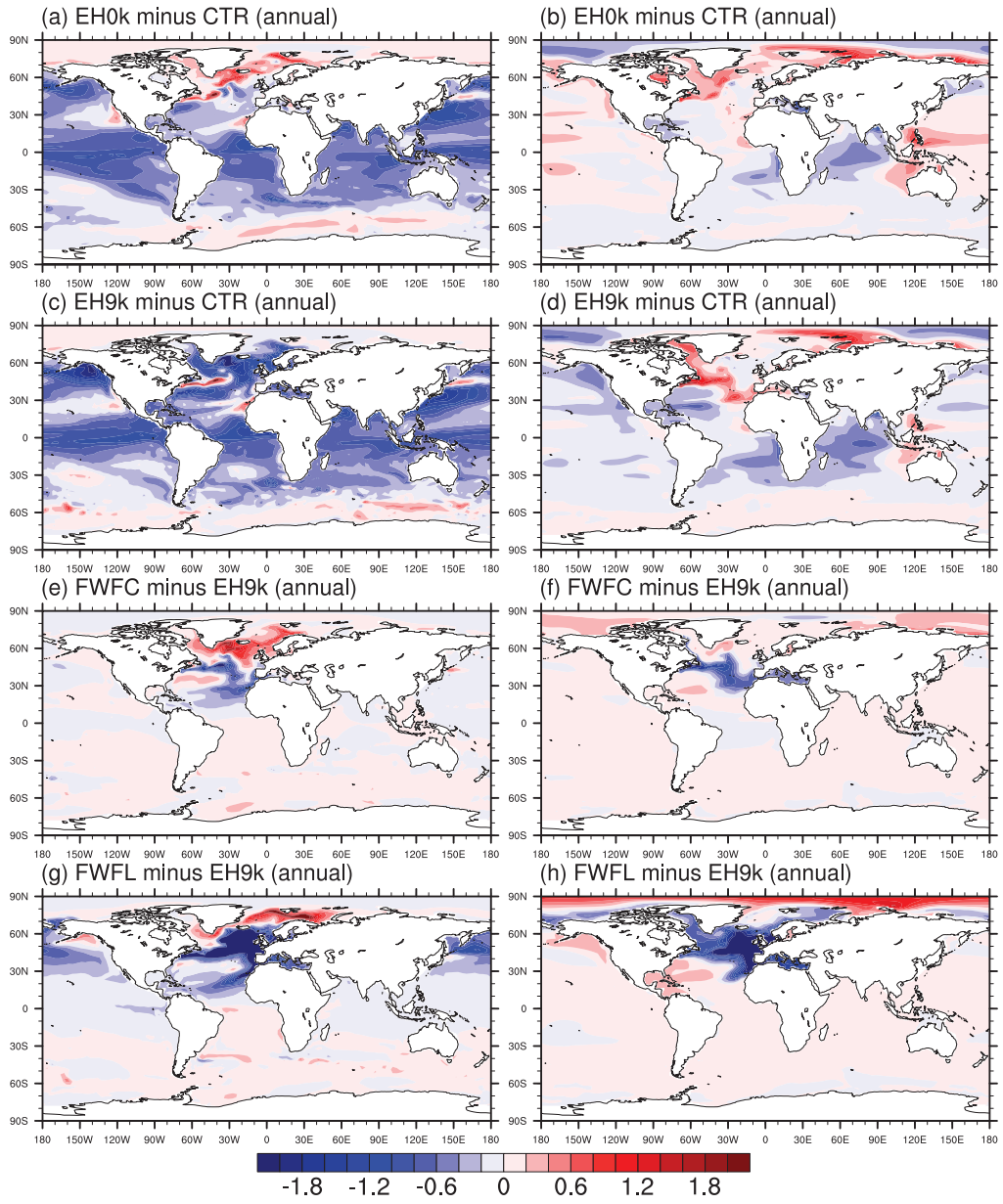

Fig. 4.3: *Annual mean anomalies of (left) sea surface temperature (units: K) and (right) sea surface salinity (units: psu).*

A general cooling is found over the tropical and sub-tropical regions, mostly induced by reduced insolation in boreal winter. Another important signal is an increase in the Southern Ocean SST, with a magnitude of up to 1 K, dominated by a large positive insolation anomaly from September to November. With the persistence of the LIS, an additional significant cooling is found over the North Atlantic and Nordic Sea (Fig. 4.3c), with the maximum value being larger than -2 K. A clear exception is the robust warming around the Gulf Stream, likely linked to an enhanced thermohaline circulation. In glacial melting experiment FWFC, sea surface temperatures are 1-2 K higher over the North Atlantic subpolar region around 60 °N and are 1-2 K lower along the route of Gulf Stream and Canary Current than in the simulation EH9k. In FWFL, sea surface temperatures are slightly warmer over the Labrador Sea than in EH9k, as the region is covered by sea ice and the freshening of sea water contributes to a higher freezing point. The route along Gulf Stream and the northestern Atlantic experience a significant cooling (larger than -2 K). In addition, a local increased temperature is found over the Greenland Sea, as a response to an enhanced southwestern wind flow and heat flux from the ocean sub-surface layer.

The annual mean sea surface salinity (SSS) anomalies are shown in the right panels of Fig. 4.3. Compared to the pre-industrial condition, the most intriguing large-scale features in EH0k include: 1) the salinification over the North Atlantic Ocean and Nordic Sea, 2) the increase and decrease in SSS over the equatorial Pacific and Indian Ocean, respectively, which are likely led by the corresponding change in precipitation, and 3) the general dilution over the central Arctic as a result of smaller sea ice production. With the existence of the LIS (Fig. 4.3d), EH9k simulates similar pattern, even though a more pronounced increase in salinity occurs over the North Atlantic, in particular the region of Gulf Stream with the maximal anomaly being larger than 1 psu. Glacial melting experiments reveal different SSS anomalies patterns, as FWFC indicates only a pronounced freshening along the Gulf Stream and Canary Current, whereas experiment FWFL shows a significant decrease in SSS over the North Atlantic, with the maximum anomaly being larger than -2 psu occuring over northeastern Atlantic, as well as a salinification over the Arctic Ocean at a magnitude of about 1 psu.

Fig. 4.4 and Fig. 4.5 present the meridional profiles of zonal mean ocean properties along the Atlantic section. A general cooling is found in EH0k and EH9k over 0-1000 m

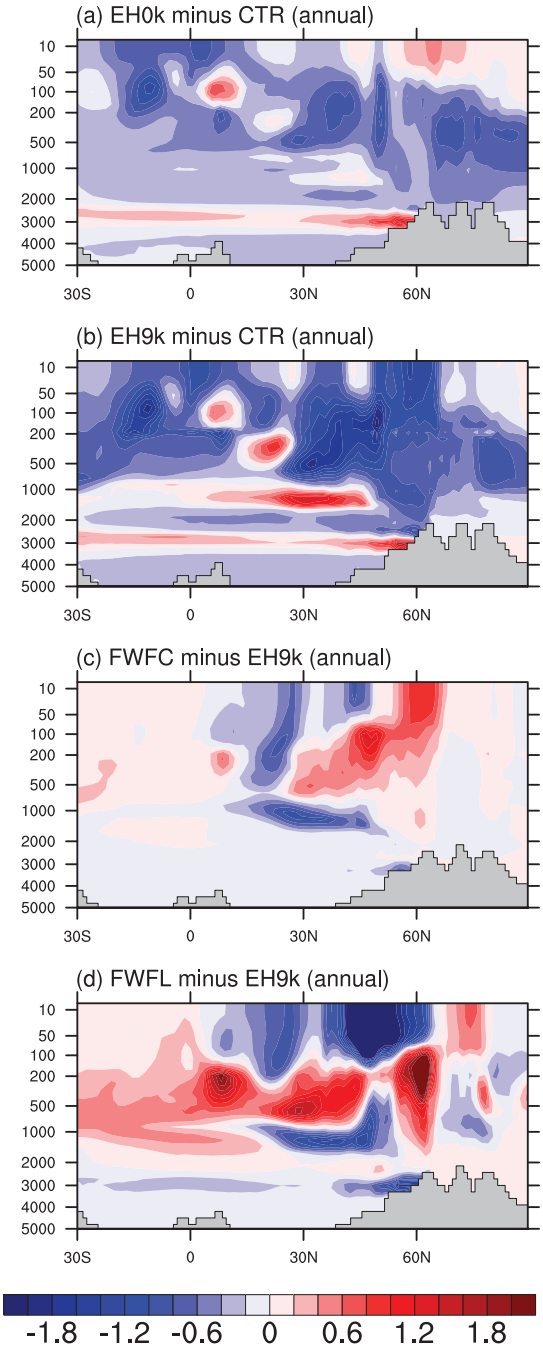

Fig. 4.4: *Annual mean anomalies of zonal temperature profile relative to CTR in (a) EH0k, (b) EH9k, (c) FWFC and (d) FWFL. Units are psu.*

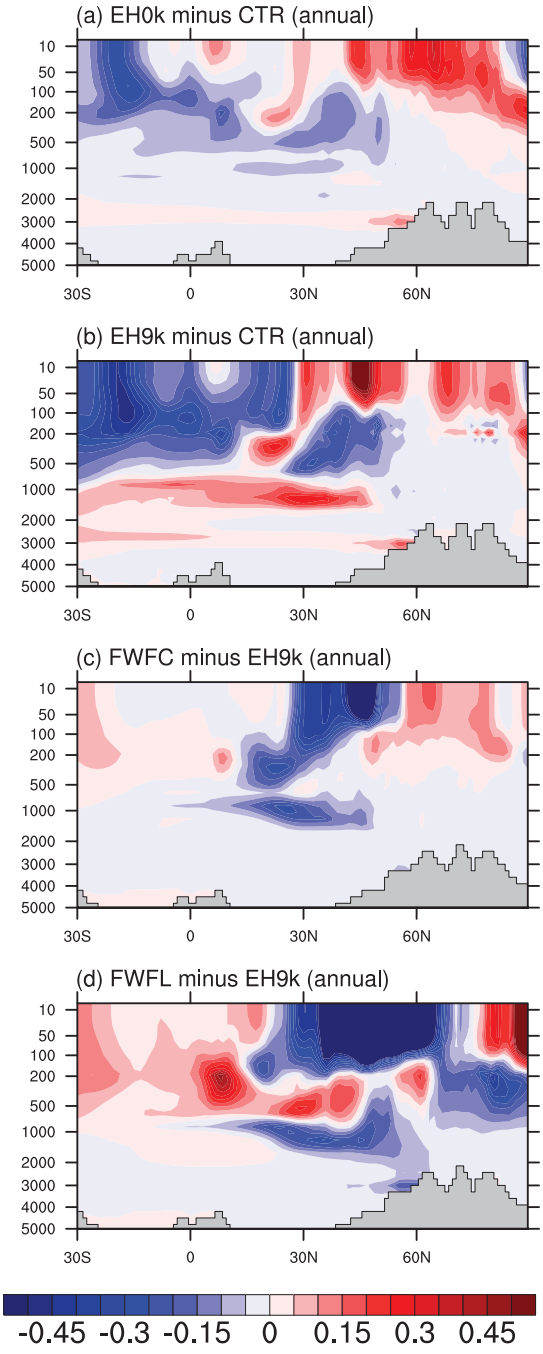

Fig. 4.5: *Annual mean anomalies of zonal salinity profile relative to CTR in (a) EH0k, (b) EH9k, (c) FWFC and (d) FWFL. Units are psu.*

depth, which is more pronounced with the prescribed Laurentide ice sheet. Moreover, salinification and freshening occurs over the upper ocean north and south of 30 °N, respectively, contributing to an increased meridional density gradient, which further results in a strenthening of the thermohaline circulation. In terms of the water mass properties of ocean interior in glacial melting experiments, there are common features shared by FWFC and FWFL about the cooling over depth of 0-200 m, the warming at 200-800 m, and the freshening over 0-200 m of North Atlantic. However, inconsistency emerge as the magnitudes and locations of the above-mentioned anomalies differ in FWFC and FWFL: 1) Surface cooling in FWFC is much less pronounced (up to -1 K) and restricted within 10-45 °N, whereas FWFL presents a cooling of more than -2 K which spreads to 60 °N. 2) The decrease in salinity of North Atlantic upper ocean has the mean value of -0.3 psu and -0.5 psu, happening over 25-55 °N and 20-75 °N in FWFC and FWFL, respectively.

The mechanism for the different response of ocean properties to the location of freshwater perturbation is as the follows. In FWFC, the west branch of Labrador Current transports the LIS coastal meltwater to the lower latitudes, therefore preventing a further advection of freshwater to the Labrador Sea. The freshwater mass is then merged into the Gulf Stream and Canary Current, forming a surface freshening tough which provides a lid on the sea water below, therefore suppresing the ocean convection. As a consequence, less heat is transferred from the upper branch of AMOC to the ocean surface, leading to an increase in temperature over depth of 200-800 m. As the warmer sub-surface water reaches higher latitudes, more heat is released and the upper ocean experiences a warming up to 1 K. In contrast, FWFL presents a surface freshening over the whole Labrador Sea, which advects to the surface and subsurface of North Atlantic Ocean. Such pattern of ocean salinity anomalies contributes to a decline of the AMOC, which further cools and freshens the upper ocean of North Atlantic, forming the well-known salinity-advection feedback [*Stommel*, 1961].

4.3.2 Precipitation minus evaporation (P-E)

All early-Holocene experiments show similar results in terms of the changes in precipitation minus evaporation (P-E) as depicted in the right panels of Fig. 4.6. Note that the evaporation anomalies (middle panels) are multiplied by -1 so the wet and dry condition

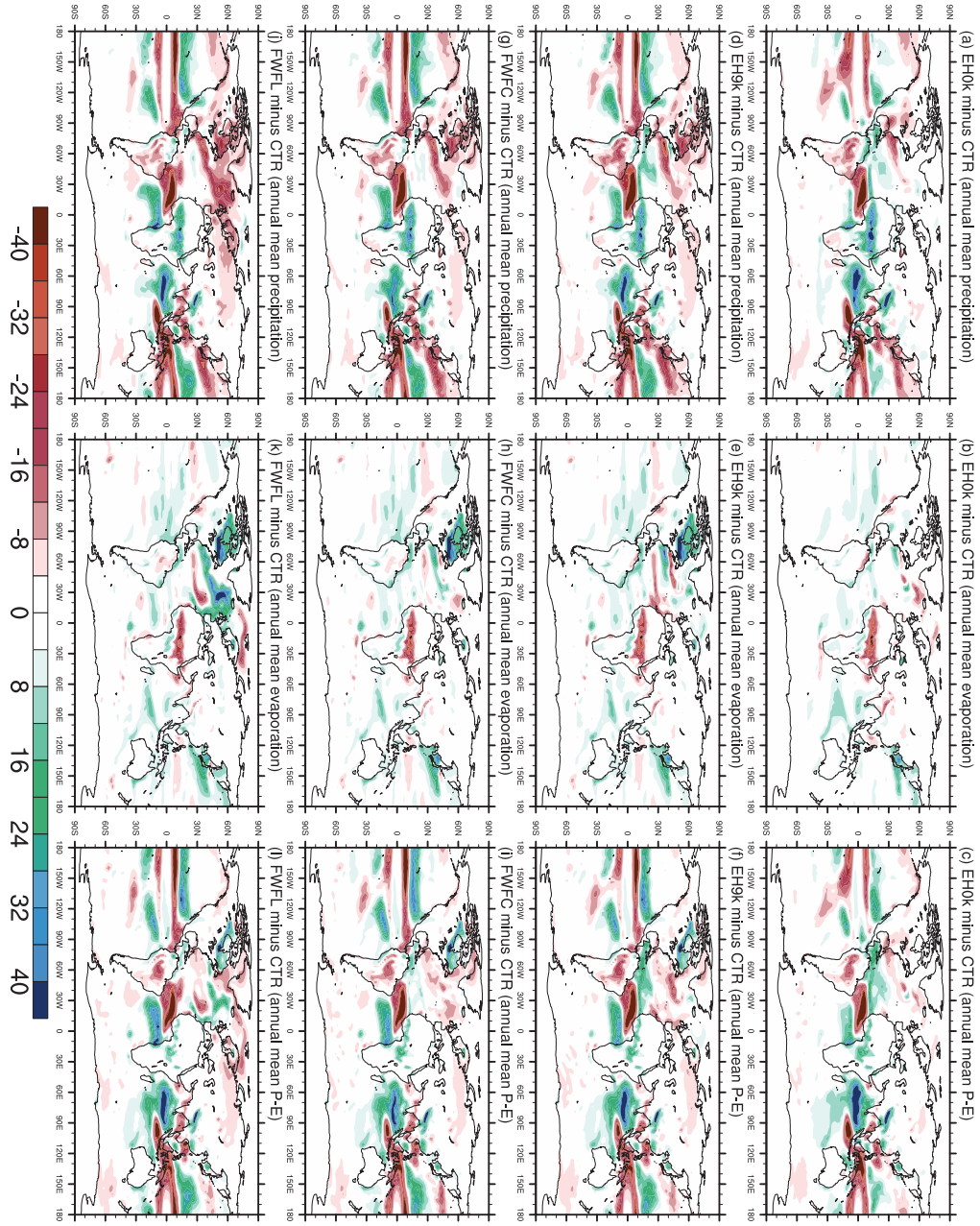

Fig. 4.6: *Simulated annual mean anomalies of (left) precipitation, (middle) evaporation, and (right) precipitation minus evaporation (P-E) relative to CTR in (a-c) EH0k, (d-f) EH9k, (g-i) FWFC and (j-l) FWFL. Units are mm/month.*

can be presneted by positive and negative values, respectively. Corresponding to the insolation change, the strongest P-E increase of up to 50 mm per month happens over the Sahel region and the western Indian ocean. This is dominated by the precipitation anomalies (left panels of Fig. 4.6), which is owing to the ocean feedback [*Kutzbach and Liu*, 1997; *Zhao et al.*, 2005] and monsoon response [*Herold and Lohmann*, 2009] to the increased insolation in boreal summer. The Africa and India sector, where such significant wetter condition occurs, is the northern edge of the intertropical convergence zone (ITCZ), therefore, the increase of the precipitation over these regions and the cooling along the equator favors a northward shift of the ITCZ [*Koutavas et al.*, 2006; *Haug et al.*, 2001]. Additionally, the increased cloud cover and the increased local evaporation both contribute to a cooling surface [*Braconnot et al.*, 2007]. The strongest annual mean P-E decrease of -40 mm per month occurs over the equatorial Atlantic and the eastern Indian Ocean near Indochina and south of Indonesia. In the tropical Pacific Ocean, P-E decreases by a maximum magnitude of -40 mm per month on an annual average. A different phenomenon in EH9k, FWFC and FWFL is the decrease of both precipitation and evaporation over the LIS region and its adjacent western Atlantic, as the cooling effect of the ice sheet contributes to a more stable atmosphere. Finally, it is noted that over the North Atlantic Ocean there is no significant P-E change but a local dryness over the southeast of Greenland in EH0k, while other early-Holocene experiments all illustrate negative P-E anomalies over the Labrador Sea, but with a small magnitude of less than -10 mm/month.

4.3.3 Sea ice processes

The simulated sea ice in all early-Holocene experiments experience an enhanced ablation and accretion over the central Arctic Ocean and Bering Sea, respectively, as shown in Fig. 4.7, in consistent with the temperature anomalies in boreal summer (Fig. 4.1b,e,h,k). With the cooling effect of the LIS, EH9k presents a pronounced sea-ice increase in the Baffin Bay and Labrador Sea, which leads to salinification and strengthening deep convection over those regions, contributing to an increase in the thermohaline circulation.

Coastal hosing has no obvious influence on the simulated sea ice (Fig. 4.7e-f, compared to Fig. 4.7c-d), as the meltwater flow mainly occurs along the Gulf Stream and Canary

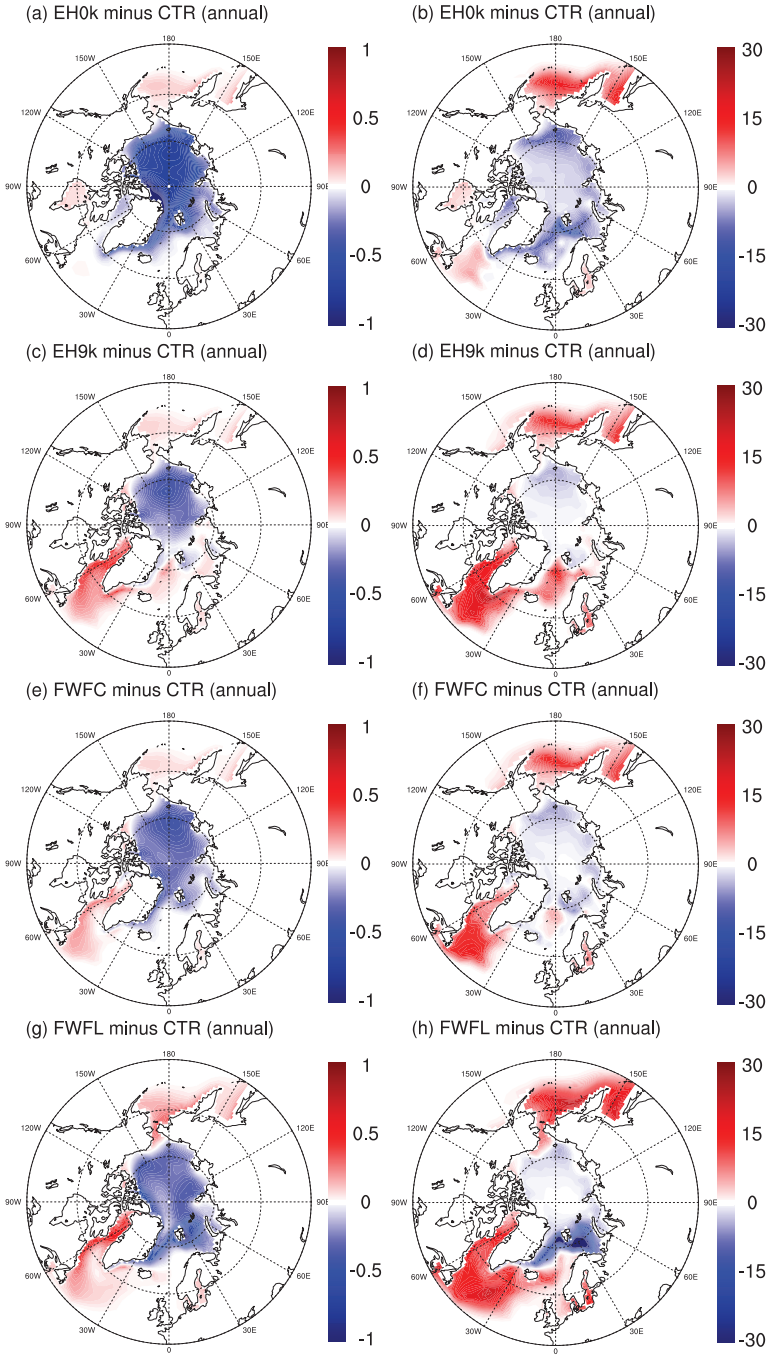

Fig. 4.7: *Annual mean anomalies of (left) sea ice thickness (units: m) and (right) sea ice concentration (units: %) relative to CTR in (a-b) EH0k, (c-d) EH9k, (e-f) FWFC and (g-h) FWFL.*

Current, therefore not affecting the deep water formation sites, whereas, freshwater pulse over the Labrador Sea leads to a significant increase in sea ice concentration over the North Atlantic subpolar gyre (Fig. 4.7h, compared to Fig. 4.7d). Besides, pronounced negative sea ice anomalies are found over the Nordic Sea and Barents Sea in FWFL, induced by a local warming there. In addition, no significant change in sea ice is found over the Southern Ocean in all early-Holocene experiments, except for a reduction in ice concentration in the Weddell Sea (not shown).

In summary, the stronger-than-present AMOC in EH9k and FWFC is partly a result of the salinification over the Baffin Bay and Labrador Sea induced by sea ice increase as a response to the cooling effect of LIS. Furthermore, the saline sea water advects to the North Atlantic subpolar region. Besides, the cooling effect of LIS also contributes to a denser North Atlantic Ocean. Larger sea ice production can also be seen in FWFL compared to CTR over the Baffin Bay and Labrador region, however, the freshening effect of iceberg discharge plays a dominate role. In experiment EH0k that presents no significant sea ice change over North Atlantic subpolar regions, it is important to consider the ice mass transport through Fram Strait (ICEFS) for studies of the net freshwater input into the Nordic Sea and North Atlantic subpolar gyres to examine the reason for the AMOC response. The time series of the annual means of this export (Fig. 4.8) shows significant negative anomalies in EH0k relative to CTR, accounting for an averaged ice volume export of 600 km^3/year larger in EH0k than the pre-industrial mean of 3060 km^3/year. The reduction in ICEFS origins from decreased sea ice volume in the Arctic. This ice export anomaly represents a loss of freshwater in the Nordic Sea and North Atlantic subpolar gyre (Fig. 4.3b).

The strength of the thermohaline cell to a certain extent depends on the amount of sea ice transported from the Arctic to the Greenland Sea and further to the subpolar gyre. Lag composite analysis between annual mean SSS and ICEFS, calculated by averaging the SSS anomaly fields that have more or less than one standard deviation with respect to indices of the Fram Strait ice mass import, is presented in Fig. 4.9. When low (high) ICEFS occurs, a pronounced increase (decrease) in SSS over the North Atlantic subpolar gyre is observed after 2 years in CTR, due to a comparably smaller (larger) freshwater import by sea ice. Composite map of SSS anomalies and ICEFS is similar in EH9k, therefore is not shown here.

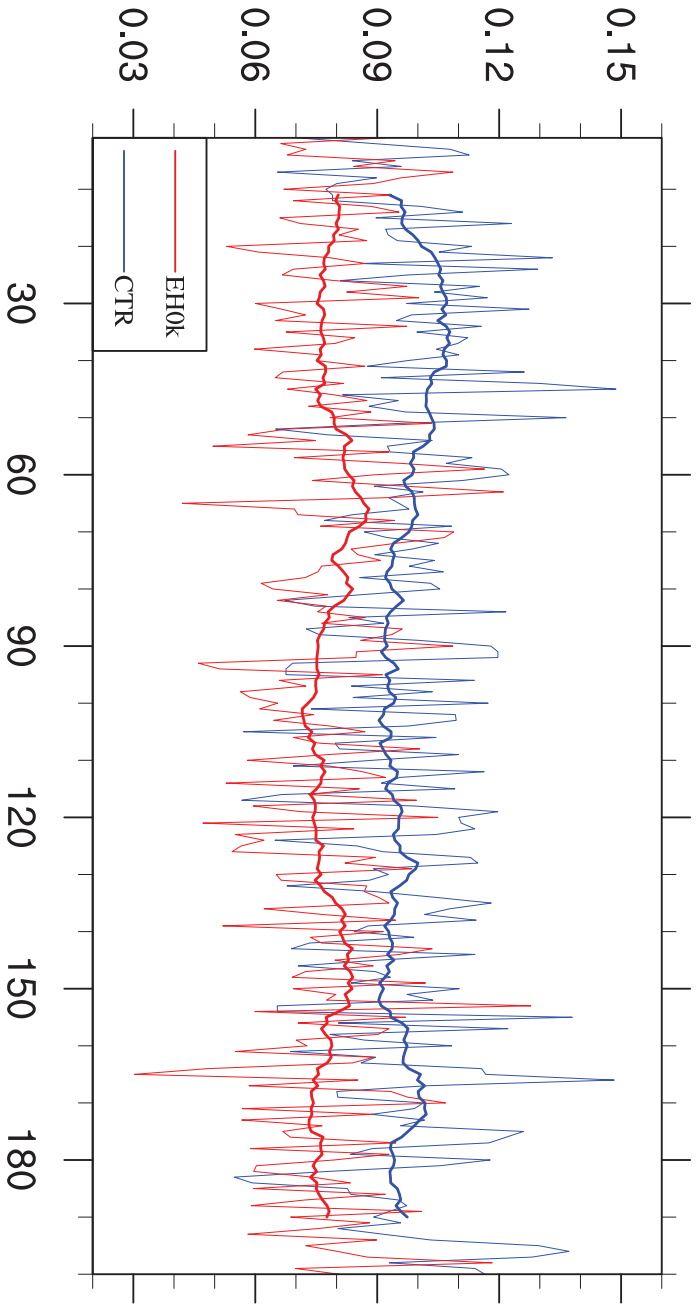

Fig. 4.8: *Time series of ice mass transport through Fram Strait in CTR and EH0k. A 21-year fliter is applies (thick lines). Units are Sv.*

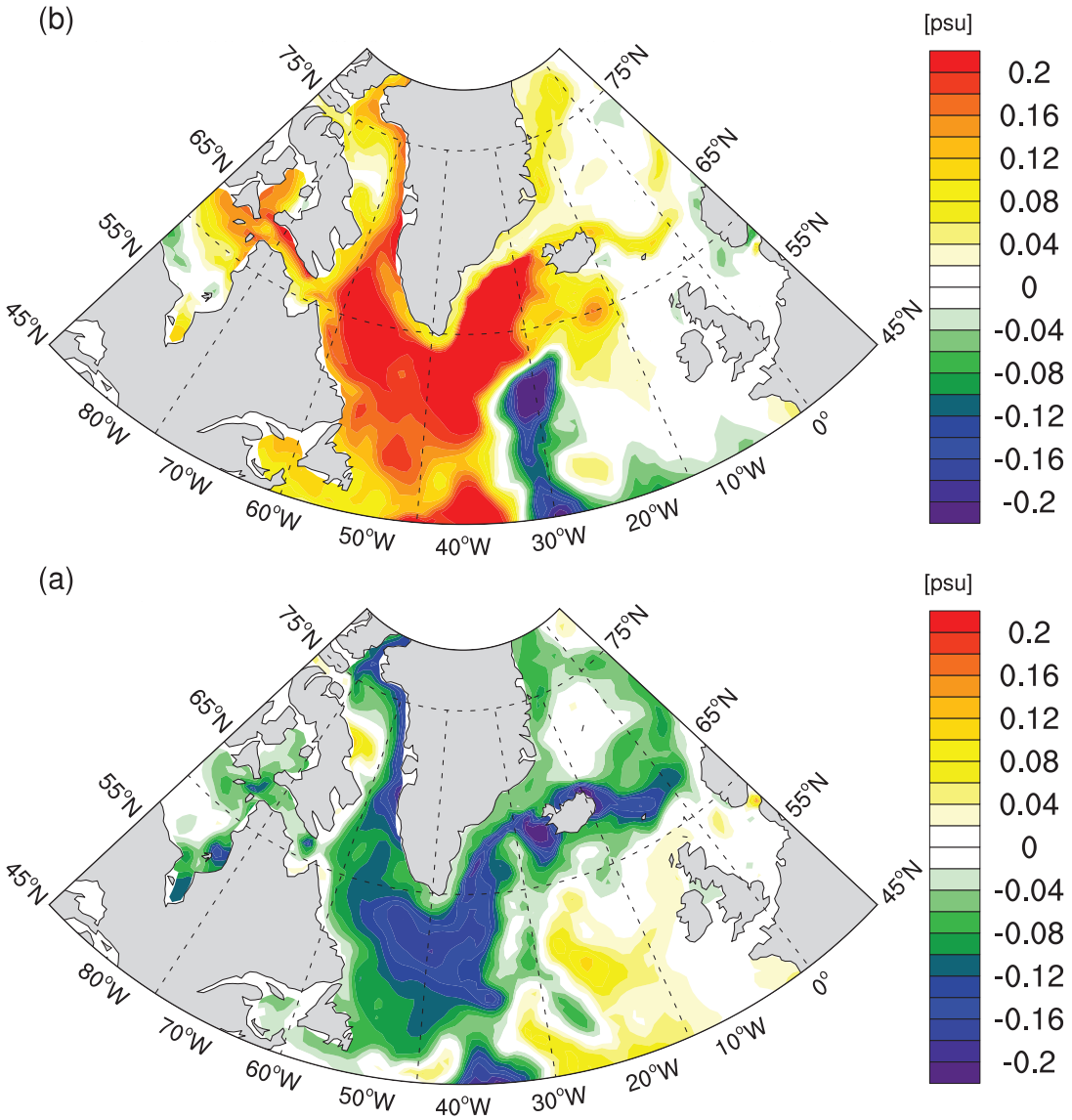

Fig. 4.9: *Composite maps of annual mean sea surface salinity anomalies during years of (a) low ICEFS and (high) ICEFS in the control experiment, with a lag of 2 years. Units are psu.*

4.4 Atmospheric circulation

4.4.1 North Atlantic Oscillation (NAO)

Fig. 4.10 depicts the changes in sea level pressure (SLP). Compared to the pre-industrial condition, all early-Holocene runs illustrate a North Atlantic Oscillation (NAO)-like mode, with negative SLP anomalies over the Greenland and Nordic Sea, and positive anomalies over North Atlantic Ocean. Such signal is relatively minor if only early-Holocene insolation and GHGs are applied, and is the most pronounced in EH9k. Another intriguing feature is a more negative Southern Annular Mode (SAM), which is more pronounced in EH0k. Additionally, the early-Holocene favors high SLP over Bering Sea, northern Africa and Euroasia.

4.4.2 Zonal wind

As indicated by previous studies, the NAO growth is significantly driven by transient eddy flux [*Feldstein*, 2003]. The strength of NAO reflects changes in the eddy-driven component, due to the action of transient eddy forcing to particularly accelerate the westerlies, thus barotropising the flow [*Hoskins et al.*, 1983; *Woollings et al.*, 2010]. In the present paper, we derive the Eliassen-Palm (E-P) flux [*Eliassen and Palm*, 1961; *Edmon Jr et al.*, 1980] to examine the changes of early-Holocene NAO and the conresponding zonal flow. The E-P flux is an indicator of both the flux of eddy activity and the eddy forcing of the zonal mean flow. The divergence of the E-P flux is a diagnostic tool for reflecting the change of zonal mean flow, as it is proportional to the eddy potential vorticity flux [*Eliassen and Palm*, 1961; *Edmon Jr et al.*, 1980]. In specific, net divergence (convergence) of E-P flux leads to stronger westerlies (easterlies); in the special case when the E-P flux divergence is zero, as for steady, frictionless, linear waves, thermal wind balance is maintained in an idealized zonally symmetric atmosphere.

To explore the responses of atmosphere circulation to different early-Holocene regimes, we examine the zonal wind anomaly as well as the E-P flux as illustrated in Fig. 4.11. All early-Holocene experiments favor 3 main features: 1) Enhanced westerlies happen around latitude 50°N over Atlantic section. Such wind anomaly further drives the air circulation from surface to the top of the troposphere, with the maximum value be-

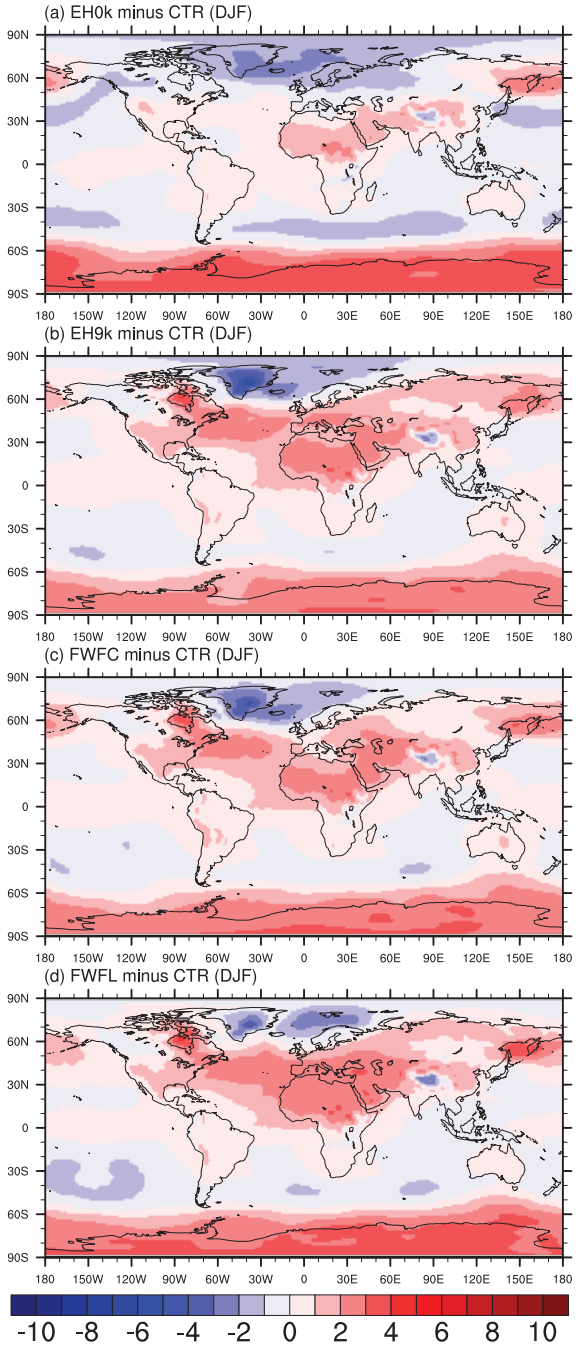

Fig. 4.10: *Simulated DJF (December-February) sea level pressure anomalies relative to CTR in (a) EH0k, (b) EH9k, (c) FWFC and (d) FWFL. Units are hPa.*

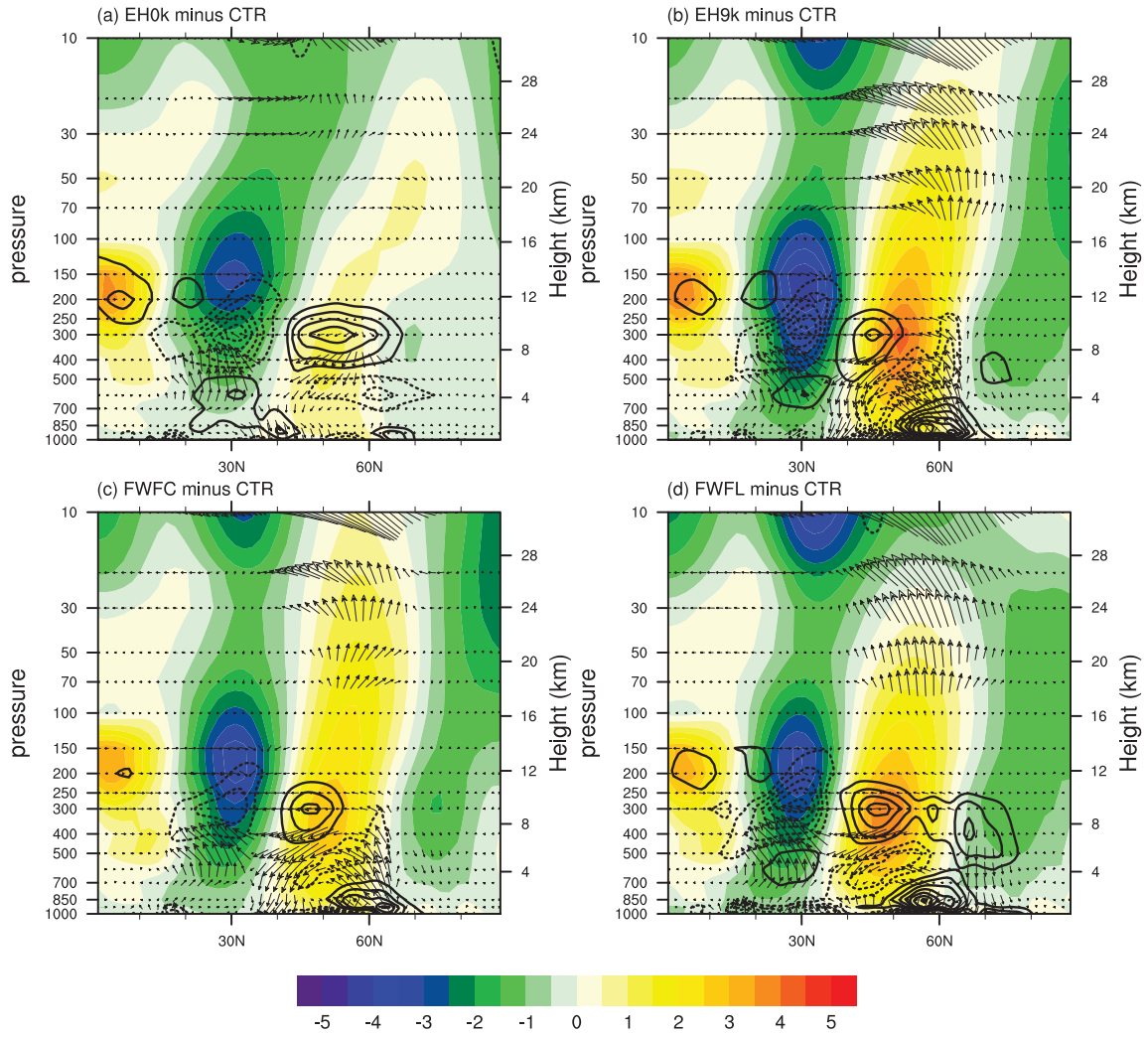

Fig. 4.11: *Simulated DJF (December-February) zonal wind anomalies (units: m/s) over the North Atlantic section (shading), the anomalies of the Eliassen-Palm flux (vector) and its divergence (contour) relative to CTR in (a) EH0k, (b) EH9k, (c) FWFC and (d) FWFL. Solid contour lines indicate net divergence and dashed contour lines represent net convergence.*

ing at about 300 hPa. This phenomenon is most pronounced in simulations with the LIS, as the LIS in ECHAM6-FESOM enhances the positive SLP anomaly over western North Atlantic Ocean. In detail, a large anomalous anticyclone dominates the surface flow over the ice sheet year-round. The northeast branch of the anticyclone constitutes into the westerlies over the North Atlantic, which forces the upper air circulation (not shown). 2) Another interesting feature is an weakened sub-tropical westerly flow which locates at 200 hPa in the latitude of about 30 °N, favored by the south branch of the anomalous North Atlantic anticyclone. 3) In addition, a more eastereard wind flow is found near the tropics, certering at 200 hPa.

The above 3 changes in the zonal flow are associated with the forcing of transient eddy component, as a net divergence , a net convergence and another relatively weaker divergence of E-P flux are found roughly over the three anomalies centers of Atlantic mean flow, owing to the anomalies distribution of meridional heat flux (vertical direction of E-P flux) and meridional flux of zonal momentum (horizontal direction of E-P flux).

4.4.3 Blocking event (BE), cold air outbreak (CAO) and snowfall

In this section, model daily output is used to analyze the behavior of blocking event (BE) and cold air outbreaks (CAO) under pre-industrial and early-Holocene regimes. Blocking events involves the formation of quasi-stationary, long-lived (more than 7 days), closed anticyclonic circulation that temporarily divert the prevailing westerly flow of air in troposphere [*Liu et al.*, 2012]. We define an atmospheric BE as an occurrence of five or more consecutive days during which the 500 hPa geopotential height is at least 1.5 standard deviations above the wintertime (1 December-28 February) mean value, following *Thompson and Wallace* [2001]. A CAO is an incursion of cold polar air into middle or lower latitudes, resulting in extreme negative anomalies of surface air temperature. It often occur downstream of high-latitude blocking anticyclones. Here we define a CAO as an event of at least three consecutive days during which the daily mean 2 m minimum temperature at a grid point is at least 1.5 standard deviations below the simulated winter-mean value at that location. The standard deviation used here is the average value of the 90 daily standard deviations of inter-annual 2 m minimum

temperature during the winter, following *Thompson and Wallace* [2001].

In agreement with re-analysis data [*Vavrus et al.*, 2006], pre-industrial BE acvitities produced by ECHAM6-FESOM, as shown in Fig. 4.12, present the most frequency over high latitudes. Moreover, the model generally simulate pre-industrial CAO most frequently over western North America and Europe and least commonly over the Arctic, consistent with observational estimate and other model results [*Vavrus et al.*, 2006]. These favored regions for CAO are located downstream from preferred locations of atmospheric blocking.

As the model is forced by early-Holocene boudary conditions, it generally simulates reduced CAO frequency over most of the Northern Hemisphere continents (right panels of Fig. 4.13), especially the eastern America and Eurasia by up to -50%. Such anomalies in CAO can generally be linked to associated changes in mean atmospheric circulation, as stronger westerly winds tend to weaken broader meanders that are likely to form blocking circulation. As can be seen in left panels of Fig. 4.13, there is a significant decreased incidence of BE during boreal winter over much of the high latitudes by more than 50%, with an amplification in EH0k and EH9k (up to 100%). The reduced blocing patterns favor less frequent incursions of Arctic cold air mass into lower-latitude continents, which further leads to a reduction in snowfall over Northern Hemisphere continents especially the Eurasia as shown in Fig. 4.14.

4.5 Discussion

The ice-ocean component FESOM has the advantage in the ability to provide a regional focus in a global setup [*Sidorenko et al.*, 2011]. The model has been validated in *Timmermann et al.* [2009]; *Scholz et al.* [2013]; *Sidorenko et al.* [2014], who indicated that the modeled and observational mean fields are in good agreement. Moreover, both monthly and daily outputs are analyzed.

The simulated global climate responses—including JJA warming, DJF cooling, reduction of the sea ice and wetter conditions at the Sahel and Sahara regions—are generally consistent with many previous studies [*Kutzbach and Gallimore*, 1988; *Kutzbach et al.*, 1996; *Weber*, 2001; *Renssen et al.*, 2005; *Wei and Lohmann*, 2012]. Note that, under the big background of DJF cooling, the model captures a regional warming over the

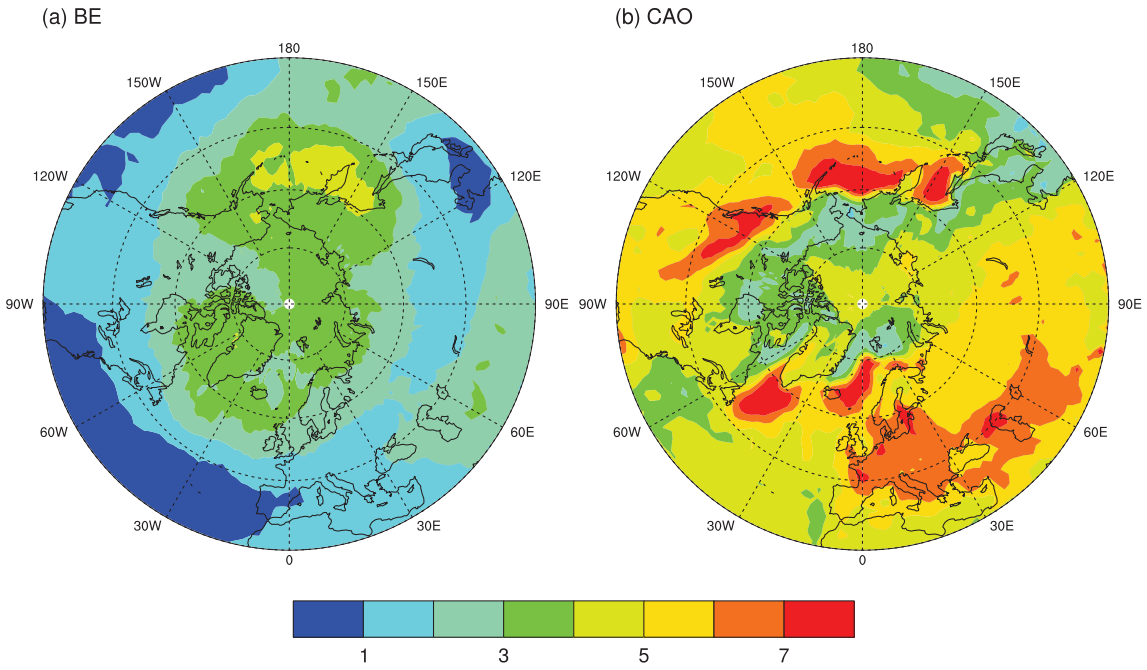

Fig. 4.12: *Simulated frequency (units: days/winter) of events of (a) blocking pattern and (b) cold air outbreak in the control experiment.*

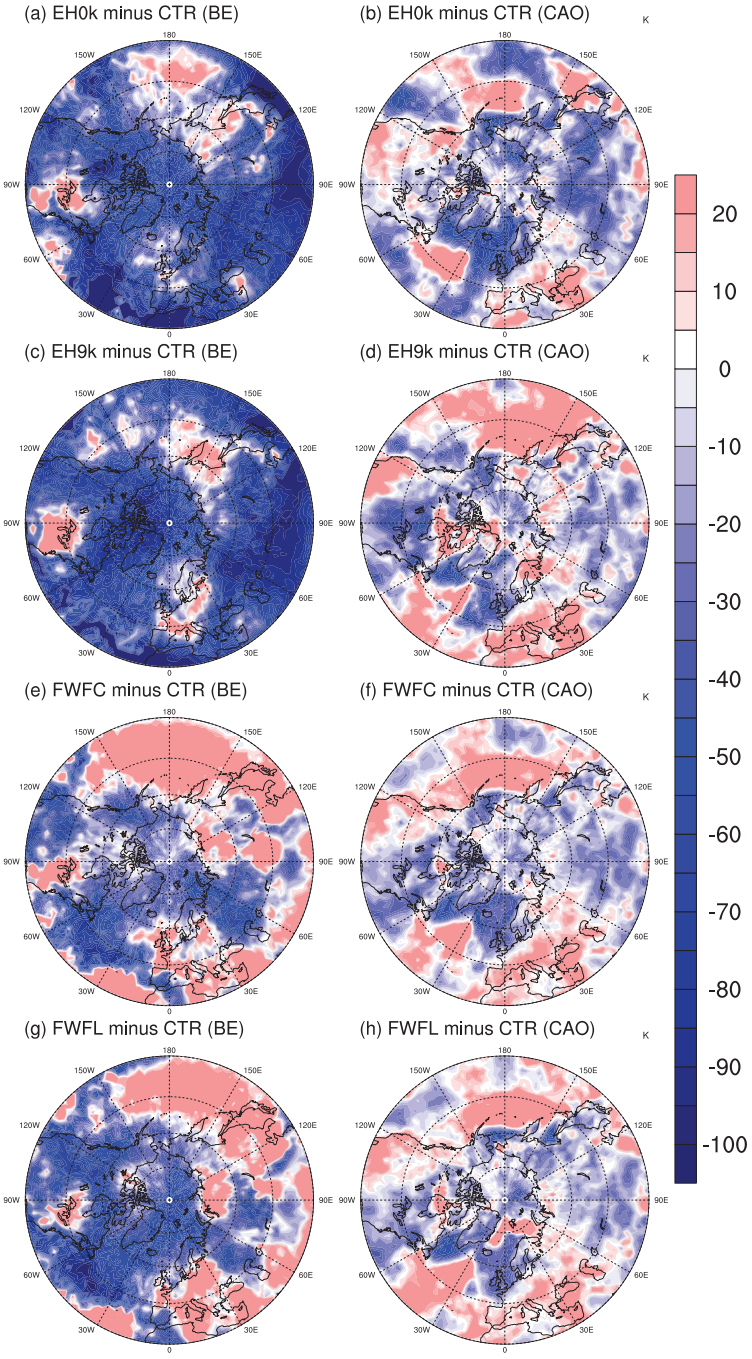

Fig. 4.13: *Simulated frequency anomalies of (left) blocking event and (right) cold air outbreak relative to CTR in (a-b) EH0k, (c-d) EH9k, (e-f) FWFC and (g-h) FWFL. Units are %.*

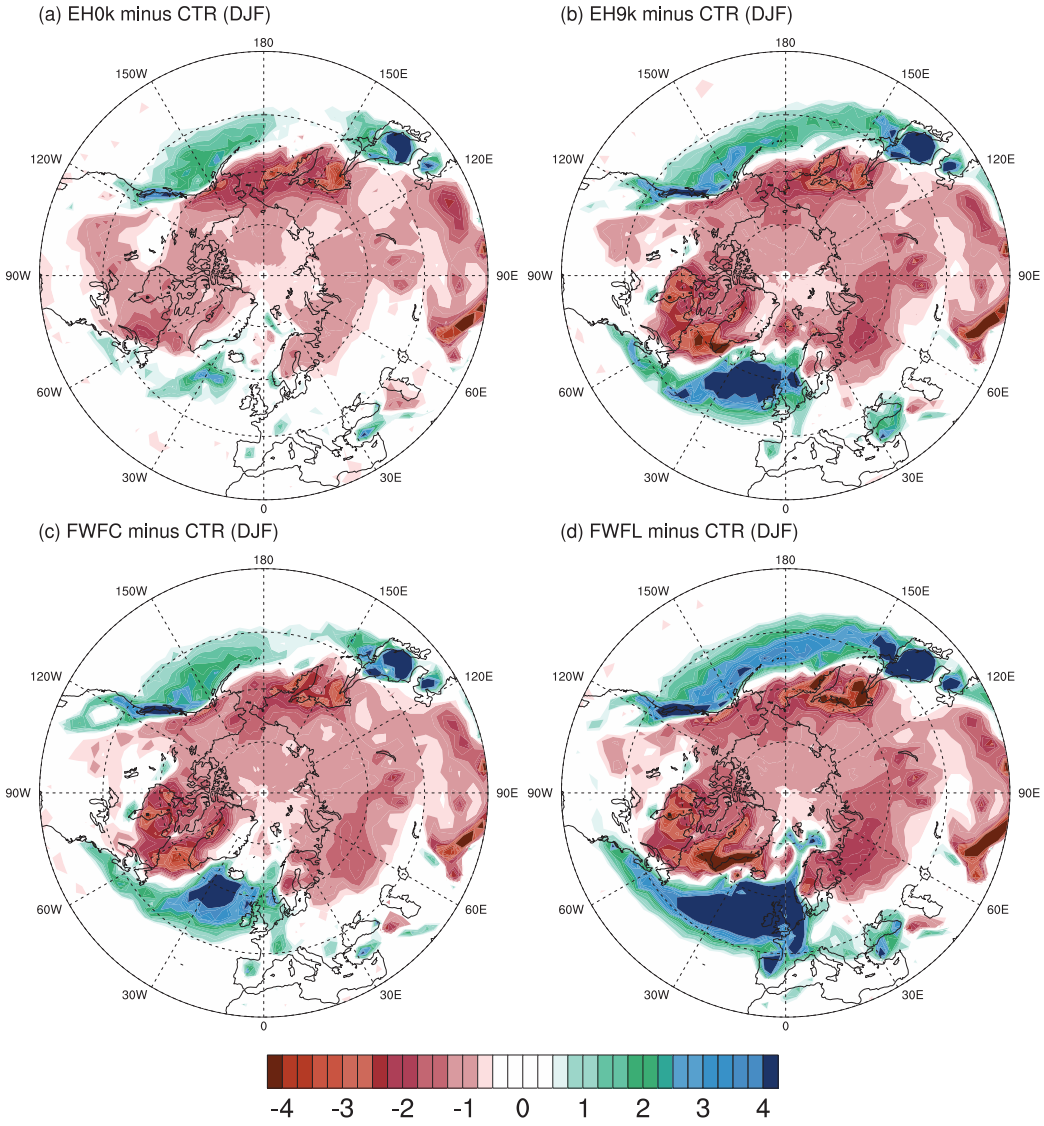

Fig. 4.14: *Simulated DJF (December-February) anomalies of snowfall relative to CTR in (a) EH0k, (b) EH9k, (c) FWFC and (d) FWFL. Units are mm/month.*

Greenland Sea, dominating the annual average values, which is in consistency with proxy records [*Lohmann et al.*, 2013].

The cooler and denser North Atlantic, together with the enhanced AMOC in our early-Holocene simulations, is in good agreement with proxy-based reconstructions [*McManus et al.*, 2004; *de Vernal and Hillaire-Marcel*, 2006; *Came et al.*, 2007; *Thornalley et al.*, 2009; *Rasmussen and Thomsen*, 2010]. In detail, proxy-based reconstructions show the possibility of a brief decline in meridional overturning circulation from the Holocene to present [*McManus et al.*, 2004]. Paleo-records suggests an increase of ocean salinity over Nordic Sea [*de Vernal and Hillaire-Marcel*, 2006; *Came et al.*, 2007; *Rasmussen and Thomsen*, 2010], indicating a strengthening AMOC in the Holocene. Core data from RAPiD-12-1K $(62°05N, 17°49W)$ presents a denser subpolar North Atlantic [*Thornalley et al.*, 2009], which also reflects a stronger-than-present AMOC. In terms of modeling results, *Wei and Lohmann* [2012] simulated a difference of 4 Sv between the AMOC of early-Holocene and pre-industrial using the coupled model ECHAM5-MPIOM with a coarse resolution. This value changes into -3 Sv when *Wei and Lohmann* [2012] removes the LIS from the early-Holocene conditions. The reduction of AMOC in their experiment is also consistent with a transient model integration [*Liu et al.*, 2014].

4.6 Conclusions

In the previous sections we have described the response of simulated oceanic and atmospheric circulation over Northern Hemisphere to different early-Holocene forcings, including the insolation and greenhouse gases, and their combination with the changed topography including the presence of the Laurentide ice sheet, as well as the meltwater flux which is added either into the LIS coastal region or the Labrador Sea. Our results are based on integrations performed with a state-of-the-art high-resolution model ECHAM6-FESOM. In our study, we mainly focus on the following two research questions:

4.6.1 How AMOC responses to the different early-Holocene forcings and what are the elements governing the change of AMOC?

When the early-Holocene orbital parameters and Greenhouse gases (GHGs) are applied, the modeled warmer Northern Hemisphere in boreal summer leads to an overall reduction in the Arctic sea ice volume, which resulted in a decline of Fram Strait sea ice import to the North Atlantic subpolar gyre. Significant salinification occurs over one of the main deep water formation sites, e.g., the Labrador Sea, as response to the decreased Arctic sea ice mass export, with a delay of 2 years. Finally, denser sea water of the upper ocean of North Atlantic leads to a strenthening of the thermohaline circulation.

With the early-Holocene topography, the Laurentide ice sheet (LIS) cooling is advected to the North Atlantic Ocean, causing a denser surface. Moreover, the cooling led by LIS allows more sea ice production over the Baffin Bay and Labrador Sea, resluting in a salinification of the sea water. The resulting enhanced AMOC in turn generates positive salinity (and density) anomalies. This well-known salinity-advection feedback is a positive feedback on the thermohaline circulation response at any time scale.

There are great discrepancies in the responses of the modeled oceanic properties with different locations of LIS meltwater flux, as Laurentide meltwater input to the coastal region, or iceberg discharges into the Labrador Sea. The former leads to a freshening over the Gulf Stream and Canary current, no obvious change is found in the properties of deep water formation regions and in the strength of AMOC, as the coastal meltwater is firstly transported to lower latitudes by the Labrador Currrent, with no advection to the far-field ocean. In contrast, the latter results in a significant surface cooling and freshening over the North Atlantic subpolar region, and a decline of AMOC with the maximum anomaly being up to -10 Sv.

4.6.2 How Northern Hemisphere atmosphere circulation responses to the different early-Holocene forcings and what might be the reason and influence of such change?

All early-Holocene experiments indicate a more positive North Atlantic Oscillation (NAO) pattern in the early-Holocene compared to pre-industrial, accompanied by intensified and weakened westerlies around 50°N and 30°N, respectively, in response to the transient eddy forcing. In detail, a net anomalous divergence and convegence of Eliassen-Palm (E-P) flux happens around 250 hPa, 50°N and 250 hPa, 30°N respectively, which is roughly consistent with the center of zonal wind anomalies. Such changes in mean atmospheric circulation tend to weaken broader meanders, therefore leading to a reduction in the blocking events and cold air outbreak. As a consequence, a decreased snowfall occurs over the Northern Hemisphere continents especially over the Europa and Asia.

In summary, using a finite-element high-resolution model, we simulate the responses of Northern Hemisphere oceanic and atmospheric circulation to different early-Holocene forcings involving the orbital parameters, greenhouse gases, topography and the background of ice sheet melting. Results indicate an important role of the presence of Laurentide ice sheet in the simulated climate and the position of freshwater pulse in the modelled reponse of thermohaline circulation.

5 Open-water ice growth

5.1 Experimental design

In the following section we describe the experimental setup of three simulations. Using the circulation model FESOM-ECHAM6 we perform three experiments FE-CTR, FE80 and FE120, with c_* being 100%, 80% and 120%, respectively. The control experiments FE-CTR is a 700 years simulation under pre-industrial boundary conditions [*Berger*, 1978; *Crucifix et al.*, 2005]. It is initialized by the mean climatology from the Atmospheric Model Intercomparison Project (AMIP) and the data from the World Ocean Atlas (WOA). A T63 grid (about $1.9° \times 1.9°$) with 47 vertical levels is applied in the atmosphere component ECHAM6. In terms of the ice-ocean module, FESOM uses a varying resolution from about 200 km in the open ocean to 20 km along coastlines (Fig. 2.1), with 46 vertical levels. The model has run into quasi-equilibrium with trends in global mean surface air temperature of the last 100 model years being no large than 0.002 °C/decade, which meet the quasi-equilibrium criteria as described in *Braconnot et al.* [2007]. The sensitivity experiments FE80 and FE120 are initialized from the control simulation, and integrated for 250 years. The average of the last 100 model years is considered to represent the climatology in all simulations. A summary of the experiment characteristics is also provided in Table 5.1.

Table 5.1: *List of experiments.*

Name	Value of c_*	Integration time
FE-CTR	100%	700(100)
FE80	80%	250(100)
FE120	120%	250(100)

5.2 Parameterization of ice concentration evolution

There are two main thermodynamic processes relating to changes in sea ice concentration: 1) freezing occurs on open water when sea water at its freezing point is cooled by the atmosphere, which reduces the open water area; 2) melting of sea ice (including both vertical and lateral melt) leads to a decrease in ice concentration [*Hibler*, 1979]. Furthermore, there are also some dynamic processes, such as divergence and ridging, that can affect the ice concentration evolution, which is however beyond the scope of our study.

The parameterization of ice-concentration evolution used in FESOM-ECHAM6 follows closely *Hibler* [1979]. Here only details on the improved equations and more sophisticated schemes by *Dorn et al.* [2009] are given. When new ice is formed on open water, the ice concentration increases at a rate given by:

$$\dot{A}_{ow} = \frac{1}{h_0} max(\dot{h}_{ow}, 0) \tag{5.1}$$

where $\dot{h}_{ow}$, the effective ice production rate at open water area, is calculated based on the open water energy budget.

The lead closing parameter h_0 in the equation is computed by:

$$h_0 = max({h_0}^{min}, min({h_0}^{max}, h)) \tag{5.2}$$

Here ${h_0}^{min}$ and ${h_0}^{max}$ are thresholds of demarcation ice thickness. Different from the fixed-value approach [*Hibler*, 1979] used in the standard ice growth scheme, FESOM-ECHAM6 uses a special case with ${h_0}^{min}$ and ${h_0}^{max}$ being 0.5 m and 1.5 m respectively. When melting of sea ice occurs, the decrease in ice concentration is based on the assumptions of *Hibler* [1979] that the sea ice thickness is uniformly distributed between

0 and two times of the actual sea ice thickness.

For further information on the ice concentration evolution in the model, it is referred to *Hibler* [1979].

In the present paper, we multiply $\dot{A}_{ow}$ by a factor c_* ($c_* = 80\%$ or 120%) to alter the horizontal-to-vertical aspect ratio of ice growth during the freezing period of open-water, as in

$$\dot{A}_{ow(new)} = \dot{A}_{ow} c_* \tag{5.3}$$

By performing such modification, the lateral ice growth within open water is changed (Fig. 1.1). Taking into account the mass conservation, the actual sea ice thickness is automatically adjusted by the model.

5.3 Climatological sea ice and Atlantic Meridional Overturning Circulation (AMOC)

Fig. 5.1 provides a seasonal picture of mean ice thickness conditions throughout the Arctic. It clearly shows areas of thick ice floes (mean thickness larger than 5 m) over the north side of Greenland and the Canadian Archipelago. Such pattern is mainly due to the Beaufort Gyre and Transpolar Drift Stream which tend to push the ice pack around the Arctic Ocean in a clockwise direction, causing the ice to the north to pile up along the natural barriers to this flow. The thick-to-thin ice gradient is clearly captured by the model from the Canadian Archipelago (5.5 m) towards the Siberian coast (less than 1 m). In September, the sea ice retreats from subpolar North Atlantic and Bering Strait to the Arctic Basin north of $50°N$. It is obvious that Southern Ocean sea ice is generally thinner than its counterpart in the Arctic. In the model simulations, most Southern Ocean ice is thinner than 2 m. In March, the sea ice only occupies the Weddell Sea and Antarctic coastal regions, while in September the sea ice extends further to $60°S$.

Fig. 5.2 presents the mean sea-ice concentration of the model in FE-CTR. The Arctic sea ice in winter reveals a large coverage over the entire central Arctic region. The 15% boundary of the winter sea-ice concentration extends into the Barents Sea up to $75°N$, and along the east coast of Greenland and the Labrador Peninsula up to $53°N$. The

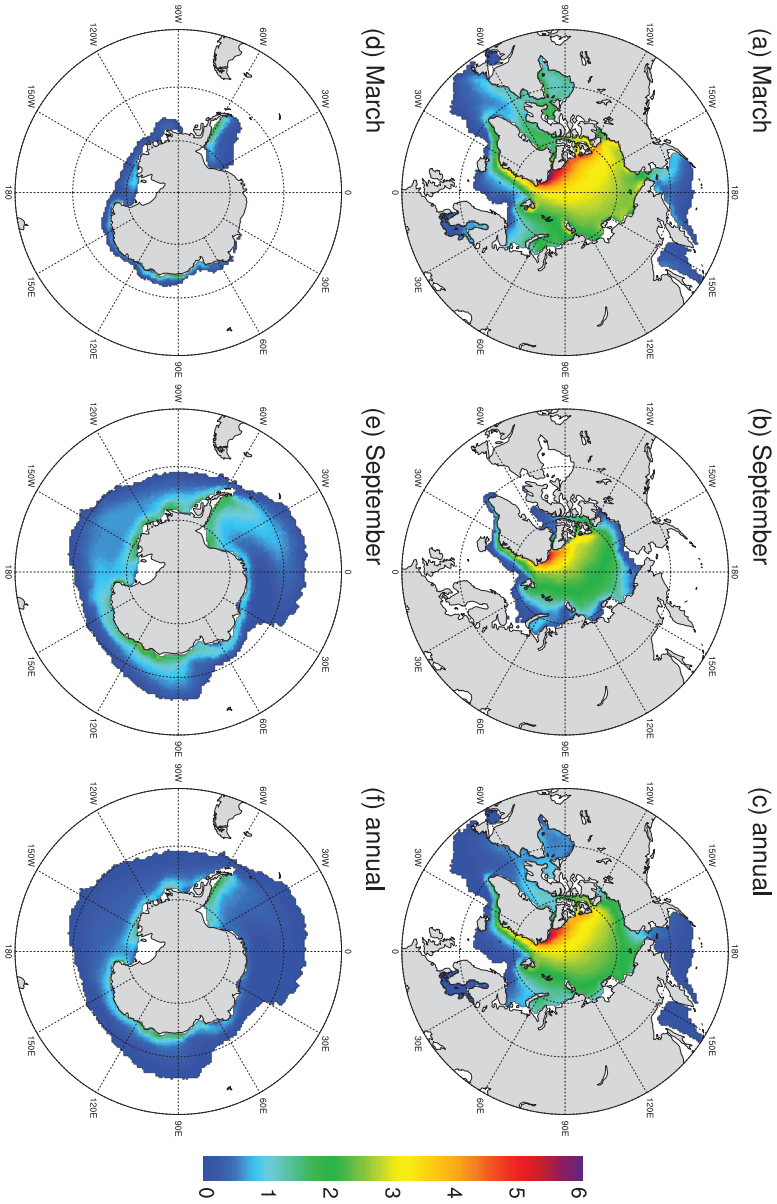

Fig. 5.1: *Distribution of sea ice thickness for FE-CTR, units are m.*

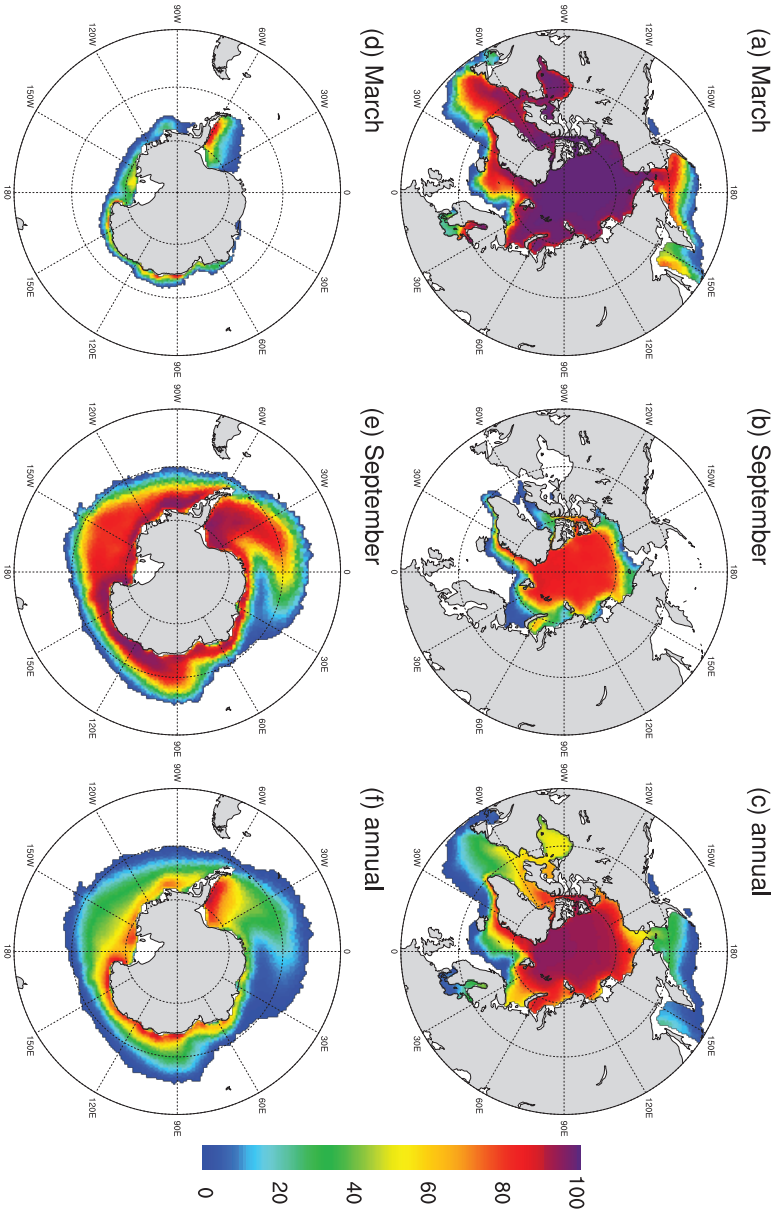

Fig. 5.2: *As in Fig. 5.1, but for sea ice concentration, units are %.*

pronounced retreat in the summer Arctic sea-ice coverage is clearly seen. The ice concentration over the Southern Ocean reaches its maximum along the coastal regions of Antarctic continent and minimum in the Marginal Ice Zone (MIZ).

Generally, the sea ice distributions in FESOM-ECHAM6 in both hemispheres are similar to reanalysis and observational estimates [*Zhang and Rothrock*, 2005; *Fetterer et al.*, 2002] despite the following two aspects: 1) The Arctic Sea ice is relatively thicker compared to reanalysis data [*Zhang and Rothrock*, 2005], with amplification over the Greenland Sea. The large bias in the Greenland Sea is possibly linked to the Transpolar Drift Stream between Beaufort and Barents Gyres. 2) There is extensive winter sea ice cover in the Labrador Sea, the reason of which is currently unknown [*Sidorenko et al.*, 2014].

In control experiment, the Atlantic meridional overturning circulation (AMOC) stream-function, defined as the zonally integrated stream function over the Atlantic basin, has the maximum of 12-13 Sv (1 Sv = 10^6 m^3/s) at 1000 m depth of 35°N (Fig. 5.3), relatively weaker and shallower than the estimates of global circulation from the hydrographic data (about 15 Sv) [*Ganachaud and Wunsch*, 2000] and the results of most other coupled climate model including ECHAM6-MPIOM [e.g., *Danabasoglu et al.*, 2014]. An important reason for such model behavior lies on the freezing of the Labrador Sea, which limits the deep convection there. Visa versa, the simulated excessive sea ice over the Labrador Sea could also be partly a result of the relatively weak AMOC, as the strength of AMOC is significantly correlated to the North Atlantic subpolar temperature [e.g., *Schlesinger and Ramankutty*, 1994; *Rühlemann et al.*, 2004; *Knight et al.*, 2005; *Dima and Lohmann*, 2007; *Zhang*, 2007, 2008; *Chylek et al.*, 2009; *Mahajan et al.*, 2011; *Zhang*, 2015].

5.4 Changes in ice thickness and ice concentration

Compared to FE-CTR, there is an increase in sea ice thickness in FE80 over the entire Arctic (Fig. 5.4a-c), with the maximum change of about 0.8 m occurring over the coastal region north of Greenland, where sea ice reaches its maximal thickness. The reason for such pronounced change is simply a reflection of the increased advection of sea-ice volume from the central Arctic. Similarly, decreasing the value of $\dot{A}_{ow}$ in the Southern

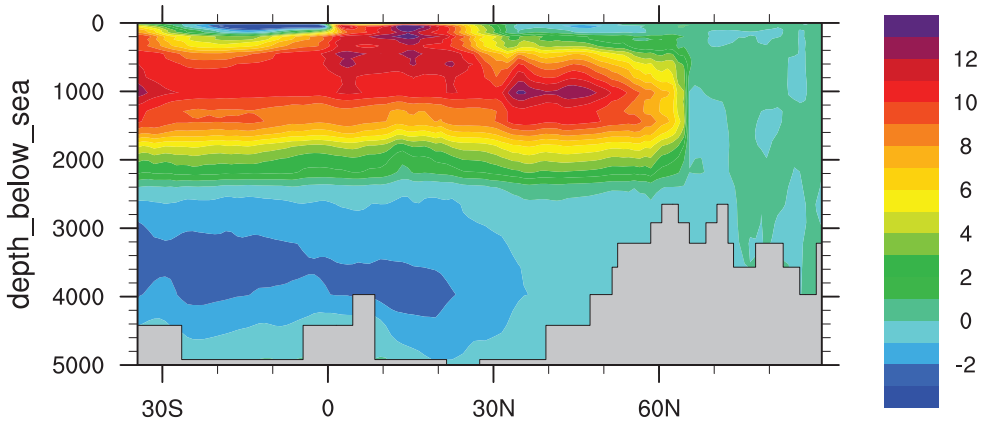

Fig. 5.3: *Simulated AMOC streamfunction in FE-CTR, units are Sv.*

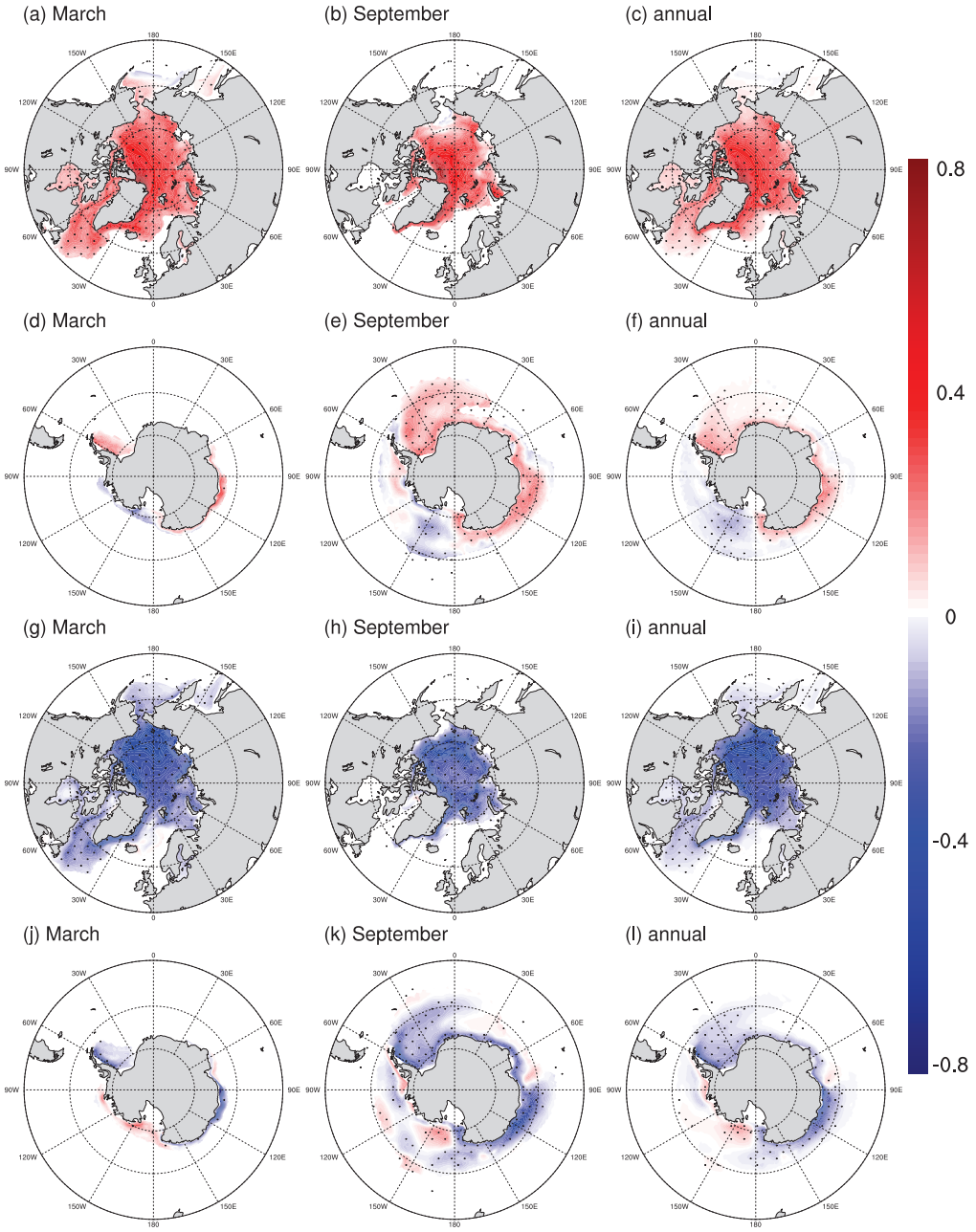

Fig. 5.4: *(a-f) Sea ice thickness amomalies of FE80 compared to FE-CTR, units are m. Hatched regions have >95% significance level based on Student's T test, which takes into account the auto-correlation. (g-l) As in (a-f), but for sea ice thickness amomalies between FE120 and FE-CTR. Units are m.*

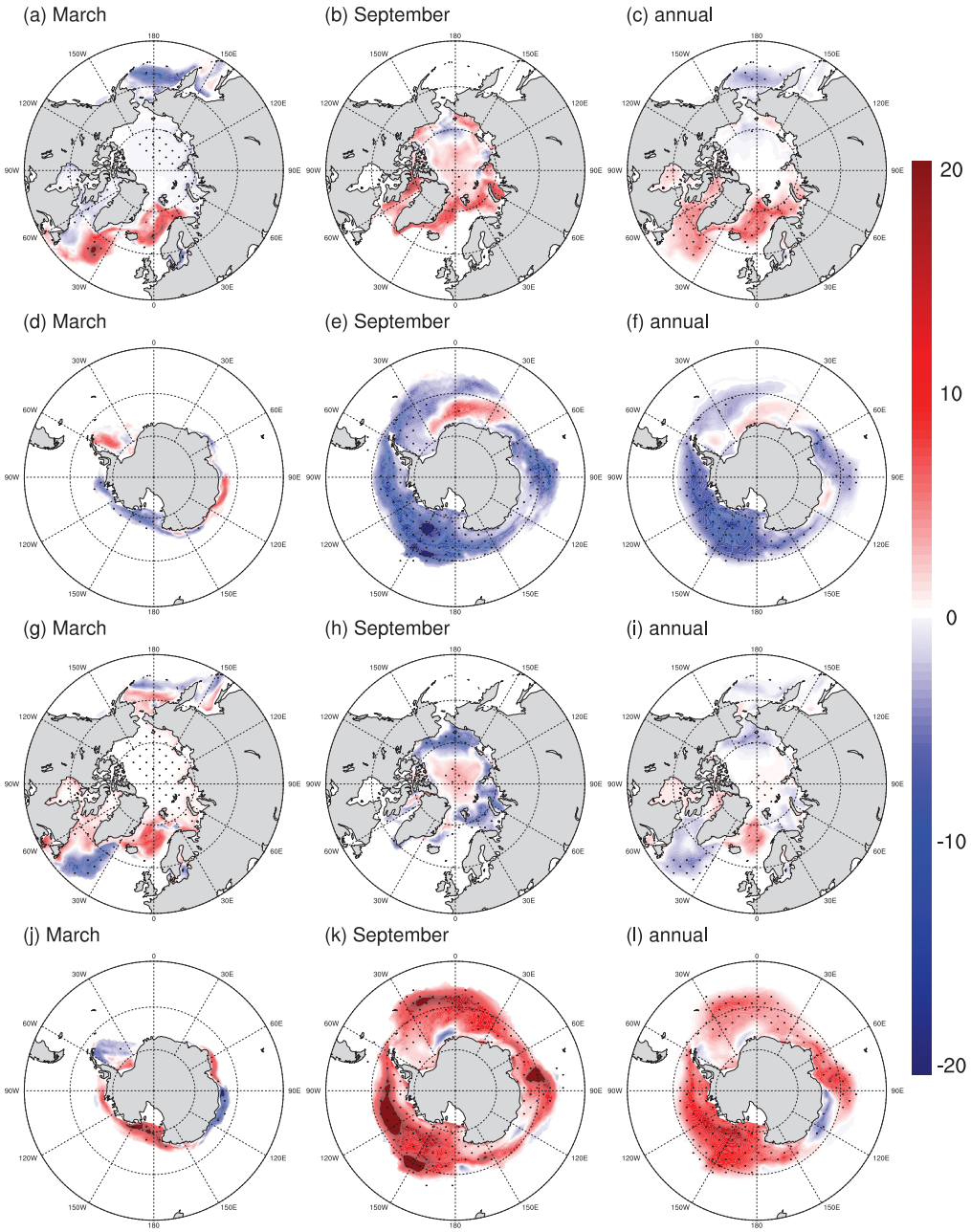

Fig. 5.5: *As in Fig. 5.4, but for sea ice concentration anomalies, units are %.*

Hemisphere yields a general enhanced production of sea ice (Fig. 5.4d-f), the difference amounts approximately to 0.3 m over coastal region of the Antarctic continent, and to less amount for the areas which are relatively far from the continental shelf. FE120 shows the opposite pattern (Fig. 5.4g-l), with general thinner sea ice over both polar regions. The maximum change happens over the Greenland Sea, at a maginitude of about -0.5 m.

Fig. 5.5 displays the changes of sea ice concentration. Over the central Arctic Ocean, we observe slight decrease and increase of FE80 sea ice concentration in March and September, respectively. This is reasonable, as the open-water ice growth mostly takes place in cold months, the reduced $\dot{A}_{ow}$ directly leads to decreased ice concentration and increased ice thickness in boreal winter. The resulting thicker sea ice persists longer on the sea surface during melting period, thereby reducing the areas of open water and leads in summer. Besides, a more pronounced feature is the increase in sea ice concentration in the Greenland-Iceland-Norwegian (GIN) Sea and North Atlantic subpolar gyre (Fig. 5.5a-c). The sea ice concentration decreases for most parts of the Southern Ocean during austral winter (September) which dominates its annual pattern. Whereas, both positive and negative anomalies of sea ice concentration are found along the Antarctic continental shelf in austral summer (March). For the experiment FE120, the anomalies pattern is generally reversed (Fig. 5.5g-l), except for the increased sea ice over Nordic Sea and central Arctic Ocean during winter and summer, respectively.

5.5 Changes in the sea surface temperature and salinity

Fig. 5.6a,b depicts the responses of the sea surface temperature (SST) and sea surface salinity (SSS) in FE80. Compared to FE-CTR, pronounced cooling is simulated over the GIN Sea and the North Atlantic in FE80 (Fig. 5.6a), with the most significant change (over $-1°C$) occurring at the North Atlantic subpolar gyre, while for the Southern Ocean it is the opposite case, with the strongest warming happening at the region of Antarctic Circumpolar Current (ACC) (about $0.5°C$). The simulated changes in the FE80 sea surface salinity show a more saline central Arctic (Fig. 5.6b), as a consequence of the brine release led by enhanced sea ice production. A more pronounced feature is

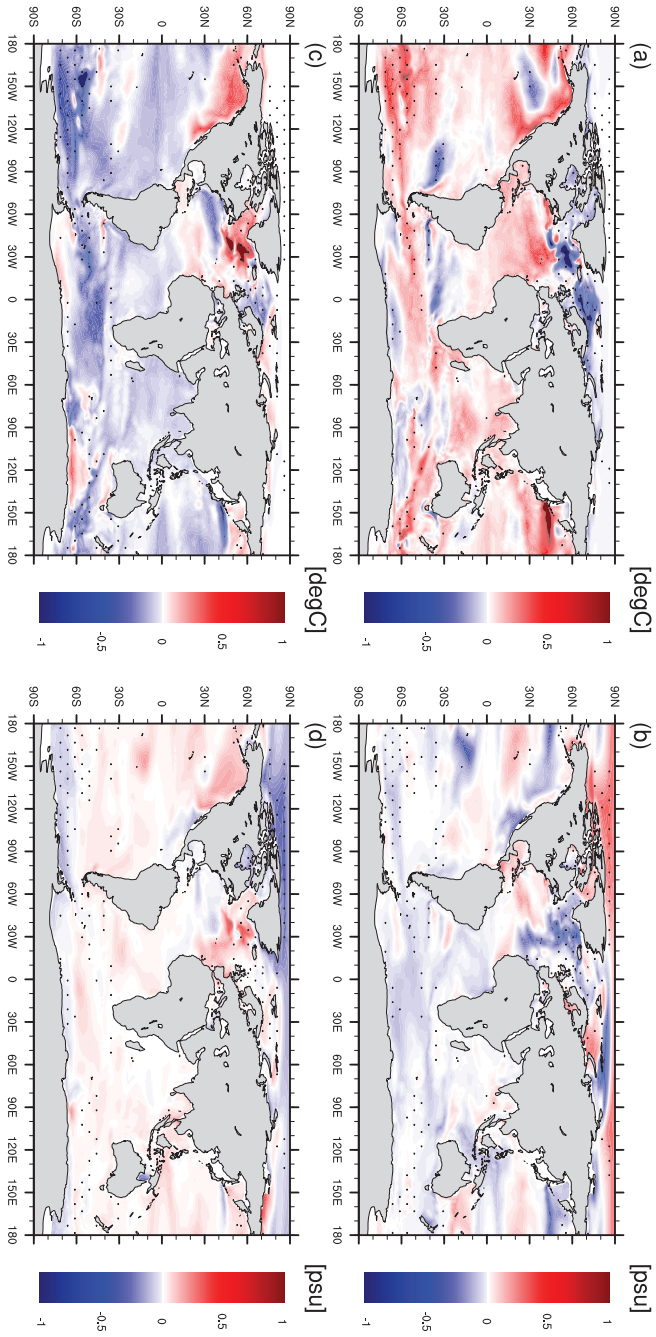

Fig. 5.6: *(a-b) Difference of annual mean (a) the sea surface temperature and (b) the sea surface salinity between experiments FE80 and FE-CTR (FE80 minus FE-CTR). Hatched regions have >95% significance level based on Student's T test, auto-correlation has been taken into account. (c-d) As in (a-b), but for anomalies between FE120 and FE-CTR.*

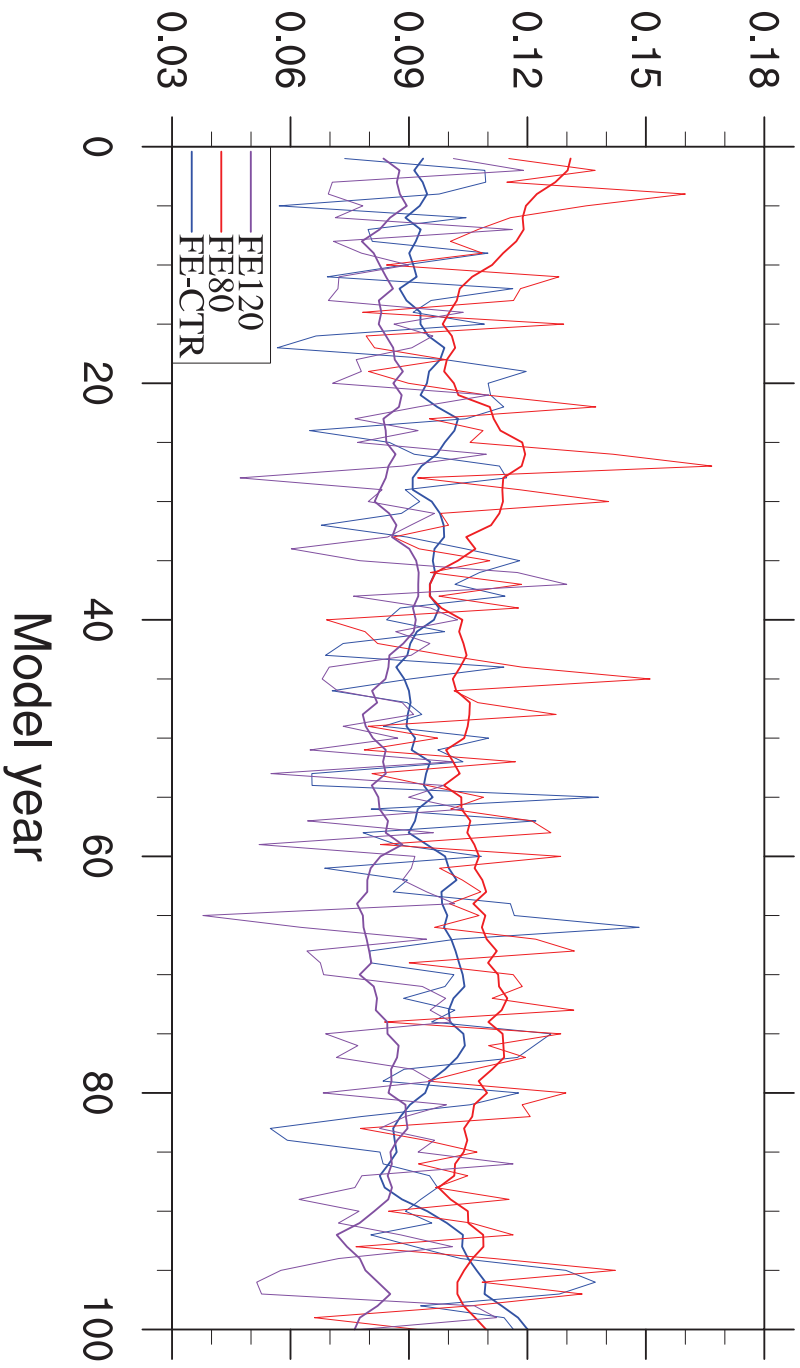

Fig. 5.7: *Time series of Fram Strait sea ice mass transport. A 11 years filter is applied (thick lines). Units are Sv.*

the freshening over the Nordic Sea and North Atlantic subpolar region. The response of SST and SSS to a larger c_* is illustrated in Fig. 5.6c,d. Significant warming and salinification are found over the North Atlantic Ocean, opposite to the results of FE80. The Southern Ocean experiences a cooling, mainly along the ACC route, at a magnitude of about $-0.5°C$. Reduced sea ice production results in a freshening Arctic Ocean in FE120.

An important factor affecting the SSS anomalies over North Atlantic subpolar region is a sea ice dynamic process: sea ice import through Fram Strait that affects the freshwater budget of the subpolar region. As depicted in Fig. 5.7, compared to our control experiment, a larger and smaller import of sea ice mass is simulated in FE80 and FE120, with the mean difference being approximately 0.01 Sv and -0.01 Sv, respectively, at a significance level (Student's T test) exceeding 99%.

To further investigate the impact of Arctic sea ice transport on the deep water formation, composite analyses are calculated as depicted in Fig. 5.8, by averaging the SSS anomaly fields that have more (less) than one standard deviation with respect to indices of the Fram Strait ice mass import. As a result of the high (low) Fram Strait ice mass import, pronounced freshening (salinification) happens over Nordic Sea and subpolar North Atlantic Ocean in particular the Labrador Sea, with a delay of 2 years. Nordic and Labrador Seas are the main deep water formation sites in FESOM-ECHAM6 [see *Danabasoglu et al.*, 2014, Fig. 13]. The resulting less (more) dense sea water leads to a weakened (stronger) downwelling current over the North Atlantic and a decline (strengthening) in AMOC circulation. FE80 and FE120 reveal similar composite patterns between SSS and Fram Strait ice mass import as in Fig. 5.8, therefore are not shown here.

5.6 Positive feedback behind the sea ice change in the Arctic

In boreal winter, new sea ice is formed on open water when the ocean loses heat to the atmosphere and the temperature of sea water is about to fall below its freezing point. When $c_* = 80\%$ is applied, sea ice grows more in the vertical direction as a result of reduced $\dot{A}_{ow}$, increasing the persistence of open water in boreal winter (Fig. 5.5a) and

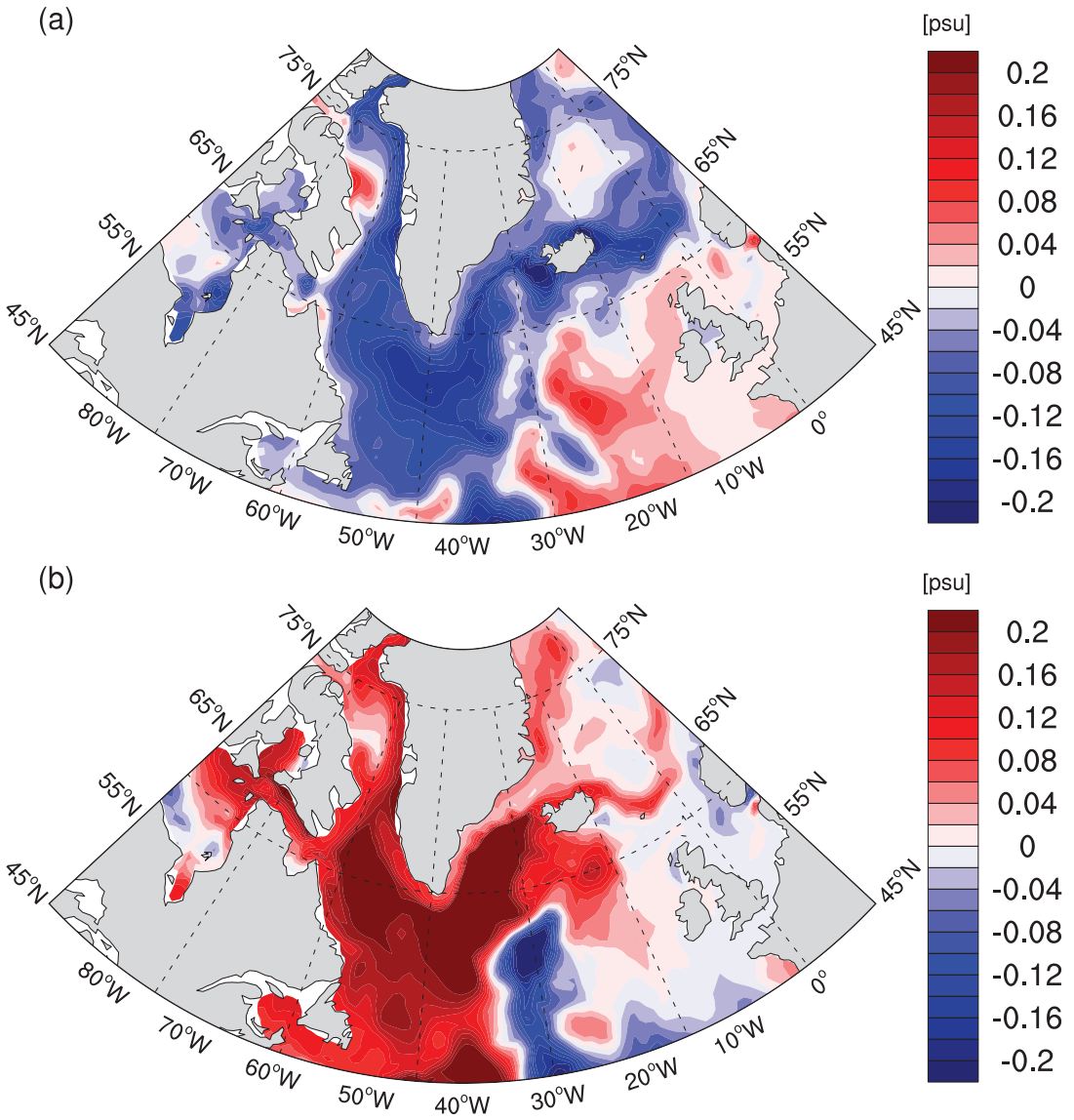

Fig. 5.8: *Composite map between sea surface salinity anomalies and (a) high and (b) low Fram Strait ice mass import with a lag of 2 years (ice import leads), based on FE-CTR. Units are psu. Composite map shown here is calculated by subtracting the slices that are above/below one standard deviation of the indices of Fram Strait ice mass import.*

the accompanying heat loss from ocean to air. More sea ice is therefore generated which in turn helps to increase the sea ice thickness as depicted in Fig. 5.4a-c. The increased sea ice in the Arctic strongly reinforces sea ice export into the subpolar regions through Fram Strait. Such process is clearly seen in the plot of ice mass transport as illustrated in Fig. 5.7. Therefore, the increased sea ice in GIN Sea, Labrador Sea and the Atlantic subpolar gyre is partly owing to the stronger Arctic sea ice transport. Whereas the opposite case is for the experiment with $c_* = 120\%$: less Arctic sea ice volume is simulated which leads to a reduction of Fram Strait sea ice import. Significant retreat of sea ice is observed over the Labrador Sea in March (Fig. 5.5g).

Fig. 5.9a, b represent the changes of zonal profiles of the FE80 ocean temperature and salinity. Compared to FE-CTR, there is a significant decrease in water temperature in FE80 for the upper ocean (0-100 m) between $50°N$ and $70°N$. At the same time, the sub-surface signal between 100-1000 m shows the opposite behavior, especially over tropical and sub-tropical regions. Fresher sea water is simulated in FE80 for the upper ocean (0-100 m) of $50-70°N$ latitude as shown in Fig. 5.9b. The decline of the AMOC (Fig. 5.9c) is owing to the negative salinity anomaly which weakens the sinking in the North Atlantic Ocean. Furthermore, there are two striking features in terms of the zonal ocean temperature and salinity anomalies (Fig. 5.9a-b): 1) the significant cooling and freshening of deep water (1000-3000 m) probably origins from the North Atlantic surface water; 2) increased temperature and salinity of bottom water (below 3000 m) is more likely caused by the stronger transport of Antarctic Bottom Water (AABW) cell (Fig. 5.9c), considering the warming in the surface of Southern Ocean (Fig. 5.6a). Further study is needed to determine the nature of this phenomenon.

FE120 illustrates opposite patterns (Fig. 5.9d-f). In detail, the North Atlantic upper ocean experiences a warming and salinification, the resulting denser sea water is the cause for a strengthening AMOC, which further changes the properties of deep water (1000-3000 m). Cooling and freshening of bottom water (below 3000 m) is associated with the weaker AABW cell and the cooling of Southern Ocean.

The spatial patterns of the surface air temperature (SAT) anomalies, associated with high (low) phases of AMOC are illustrated by composite maps (Fig. 5.10). During the high (low) phase of the AMOC, there is a general warming (cooling) of $0.5°C$ in the central Arctic Ocean. A more pronounced feature is the significant warming (cooling)

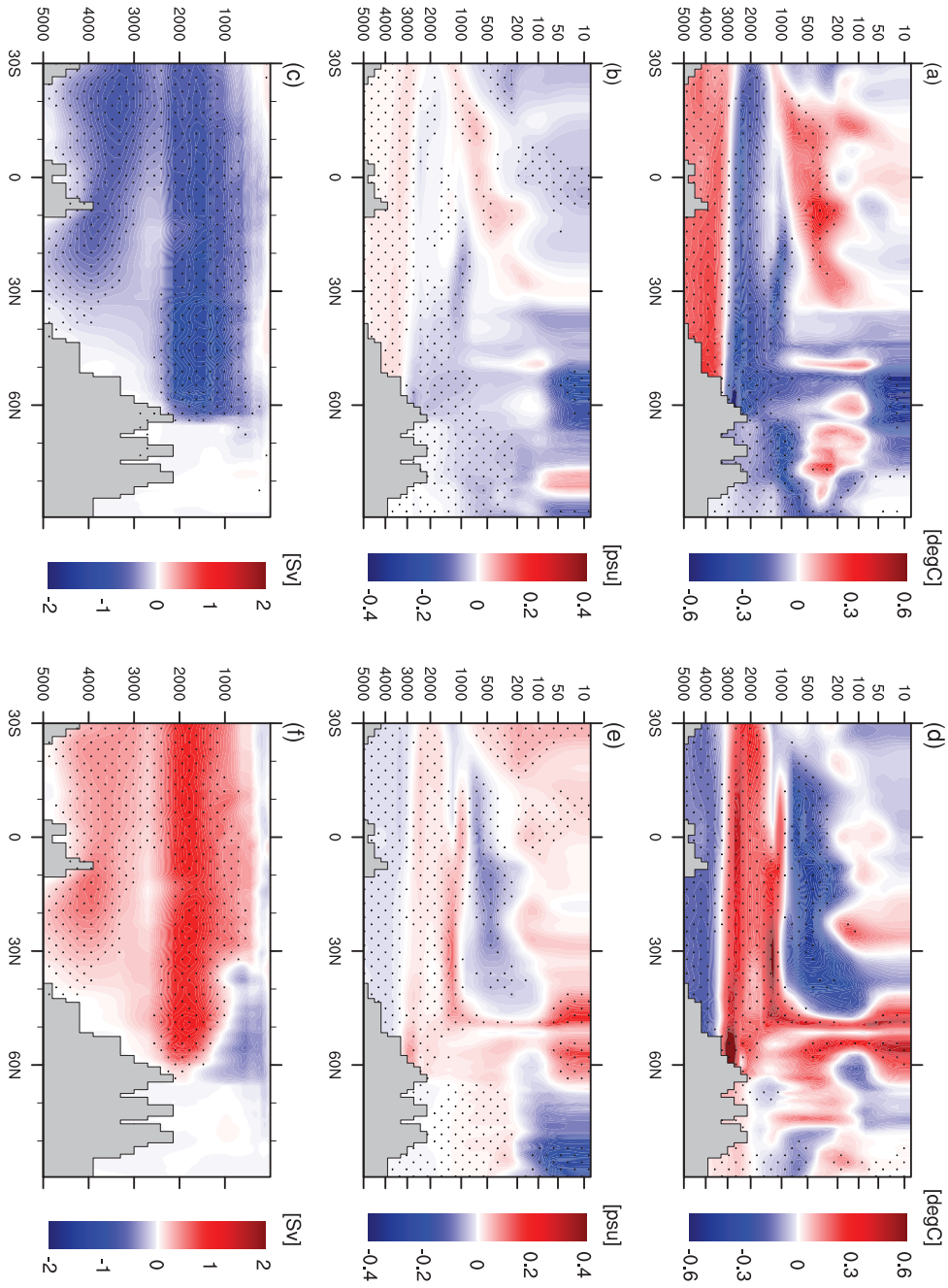

Fig. 5.9: *(a-c)Difference of (a) zonal mean ocean temperature, (b) zonal mean ocean salinity and (c) AMOC between experiments FE80 and FE-CTR (FE80 minus FE-CTR) for the Atlantic region. Hatched regions have >95% significance level based on Student's T test. (d-f) As in (a-c), but for anomalies between FE120 and FE-CTR.*

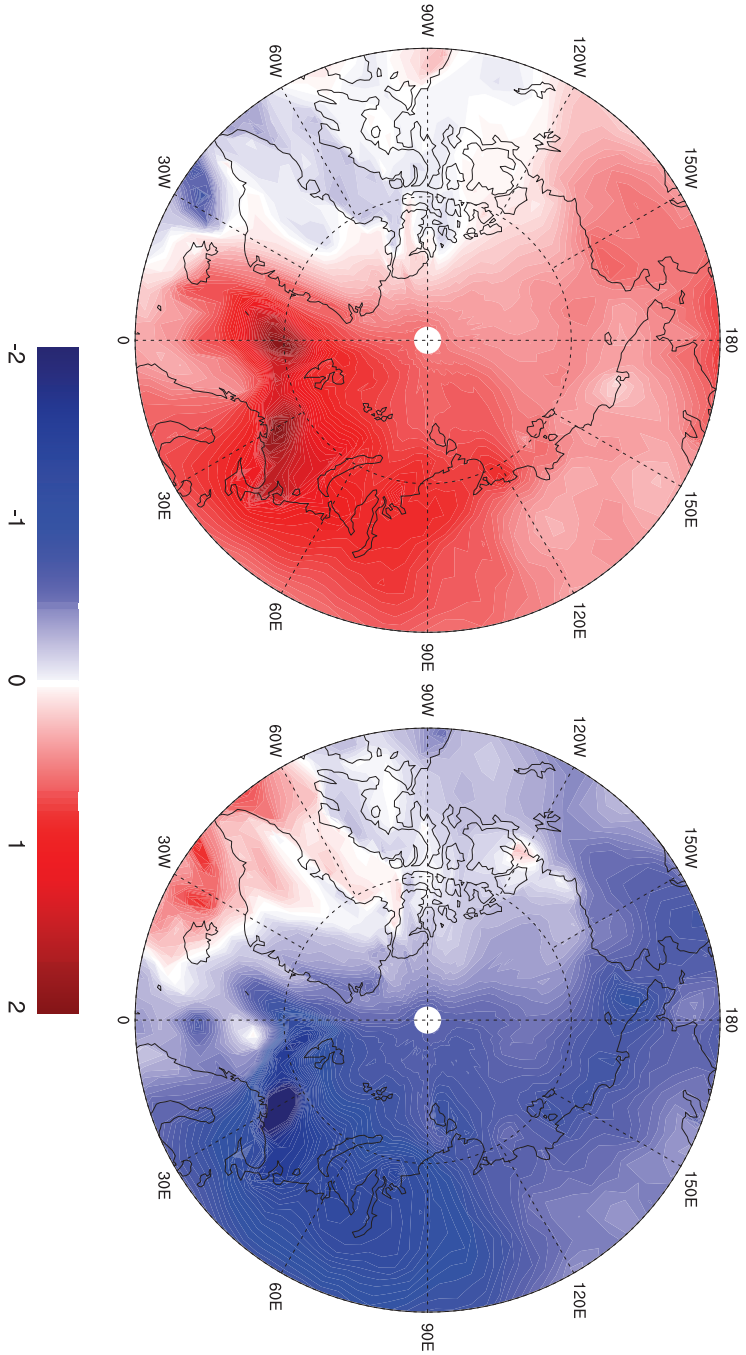

Fig. 5.10: *Composite map between surface air temperature anomalies and high (low) phases of AMOC. Units are °C. Composite map shown here is calculated by subtracting the fields that are above (below) one standard deviation of the AMOC indices.*

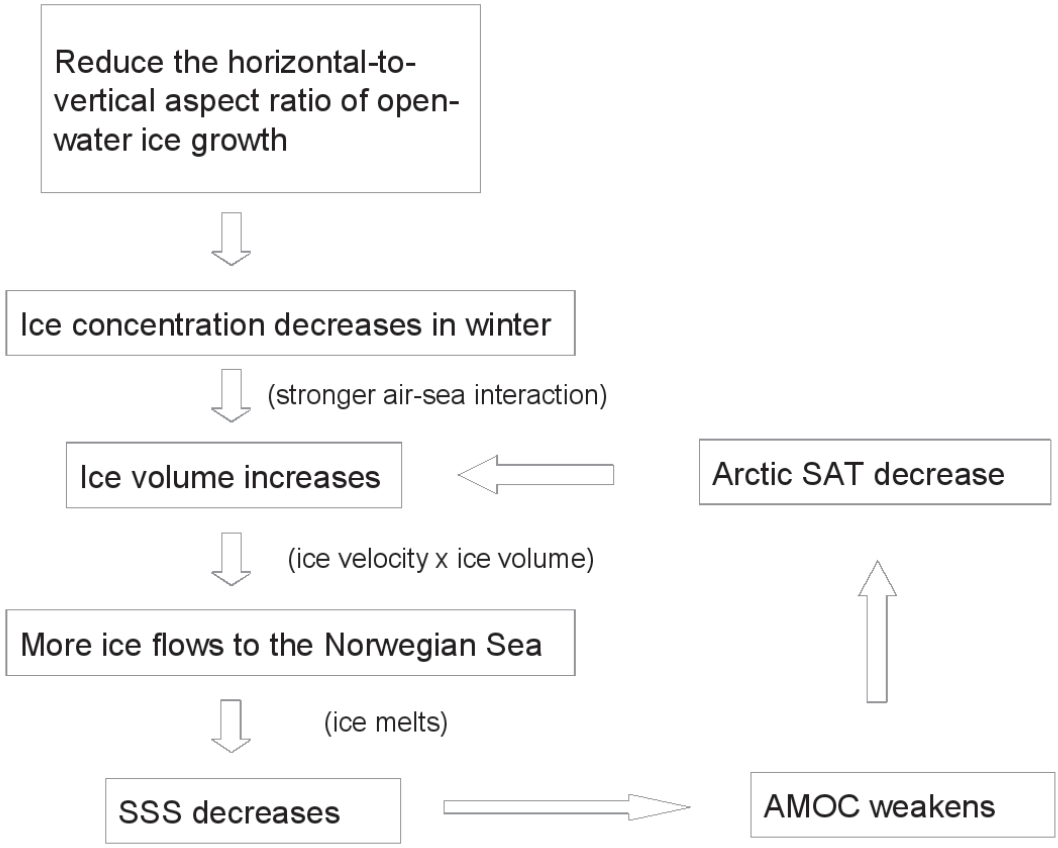

Fig. 5.11: *Positive feedback in the Northern Hemisphere between sea ice and large-scale ocean circulation when $\dot{A}_{ow}$ is reduced (FE80).*

over the Noridc Sea, which is linked to an enhanced (weakened) surface northward heat transport. Therefore, the increase (decrease) in AMOC leads to a general increase (decrease) in the Arctic SAT, such association is supported by numerous studies [e.g., *Schlesinger and Ramankutty*, 1994; *Rühlemann et al.*, 2004; *Knight et al.*, 2005; *Dima and Lohmann*, 2007; *Zhang*, 2007, 2008; *Chylek et al.*, 2009; *Mahajan et al.*, 2011; *Zhang*, 2015] .

Here we propose a positive feedback which to a certain extent affects the simulated Arctic sea ice and AMOC in our sensitivity experiments. For example in the case when $\dot{A}_{ow}$ is reduced (FE80), the Arctic grid-cell mean sea-ice thickness in increase (Fig. 5.4a-c) as a result of the stronger air-sea interaction in winter through larger open-water and leads. The increased sea-ice volume leads to an enhanced ice transport towards the subpolar regions through Fram Strait (Fig. 5.7), which influences the freshwater budget of GIN Sea and North Atlantic subpolar region (Fig. 5.8), and further weakens the Atlantic overturning circulation (Fig. 5.6c,f). As a result, the Arctic experiences a cooling (Fig. 5.10), allowing more sea ice formation, which in turn helps to increase the Fram Strait ice transport. In this way, a positive feedback is formed (Fig. 5.11).

5.7 Mechanism for the sea ice change in the Southern Ocean

Different from the Arctic sea ice, the sea ice in the Southern Ocean is more seasonal rather than multi-year, and therefore shows a more pronouced response to change of open-water ice growth parameterization. For example in the FE80 experiment, increased open-water and leads in austral winter (September) results in enhanced sea ice growth, which buffers the effect of the reduced $\dot{A}_{ow}$ on sea ice concentration. Thicker sea ice persists longer in austral summer, which is the reason why in some regions (e.g., the Weddell Sea) the sea ice concentration increases in March. In contrast to the cooling of the North Atlantic, most parts of the Southern Ocean experience an increase in SST with the most significant warming occurring along the route of the ACC (about $0.5°C$). Such pattern is likely caused by regional processes involving stronger vertical mixing and enhanced convective overturning, which tends to bring warm circumpolar sea water to the surface, as well as the interhemispheric bipolar seasaw linked to AMOC

weakening. The ACC warming can be seen in all seasons throughout the year.

5.8 Improvement of the FESOM-ECHAM6 performance on simulating sea ice and AMOC

As mentioned earlier, FESOM-ECHAM6 has shortcomings when simulating the subpolar sea-ice boundary in the Northern Hemisphere and the strength of AMOC: 1) Greenland Sea ice is much thicker than observational estimate [*Zhang and Rothrock*, 2005; *Fetterer et al.*, 2002], 2) There is extensive sea ice in the Labrador Sea during winter, 3) AMOC is relatively weaker than the estimates of global circulation from the hydrographic data [*Ganachaud and Wunsch*, 2000].

In our experiment FE120, we increase the horizontal open-water ice growth by 20%, therefore limiting the heat loss of the ocean in winter. The modeled sea ice and AMOC are found to be more close to observational estimates. In detail, thinner sea ice is simulated over the Arctic Ocean, and the ice thickness over Greenland Sea is significantly decreased mainly owing to the weakened air-sea interaction and the Transpolar Drift Stream. Retreat of ice extent over the Labrador Sea is found, linked to a decline in the Fram Strait ice export. Furthermore, a stronger AMOC is produced by FE120, caused by a salinification over the North Atlantic subpolar gyre.

Given above, we conclude that a factor of $c_* = 120\%$ can improve the behavior of FESOM-ECHAM6 on simulating sea ice and the strength of AMOC. Then a question arises as to can a larger c_* (e.g., 150%) improve the model performance even further. Therefore a logical next step would be to seek for the optimal value for c_*, which allows the simulated climate be more consistent with observations.

5.9 Discussion

a. The process of open-water ice growth

As reported by *Notz* [2012], focus of sea ice simulation has been primarily on changes in the ice volume that result from changes in the ice thickness. However, for a realistic representation of the impact of thermodynamics on sea-ice thickness distribution,

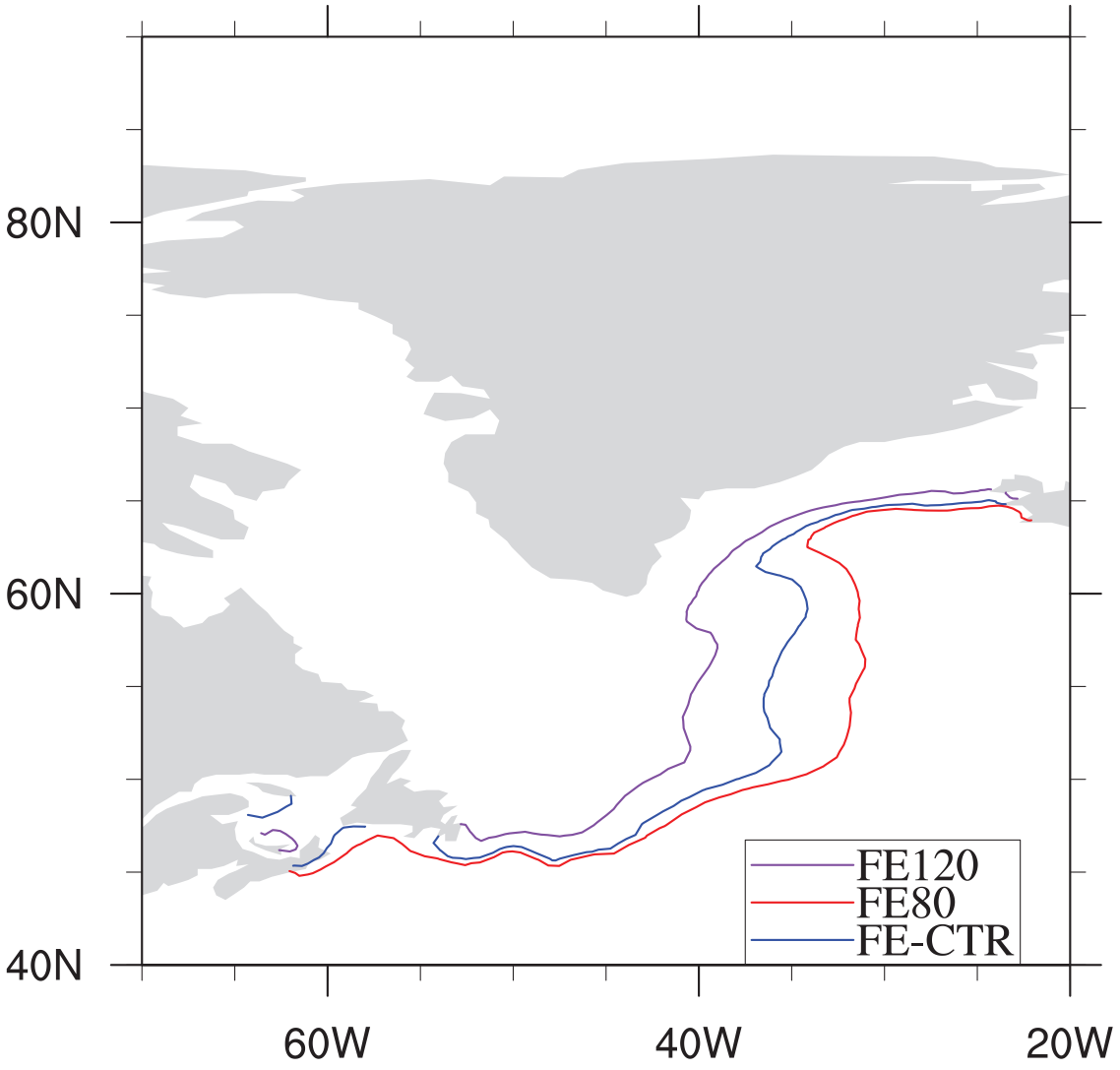

Fig. 5.12: *Sea ice extent over Labrador Sea (defined by 15% sea ice concentration) in the three experiments.*

its lateral versus vertical heat exchange — including the open water ice growth and lateral/vertical ice accretion — is also of importance on ice extent, in particular on simulations extending beyond a few days. Ice growth on open water is a key element of any sea-ice model [*Hibler*, 1979]. The new ice volume formed on open water is transferred into solid sea ice which limits the area of open water as well as heat exchange between the water and the air. A difficulty arises when distributing the new ice volume between growth in area and thickness [*Smedsrud*, 2011]. It should be noted that with the presence of a thin ice cover (normally below 20 cm) the ocean-atmosphere heat exchange still occurs [*Maykut*, 1986].

Unfortunately, this process cannot be explicitly resolved in large-scale models and needs to be parameterised. *Biggs et al.* [2000] introduced a more physically based parameterisation of open water ice formation with the lead closing parameter h_0 being a nonlinear function of ice velocity, wind speed and packice thickness. *Vancoppenolle et al.* [2010] reported that the computed values of h_0 are well-suited for the simulation of new ice growth in the calm waters of the Arctic Ocean, as well as for leads and polynyas.

In sea ice models, the volume of new ice can be computed from the open water energy budget, then difficulties and uncertainties arise when transforming the certain volume of new ice into growth in thickness and concentration in that grid cell. It is not known how the new ice shall be distributed in reality. Our purpose is to investigate to what extent such parameter can affect the simulation results. We do observe significant changes of sea ice, ocean and even the climate when changing this parameter, and the changes to sea ice and AMOC are mostly significant and robust based on Student's T test.

New ice formation strongly depends on many uncertain parameters, such as wind speed [*Alam and Curry*, 1998; *Winsor and Björk*, 2000; *Smedsrud and Skogseth*, 2006], ocean currents [*Kämpf and Backhaus*, 1999], ice velocity and packice thickness, and is based on a theoretical polynya model [*Biggs et al.*, 2000], which was validated with laboratory work [*Martin and Kaufmann*, 1981]. One could describe the factor c_* as a function of these elements. The newly formed sea ice then in turn affects these sea state variables, which can further cause discrepancies in some regional parts. Therefore, one can expect that the anomalies of ice, ocean and surface properties observed in our work,

are owing to the combined effects of all the processes mentioned above. Even though seeking for the optimal values of c_* is beyond the scope of this study, we can empirically determine a factor c_* to reduce the discrepancy between observed and modeled sea ice evolution. FESOM-ECHAM6 tends to overestimate the sea ice volume over the GIN Sea and subpolar North Atlantic [*Sidorenko et al.*, 2014], we expect that such problem can be solved by applying a larger horizontal-to-vertical aspect ratio of open-water ice growth ($c_* > 100\%$) over the Northern Hemisphere.

b. Discussion on the effects of c_* on sea ice and ocean

The most significant response to the increased lead closing parameter happens at sea ice edge rather than the central Arctic. This is mainly due to two factors: one is that the ice in the central Arctic has almost full ice coverage, and the effect of c_* can only take place on open water. Another reason is that, as described in Eq. (1) and (2), when ice grows on open water, the increase in ice concentration is relatively larger for thinner ice, thus the factor c_* is more important for the ice boundary parts. Basically, the factor c_* only matters in autumn and winter when thermodynamic ice growth occurs. So the resulting reduction of ice concentration in SIM is an artifact dominated by the winter ice change. In our complex FESOM-ECHAM6, the summer ice concentration is also affected by other elements such as the ice dynamics, therefore the effect of c_* is overwhelmed.

The sea ice change in FESOM-ECHAM6 induced by our modification to the open water ice growth representation are in good agreement with former studies [e.g., *Bitz and Roe*, 2004; *Fichefet and Maqueda*, 1997; *Wang et al.*, 2010; *Mauritsen et al.*, 2012; *Notz et al.*, 2013] which revealed that the heat loss in open water during wintertime significantly enhances sea ice formation, therefore increasing the lead closing parameter h_0 causes there to be more open water and hence thicker ice. In detail, through sensitivity experiments with the LIM2 sea-ice model, *Fichefet and Maqueda* [1997] indicated that when the model was run without leads, the air-sea heat fluxes were substantially modified, resulting in drastically reduced sea-ice thickness and total ice volume. *Wang et al.* [2010] revealed that the increase in h_0 leads to decreased ice concentration during ice growth, and the annual mean sea ice volume, thickness and extent all increase with h_0, which is in good consistency with our results. In addition, *Bitz and Roe* [2004]

found a growth-thickness mechanism, which describes a negative feedback between the ice thickness and the adjustment of ice growth rate to external perturbations. More recently, *Mauritsen et al.* [2012]; *Notz et al.* [2013] test the sensitivity of the climate model MPI-ESM to vertical-lateral ice growth ratio (C_{freeze}). By increasing/decreasing C_{freeze}, more/less open ocean persists during freeze-up, thereby enhancing/weakening oceanic heat loss and sea ice formation. This is in good agreement with our work. Beyond previous studies mentioned above, our results also show the feedback among the sea ice, ocean and climate, which further gives us a more comprehensive view of the effect of open-water ice growth.

Regarding the relationship between the Arctic sea ice and AMOC (Fig. 5.11), a similar positive feedback has been also identified for hosing experiments in the North Atlantic Ocean [*Lohmann and Gerdes*, 1998], but without sea ice transport. In detail, more sea ice decreases the AMOC, which cools the high latitudes. *Koenigk et al.* [2009] found that the interannual variability of sea ice volume in the subpolar Arctic is mainly determined by variations in sea ice import from the Central Arctic. Therefore, freshwater budget over subpolar regions such as the North Atlantic subpolar gyre is dominated by Arctic sea ice export rather than the local therdynamic sea ice change. Here, we find that sea ice transport affects the freshwater budget in regions of deep water formation (Fig. 5.6b, Fig. 5.8 and Fig. 5.9b), and therefore affects the AMOC (Fig. 5.9c). As pointed out in several studies [e.g., *Rühlemann et al.*, 2004; *Knight et al.*, 2005; *Zhang*, 2007, 2008; *Chylek et al.*, 2009], the AMOC has been linked to the Northern Hemisphere sea surface temperature (SST) and mid-depth temperature. The opposite trends in mid-depth warming and cooling in the downward branch of the North Atlantic deep water (Fig. 5.9a) is consistent with projections and internal variability linked to the AMOC [*Lohmann et al.*, 2008].

c. Discussion on the treatment of ice evolution in FESOM

FESOM is a high-resolution ice-ocean model which has the advantage of providing a regional focus in an otherwise global setup [*Sidorenko et al.*, 2011]. In our work, FESOM applies even higher resolution in the high latitudes than the tropical and subtropical region. It is therefore suitable for investigating polar properties, particularly sea ice characteristics, and the related processes. However, a disadvantage of this

comprehensive climate model lies on its relatively simple treatment to sea ice processes, which might have the potential to influence the simulation results. In detail:

1) Partitioning of lateral versus vertical growth of sea ice is most realistically simulated in models that explicitly include a sub-scale distribution of ice thickness [*Hibler*, 1979; *Bitz et al.*, 2001]. In such models, lateral melting can roughly be represented by the disappearance of the thinnest sea-ice classes and the accompanying expansion of open water. *Bitz et al.* [2001] also found that the simulated ice properties are sensitive to number of ice categories. In detail, a one-ice-category model tends to simulate larger ice concentration and smaller ice thickness compared to multi-category sea ice models.

2) A more recent method introduced by *Lipscomb* [2001] — linear remapping of ice thickness distribution — apprears to be more accurate and less diffusive than the fixed thickness scheme [*Hibler*, 1980]. Such method is applied in the current state-of-the-art model CICE5 [*Hunke et al.*, 2010]. In CICE5, all the new ice formed on open water is added to the thinnest ice category, without changing the ice concentration. If the new ice thickness exceeds the maximum threshold of the thinnest category, then the model distributes excess ice volume over all categories, leaving ice area unchanged. Therefore, there is a big discrepancy between the representation of lateral ice evolution in FESOM-ECHAM6 and CICE5, the former is changing with open water ice growth, while the latter is influenced by other elements such as lateral heat flux [*Maykut and Perovich*, 1987; *Steele*, 1992].

3) FESOM-ECHAM6 applies the simple zero-layer approach [*Hibler*, 1979] with linear temperature gradients from the sea ice top to bottom. More recently, a multilayer sigma-coordinate thermodynamic method is presented by *Huwald et al.* [2005]. Furthermore, a brine pocket parameterization is introduced by *Bitz and Lipscomb* [1999]; *Huwald et al.* [2005], which account for the temperature and salinity dependence of the sea ice properties. Compared to FESOM-ECHAM6, the multilayer thermodynamic method and brine pocket parameterization will lead to different vertical sea ice temperature profiles and sea surface salinity values over sea-ice regions, which results in a discrepancy in the conductive heat flux within sea ice and the freezing point of sea water.

4) Another realistic approach of lateral versus vertical melting is based on the ratio of bottom area versus edge area of the ice pack. However, the relationship between the

ice floe size and many external factors, for example, ice age, ice thickness and weather condition [*Dumont et al.*, 2011] is not yet sufficiently very crudely implemented in sea ice models.

Compared to FESOM-ECHAM6, there are some more sophisticated parameterizations describing sea ice processes. However, the lead closing parameter h_0 in the advanced representations of sea ice evolution still needs to be determined empirically. A logical next step would be to investigate the sensitivity of the simulated climate to the lead closing parameter in climate models with the above mentioned new approaches.

d. Discussion on the effects of c_* on the climate

Besides ice and ocean properties, c_* can also have influences on the climate, as a pronounced warming over Eurasia and North America is observed in our sensitivity experiment, which results from a strengthening AO-like pattern. There are studies presenting the response of temperature to changes in SLP, which resemble our findings. For example, *Hurrell* [1995] has shown that negative SLP anomalies over Iceland and enhanced westerly flow are associated with positive temperature change extending from Great Britain and Scandinavia far into Siberia. *Kodera and Yamazaki* [1994]; *Graf et al.* [1995]; *Kodera and Koide* [1997] suggested a possibility of a dynamical linkage between the wintertime warming over Eurasia and enhanced polar night jet linked to AO+. Experiments with an atmospheric GCM (GFDL AM2) are used to determine the effect of the 1990s thinning of Arctic sea ice [*Gerdes*, 2006], the atmospheric response comprises a reduction in SLP in the central Arctic and over the Nordic Seas, and high pressure anomalies over the subtropical North Atlantic and the subpolar North Pacific.

There are a number of studies aiming to investigate the responses of climate to changes of the Arctic sea ice. For example, *Magnusdottir et al.* [2004] used an atmosphere general circulation model CCM3 to investigate the impact of sea ice change on the atmosphere and found significant changes in the North Atlantic storm track. *Chiang and Bitz* [2005] found that imposed ice can induce a rapid cooling and drying of the air and surface over the entire mid- and high latitudes, simulated by the Community Climate Model version 3 coupled to a 50-m slab ocean. More recently, *Semmler et al.* [2012] who forced the model EC-EARTH-IFS with reduced ice cover found negative sea level pressure anomalies over the western Arctic and positive anomalies over Siberia,

affecting surface temperatures over Europe. *Liu et al.* [2012] found that the declining autumn Arctic sea ice is linked to to the negative phase of the winter Arctic oscillation, resulting in increased cold surges over large parts of northern continents. Our work are different from former studies from the following aspects:

1) Unlike other studies mentioned above, our sensitivity experiment aims at changing the horizontal-to-vertical growth ratio of newborn ice on open water as shown in Fig. 1, and is not for simulating the climate changes. This study is motivated by the uncertainties in the parameterizations distributing the new ice volume between growth in area and thickness, which is due to our lack of fundamental understanding and a proper representation of processes in coupled simulations.

2) In our work, the changes of sea ice thickness and sea ice concentration are not identical, as sea ice becomes much thicker, but ice concentration significantly decrease over much part of the polar regions especially in winter. While, sea ice change in former studies indicate similar pattern for thickness and concentration, and the response of climate is due to the combined effect of the two elements.

3) Our simulations indicate a positive feedback between the Arctic sea ice, the surface temperature and the strength of AMOC, which was not studied before.

5.10 Conclusions

In the present section, we conduct three model simulations with FESOM-ECHAM6 in order to investigate the effects of the horizontal-to-vertical aspect ratio of open-water ice growth on sea ice, ocean and the climate. Compared to the reference experiment, a sensitivity experiment with the same sea ice volume but more open water shows a significant increase in ice thickness for the whole Arctic and some parts of the Southern Ocean. In the Arctic Ocean, a positive feedback among sea ice, AMOC and sea surface temperature is simulated: increase in sea ice thickness (i.e., ice volume) leads to more ice transport towards the GIN Sea. In spring and summer, ice melts and freshens the sea water at the GIN Sea and the North Atlantic subpolar gyre, thus weakening the AMOC. As a result, the associated surface air temperature in the Arctic decreases, allowing more sea ice formation, which in turn helps to reinforce the ice transport and freshen the North Atlantic Ocean. Furthermore, another sensitivity experiment

with reduced open water reveals the opposite patterns, and is in better agreement with observational estimates.

The results presented in this study emphasize the importance of open-water ice growth. In detail, the distributing of new ice volume between growth in area and thickness can affect the ice properties, the ocean circulation and even the climate system in our climate model FESOM-ECHAM6. Another approach is a stochastic method [*Juricke and Jung*, 2014] to parameterize the open-water ice growth. Further analysis of the sea ice processes is necessary in order to test the robustness of climate change scenarios, especially at high latitudes where sea ice plays a dominant role.

In addition, a changed parameter in sea ice growth as done here could also affect the response of the system to past and future climate change scenarios, which is subject of a forthcoming study. Furthermore, this paper could be helpful for paleo-research and future climate projection. It is possible that in reality the factor c_* is climate dependent, and could be different under different climate conditions and climate sensitivity.

6 Conclusions and future perspectives

This PhD project targets to examine the simulated climate responses mid- and early-Holocene boundary conditions and to investigate how the area-thickness distribution of new ice formed in open water affects the ice and ocean properties by employing the newly developed global finite-element model ECHAM6-FESOM with unstructured mesh and high resolution. The key findings of this thesis can be summarized as follows:

- The model ECHAM6-FESOM simulates an enhanced mid-Holocene AMOC, accompanied by an increase in the ocean salinity over regions of deep water formation compared to pre-industrial, as: 1) a more positive phase of North Atlantic Oscillation (NAO) increased water density over the Labrador Sea through anomalous net evaporation and surface heat loss; 2) a decreased import of sea ice from the Arctic causes a freshwater reduction in the northern North Atlantic Ocean.
  Using the coupled model ECHAM6-MPIOM in T63GR15 and T31GR30 grids, we find that the simulated AMOC is strongly affected by the model resolution. In detail, stronger-than-present mid-Holocene AMOC is revealed by simulations with the T63GR15 grid, which resembles the result of ECHAM6-FESOM, while a decline of the mid-Holocene AMOC is simulated by the low resulution model with the T31GR30 grid.
  Such discrepancy can be attributed to different changes in Labrador Sea density which is mainly affected by 1) NAO-induced net precipitation, 2) freshwater transport from the Arctic Ocean, and 3) the strength of AMOC itself.
  We analyzed available coupled climate models showing a diversity of responses of

AMOC to mid-Holocene forcings, most of which reveal positive AMOC changes related to northern high latitudes salinification.
Other CMIP5 models, although have approximately similar resolutions, show very different response of the AMOC to 6k boundary conditions. However, exploring the nature of such association in every specific CMIP5 model is beyond the scope of this study. A logical next step would be the comparison of CMIP5 model scenarios with different resolution to identify the resolution-dependent mechanisms for the Holocene AMOC change, and to identify which resolution is the key influencing factor—the atmospheric resolution, the oceanic resolution, or both.

- Under the early-Holocene orbit and GHGs, the ECHAM6-FESOM simulation shows a JJA warming and DJF cooling over mid and high latitudes compared to pre-industrial, with amplification over the continents; as well as a reduction of sea ice in the Arctic and Southern Oceans. A reduced sea ice transport through the Fram Strait leads to a stronger-than-present Atlantic Meridional Overturning Circulation (AMOC) in the early-Holocene.
  Including the early-Holocene topography and continental ice sheet over North America leads to an additional regional cooling year-round. The resulted enhanced sea ice thermodynamic production over Baffin Bay and North Atlantic subpolar gyre is the cause for a more saline surface over the region of deep water formation.
  There are big discrepancies in the oceanic responses to different locations of freshwater discharge. LIS coastal melting only leads to a freshening over the Gulf Stream and Canary Current, with no meltwater advection to the deep water formation sites, therefore not affecting the strength of the thermohaline circulation. In contrast, adding freshwater into the Labrador Sea produces a significant decrease in ocean salinity over the North Atlantic region from sea surface to 200 m depth, contributing to a decline of the Atlantic meridional overturning circulation (AMOC).
  All early-Holocene experiments reveal a change of the westerlies over the North Atlantic section, accompanied by a more positive North Atlantic Oscillation (NAO) phase, which is led by the conresponding divergence anomalies of the Eliassen-Palm (E-P) flux. The enhanced westerly wind at 50 °N provides a barrier which

prevents the Arctic cold air from invading into the lower latitudes. This circulation change in the atmosphere leads to less frenquent episodes of blocking patterns which further resluts in decreased cold surges over most parts of the Northern Hemisphere continents, in particular the Europe and Asia in the early-Holcene compared to pre-industrial. Finally, the reduced cold air outbreak events, together with a relatively dry atmosperic condition, are the causes for a reduced snowfall over Europe and Asia.

- Two sensitivity experiments are performed which modify the horizontal-to-vertical aspect ratio of open-water ice growth. The resulting changes in the Arctic sea-ice concentration strongly affect the surface albedo, the ocean heat release to the atmosphere, and the sea-ice production.
  Anomalies in sea-ice transport lead to changes in sea surface properties of the North Atlantic and the strength of AMOC. For the Southern Ocean, the most pronounced change is a warming along the Antarctic Circumpolar Current (ACC), especially for the Pacific sector.
  ECHAM6-FESOM has relatively high ability for producing many aspects of the observed climate, but also has shortcomings when simulating the subpolar sea-ice boundary in the Northern Hemisphere and the strength of AMOC. We find that such disadvantages can be improved by tunning the process of open-water ice growth, which strongly influences the sea ice concentration in the marginal ice zone and affects the North Atlantic circulation through regulating the import of Arctic sea ice volume.
  The results presented in this study emphasize the importance of open-water ice growth. In detail, the distributing of new ice volume between growth in area and thickness can affect the ice properties, the ocean circulation and even the climate system in our climate model FESOM-ECHAM6. Another approach is a stochastic method [*Juricke and Jung*, 2014] to parameterize the open-water ice growth. Further analysis of the sea ice processes is necessary in order to test the robustness of climate change scenarios, especially at high latitudes where sea ice plays a dominant role.

Bibliography

Aagaard, K., and E. C. Carmack, The role of sea ice and other fresh water in the arctic circulation, *Journal of Geophysical Research: Oceans*, *94*(C10), 14,485–14,498, 1989.

Alam, A., and J. Curry, Evolution of new ice and turbulent fluxes over freezing winter leads, *J. Geophys. Res.*, *103*(C8), 15,783–15,802, 1998.

Bao, Q., et al., The flexible global ocean-atmosphere-land system model, spectral version 2: FGOALS-s2, *Adv. Atmos. Sci.*, *30*, 561–576, 2013.

Berger, A., Long-term variations of daily insolation and quaternary climatic changes, *J. Atmos. Sci.*, *35*(12), 2362–2367, 1978.

Bigelow, N. H., et al., Climate change and arctic ecosystems: 1. vegetation changes north of 55n between the last glacial maximum, mid-holocene, and present, *J. Geophys. Res.*, *108*(D19), 2003.

Biggs, N., M. M. Maqueda, and A. Willmott, Polynya flux model solutions incorporating a parameterization for the collection thickness of consolidated new ice, *J. Geophys. Res.*, *408*, 179–204, 2000.

Bitz, C., and G. Roe, A mechanism for the high rate of sea ice thinning in the arctic ocean, *Journal of Climate*, *17*(18), 3623–3632, 2004.

Bitz, C., M. Holland, A. Weaver, and M. Eby, Simulating the ice-thickness distribution in a coupled climate model, *J. Geophys. Res.*, *106*(C2), 2441–2463, 2001.

Bitz, C. M., and W. H. Lipscomb, An energy-conserving thermodynamic model of sea ice, *Journal of Geophysical Research: Oceans (1978–2012)*, *104*(C7), 15,669–15,677, 1999.

Boville, B. A., Sensitivity of simulated climate to model resolution, *J. Clim.*, *4*(5), 469–485, 1991.

Braconnot, P., et al., Results of pmip2 coupled simulations of the mid-holocene and last glacial maximum–part 1: experiments and large-scale features, *Clim. Past*, *3*(2), 261–277, 2007.

Bradley, R. S., Holocene paleoclimatology of the queen elizabeth islands, canadian high arctic, *Quaternary Science Reviews*, *9*(4), 365–384, 1990.

Brook, E. J., S. Harder, J. Severinghaus, E. J. Steig, and C. M. Sucher, On the origin and timing of rapid changes in atmospheric methane during the last glacial period, 2000.

Buizza, R., T. Petroliagis, T. Palmer, J. Barkmeijer, M. Hamrud, A. Hollingsworth, A. Simmons, and N. Wedi, Impact of model resolution and ensemble size on the performance of an ensemble prediction system, *Quart. J. Roy. Meteor. Soc.*, *124*(550), 1935–1960, 1998.

Burke, A., O. Marchal, L. I. Bradtmiller, J. F. McManus, and R. François, Application of an inverse method to interpret 231pa/230th observations from marine sediments, *Paleoceanography*, *26*(1), 2011.

Came, R. E., D. W. Oppo, and J. F. McManus, Amplitude and timing of temperature and salinity variability in the subpolar north atlantic over the past 10 ky, *Geology*, *35*(4), 315–318, 2007.

Carlson, A. E., A. N. LeGrande, D. W. Oppo, R. E. Came, G. A. Schmidt, F. S. Anslow, J. M. Licciardi, and E. A. Obbink, Rapid early holocene deglaciation of the laurentide ice sheet, *Nature Geoscience*, *1*(9), 620–624, 2008.

Chiang, J., and C. Bitz, Influence of high latitude ice cover on the marine intertropical convergence zone, *Clim. Dyn.*, *25*, 477–496, 2005.

Chylek, P., C. Folland, G. Lesins, M. Dubey, and M. Wang, Arctic air temperature change amplification and the atlantic multidecadal oscillation, *Geophys. Res. Lett.*, *36*(L14801), doi:10.1029/2009GL038777, 2009.

Collier, M., et al., The CSIRO-Mk3. 6.0 Atmosphere-Ocean GCM: participation in CMIP5 and data publication, in *International Congress on Modelling and Simulation–MODSIM*, 2011.

Crucifix, M., M.-F. Loutre, P. Tulkens, T. Fichefet, and A. Berger, Climate evolution during the holocene: a study with an earth system model of intermediate complexity, *Climate Dynamics*, *19*(1), 43–60, 2002.

Crucifix, M., P. Braconnot, S. Harrison, and B. Otto-Bliesner, Second phase of paleoclimate modelling intercomparison project, *Eos, Trans. Amer. Geophys. Union*, *86*(28), 264–264, 2005.

Curry, R. G., M. S. McCartney, and T. M. Joyce, Oceanic transport of subpolar climate signals to mid-depth subtropical waters, *Nature*, *391*(6667), 575–577, 1998.

Danabasoglu, G., et al., North atlantic simulations in coordinated ocean-ice reference experiments phase ii (core-ii). part i: mean states, *Ocean Modelling*, *73*, 76–107, 2014.

Danilov, S., G. Kivman, and J. Schröter, A finite element ocean model: principles and evaluation, *Ocean Model.*, *6*, 125–150, 2004.

Davis, B., S. Brewer, A. Stevenson, and J. Guiot, The temperature of europe during the holocene reconstructed from pollen data, *Quat. Sci. Rev*, *22*(15), 1701–1716, 2003.

de Vernal, A., and C. Hillaire-Marcel, Provincialism in trends and high frequency changes in the northwest north atlantic during the holocene, *Global Planetary Change*, *54*(3), 263–290, 2006.

Delworth, T. L., S. Manabe, and R. J. Stouffer, Multidecadal climate variability in the greenland sea and surrounding regions: a coupled model simulation, *Geophys. Res. Lett.*, *24*(3), 257–260, 1997.

Deser, C., R. Tomas, M. Alexander, and D. Lawrence, The seasonal atmospheric response to projected arctic sea ice loss in the late twenty-first century, *J. Climate*, *23*, 333–351, doi:10.1175/2009JCLI3053.1, 2010.

Dickson, B., From the labrador sea to global change, *Nature*, *386*, 649–650, 1997.

Dickson, R., T. Osborn, J. Hurrell, J. Meincke, J. Blindheim, B. Adlandsvik, T. Vinje, G. Alekseev, and W. Maslowski, The arctic ocean response to the north atlantic oscillation, *J. Clim.*, *13*(15), 2671–2696, 2000.

Dima, M., and G. Lohmann, A hemispheric mechanism for the atlantic multidecadal oscillation, *J. Clim.*, *20*(11), 2706–2719, 2007.

Dorn, W., K. Dethloff, and A. Rinke, Improved simulation of feedbacks between atmosphere and sea ice over the arctic ocean in a coupled regional climate model, *Ocean Model.*, *29*, 103–114, 2009.

Dumont, D., A. Kohout, and L. Bertino, A wave-based model for the marginal ice zone including a floe breaking parameterization, *Journal of Geophysical Research: Oceans (1978–2012)*, *116*(C4), 2011.

Eden, C., and J. Willebrand, Mechanism of interannual to decadal variability of the north atlantic circulation, *Journal of Climate*, *14*(10), 2266–2280, 2001.

Edmon Jr, H., B. Hoskins, and M. McIntyre, Eliassen-palm cross sections for the troposphere, *Journal of the Atmospheric Sciences*, *37*(12), 2600–2616, 1980.

Eliassen, A., and E. Palm, On the transfer of energy in stationary mountain waves, *Geofysiske Publikasjoner*, *22*, 1–23, 1961.

Feldstein, S. B., The dynamics of nao teleconnection pattern growth and decay, *Quarterly Journal of the Royal Meteorological Society*, *129*(589), 901–924, 2003.

Fetterer, F., K. Knowles, W. Meier, and M. Savoie, Sea ice index. boulder, co: National snow and ice data center, *Digital media*, *6*, 2002.

Fichefet, T., and M. Maqueda, Sensitivity of a global sea ice model to the treatment of ice thermodynamics and dynamics, *Journal of Geophysical Research: Oceans (1978–2012)*, *102*(C6), 12,609–12,646, 1997.

Fischer, N., and J. Jungclaus, Effects of orbital forcing on atmosphere and ocean heat transports in holocene and eemian climate simulations with a comprehensive earth system model, *Clim. Past*, *6*(25), 155–168, 2010.

Ganachaud, A., and C. Wunsch, Improved estimates of global ocean circulation, heat transport and mixing from hydrographic data, *Nature*, *408*(6811), 453–457, 2000.

Ganopolski, A., C. Kubatzki, M. Claussen, V. Brovkin, and V. Petoukhov, The influence of vegetation-atmosphere-ocean interaction on climate during the mid-holocene, *Science*, *280*(5371), 1916–1919, 1998.

Gent, P. R., et al., The community climate system model version 4, *J. Clim.*, *24*(19), 4973–4991, 2011.

Gerdes, R., Atmospheric response to changes in arctic sea ice thickness, *Geophys. Res. Lett.*, *33*(18), doi:10.1029/2006GL027146, 2006.

Getzlaff, J., C. W. Böning, C. Eden, and A. Biastoch, Signal propagation related to the north atlantic overturning, *Geophysical research letters*, *32*(9), 2005.

Gherardi, J.-M., L. Labeyrie, S. Nave, R. Francois, J. F. McManus, and E. Cortijo, Glacial-interglacial circulation changes inferred from 231pa/230th sedimentary record in the north atlantic region, *Paleoceanography*, *24*(2), 2009.

Goosse, H., and T. Fichefet, Importance of ice-ocean interactions for the global ocean circulation: A model study, *Journal of Geophysical Research: Oceans*, *104*(C10), 23,337–23,355, 1999.

Graf, H.-F., J. Perlwitz, I. Kirchner, and I. Schult, Recent northern winter climate trends, ozone changes and increased greenhouse gas forcing, *Contrib. Atmos. Phys.*, *68*(3), 233–248, 1995.

Häkkinen, S., Variability of the simulated meridional heat transport in the north atlantic for the period 1951–1993, *Journal of Geophysical Research: Oceans*, *104*(C5), 10,991–11,007, 1999.

Haug, G. H., K. A. Hughen, D. M. Sigman, L. C. Peterson, and U. Röhl, Southward migration of the intertropical convergence zone through the holocene, *Science*, *293*(5533), 1304–1308, 2001.

Herold, M., and G. Lohmann, Eemian tropical and subtropical african moisture transport: an isotope modelling study, *Climate dynamics*, *33*(7-8), 1075–1088, 2009.

Hibler, W., A dynamic thermodynamic sea ice model, *J. Phys. Oceanogr.*, *9*(7), 815–846, 1979.

Hibler, W., Modeling a variable thickness sea ice cover, *Monthly weather review*, *108*(12), 1943–1973, 1980.

Hoskins, B. J., I. N. James, and G. H. White, The shape, propagation and mean-flow interaction of large-scale weather systems, *Journal of the atmospheric sciences*, *40*(7), 1595–1612, 1983.

Houghton, R., Subsurface quasi-decadal fluctuations in the north atlantic, *Journal of Climate*, *9*(6), 1363–1373, 1996.

Hunke, E., and J. Dukowicz, An elastic-viscous-plastic model for sea ice dynamics, *J. Phys. Oceanogr.*, *27*, 1849–1868, 1997.

Hunke, E. C., W. H. Lipscomb, A. K. Turner, et al., Cice: the los alamos sea ice model documentation and software User's manual version 4.1 la-cc-06-012, *T-3 Fluid Dynamics Group, Los Alamos National Laboratory*, pp. 1–116, 2010.

Hurrell, J. W., Decadal trends in the north atlantic oscillation: regional temperatures and precipitation, *Science*, *269*(5224), 676–679, 1995.

Hurrell, J. W., Y. Kushnir, G. Ottersen, and M. Visbeck, *An overview of the North Atlantic oscillation*, Wiley Online Library, 2003.

Huwald, H., L.-B. Tremblay, and H. Blatter, A multilayer sigma-coordinate thermodynamic sea ice model: Validation against surface heat budget of the arctic ocean (sheba)/sea ice model intercomparison project part 2 (simip2) data, *Journal of Geophysical Research: Oceans (1978–2012)*, *110*(C5), 2005.

Huybers, P., G. Gebbie, and O. Marchal, Can paleoceanographic tracers constrain meridional circulation rates?, *Journal of physical oceanography*, *37*(2), 394–407, 2007.

Iacono, M. J., J. S. Delamere, E. J. Mlawer, M. W. Shephard, S. A. Clough, and W. D. Collins, Radiative forcing by long-lived greenhouse gases: Calculations with the aer radiative transfer models, *J. Geophys. Res.*, *113*(D13), 2008.

Indermühle, A., et al., Holocene carbon-cycle dynamics based on co2 trapped in ice at taylor dome, antarctica, *Nature*, *398*(6723), 121–126, 1999.

IPCC, Climate change 2013: the physical science basis. contribution of working group i to the fifth assessment report of the intergovernmental panel on climate change, 2013.

Jungclaus, J., N. Fischer, H. Haak, K. Lohmann, J. Marotzke, D. Matei, U. Mikolajewicz, D. Notz, and J. Storch, Characteristics of the ocean simulations in the Max Planck Institute Ocean Model (MPIOM) the ocean component of the MPI-Earth system model, *J. Adv. Model. Earth Syst.*, *5*(2), 422–446, 2013.

Jungclaus, J. H., H. Haak, M. Latif, and U. Mikolajewicz, Arctic-north atlantic interactions and multidecadal variability of the meridional overturning circulation, *J. Clim.*, *18*(19), 4013–4031, 2005.

Juricke, S., and T. Jung, Influence of stochastic sea ice parametrization on climate and the role of atmosphere–sea ice–ocean interaction, *Philosophical Transactions of the Royal Society A: Mathematical, Physical and Engineering Sciences*, *372*(2018), 20130,283, doi:10.1098/rsta.2013.0283, 2014.

Kämpf, J., and J. Backhaus, Ice-ocean interactions during shallow convection under conditions of steady winds: three-dimensional numerical studies, *Deep-Sea Res.*, *46*(6-7), 1335–1355, 1999.

Keigwin, L. D., and E. A. Boyle, Did north atlantic overturning halt 17,000 years ago?, *Paleoceanography*, *23*(1), 2008.

Klitgaard-Kristensen, D., H. P. Sejrup, H. Haflidason, S. Johnsen, and M. Spurk, A regional 8200 cal. yr bp cooling event in northwest europe, induced by final stages of the laurentide ice-sheet deglaciation?, *Journal of Quaternary Science*, *13*(2), 165–169, 1998.

Knight, J., R. Allan, C. Folland, M. Vellinga, and M. Mann, A signature of persistent natural thermohaline circulation cycles in observed climate, *Geophys. Res. Lett.*, *32*(L20708), doi:10.1029/2005GL024233, 2005.

Kodera, K., and H. Koide, Spatial and seasonal characteristics of recent decadal trends in the northern hemispheric troposphere and stratosphere, *J. Geophys. Res.*, *102*(D16), 19,433–19,447, 1997.

Kodera, K., and K. Yamazaki, A possible influence of recent polar stratospheric coolings on the troposphere in the northern hemisphere winter, *Geophys. Res. Lett.*, *21*(9), 809–812, 1994.

Koenigk, T., U. Mikolajewicz, J. H. Jungclaus, and A. Kroll, Sea ice in the barents sea: seasonal to interannual variability and climate feedbacks in a global coupled model, *Clim. Dyn.*, *32*(7-8), 1119–1138, 2009.

Koutavas, A., G. C. Olive, J. Lynch-Stieglitz, et al., Mid-holocene el niño–southern oscillation (enso) attenuation revealed by individual foraminifera in eastern tropical pacific sediments, *Geology*, *34*(12), 993–996, 2006.

Kutzbach, J., and R. Gallimore, Sensitivity of a coupled atmosphere/mixed layer ocean model to changes in orbital forcing at 9000 years bp, *Journal of Geophysical Research: Atmospheres (1984–2012)*, *93*(D1), 803–821, 1988.

Kutzbach, J., and Z. Liu, Response of the african monsoon to orbital forcing and ocean feedbacks in the middle holocene, *Science*, *278*(5337), 440–443, 1997.

Kutzbach, J., G. Bonan, J. Foley, and S. Harrison, Vegetation and soil feedbacks on the response of the african monsoon to orbital forcing in the early to middle holocene, 1996.

Kutzbach, J. E., Monsoon climate of the early holocene: climate experiment with the earth orbital parameters for 9000 years ago, *Science*, *214*(4516), 59–61, 1981.

Kwon, Y.-O., and C. Frankignoul, Mechanisms of multidecadal atlantic meridional overturning circulation variability diagnosed in depth versus density space, *Journal of Climate*, *27*(24), 9359–9376, 2014.

Lamy, F., H. W. Arz, G. C. Bond, A. Bahr, and J. Pätzold, Multicentennial-scale hydrological changes in the black sea and northern red sea during the holocene and the arctic/north atlantic oscillation, *Paleoceanography*, *21*(1), 2006.

Latif, M., and N. S. Keenlyside, A perspective on decadal climate variability and predictability, *Deep Sea Research Part II: Topical Studies in Oceanography*, *58*(17), 1880–1894, 2011.

Latif, M., C. Böning, J. Willebrand, A. Biastoch, J. Dengg, N. Keenlyside, U. Schweckendiek, and G. Madec, Is the thermohaline circulation changing?, *Journal of Climate*, *19*(18), 4631–4637, 2006.

Latif, M., et al., Reconstructing, monitoring, and predicting multidecadal-scale changes in the north atlantic thermohaline circulation with sea surface temperature, *Journal of Climate*, *17*(7), 1605–1614, 2004.

Leppäranta, M., A growth model for black ice, snow ice, and snow thickness in subarctic basins, *Nord. Hydrol.*, *14*, 59–70, 1983.

Li, L., et al., The flexible global ocean-atmosphere-land system model, Grid-point Version 2: FGOALS-g2, *Adv. Atmos. Sci.*, *30*, 543–560, 2013.

Lipscomb, W. H., Remapping the thickness distribution in sea ice models, *J. Geophys. Res.*, *106*(C7), 13,989–1400, 2001.

Liu, J., J. A. Curry, H. Wang, M. Song, and R. M. Horton, Impact of declining arctic sea ice on winter snowfall, *Proceedings of the National Academy of Sciences*, *109*(11), 4074–4079, 2012.

Liu, Z., J. Kutzbach, and L. Wu, Modeling climate shift of El Nino variability in the holocene, *Geophys. Res. Lett.*, *27*(15), 2265–2268, 2000.

Liu, Z., et al., The holocene temperature conundrum, *Proceedings of the National Academy of Sciences*, *111*(34), 3501–3505, 2014.

Lohmann, G., Atmospheric bridge on orbital time scales. theoretical and applied climatology, *Theoretical and Applied Climatology*, doi:10.1007/s00704-015-1725-2, 2016.

Lohmann, G., and R. Gerdes, Sea ice effects on the sensitivity of the thermohaline circulation*, *J. Clim.*, *11*(11), 2789–2803, 1998.

Lohmann, G., H. Haak, and J. H. Jungclaus, Estimating trends of atlantic meridional overturning circulation from long-term hydrographic data and model simulations, *Ocean Dyn.*, *58*(2), 127–138, 2008.

Lohmann, G., M. Pfeiffer, T. Laepple, G. Leduc, and J.-H. Kim, A model-data comparison of the holocene global sea surface temperature evolution, *Clim. Past*, (9), 1807–1839, 2013.

Lott, F., Alleviation of stationary biases in a GCM through a mountain drag parameterization scheme and a simple representation of mountain lift forces, *Mon. weather Rev.*, *127*(5), 788–801, 1999.

Loveland, T., B. Reed, J. Brown, D. Ohlen, Z. Zhu, L. Yang, and J. Merchant, Development of a global land cover characteristics database and igbp discover from 1 km avhrr data, *Int. J. Remote Sens.*, *21*(6-7), 1303–1330, 2000.

Magnusdottir, G., C. Deser, and R. Saravanan, The effects of north atlantic sst and sea ice anomalies on the winter circulation in ccm3. part i: Main features and storm track characteristics of the response, *J. Clim.*, *17*, 857–876, 2004.

Mahajan, S., R. Zhang, and T. L. Delworth, Impact of the atlantic meridional overturning circulation (amoc) on arctic surface air temperature and sea ice variability, *J. Clim.*, *24*(24), 6573–6581, 2011.

Marsland, S., H. Haak, J. Jungclaus, M. Latif, and F. RÃ¶ske, The Max-Planck-Institute global ocean/sea ice model with orthogonal curvilinear coordinates, *Ocean Model.*, *5*(2), 91–127, doi:10.1016/S1463-5003(02)00015-X, 2003.

Martin, S., and P. Kaufmann, A field and laboratory study of wave damping by grease ice, *J. Glaciol.*, *27*(96), 283–313, 1981.

Mauritsen, T., et al., Tuning the climate of a global model, *Journal of Advances in Modeling Earth Systems*, *4*(3), doi:10.1029/2012MS000154, 2012.

Maykut, G. A., *The surface heat and mass balance*, Springer, 1986.

Maykut, G. A., and D. Perovich, The role of shortwave radiation in the summer decay of a sea ice cover, *J. Geophys. Res.*, *92*(C7), 7032–7044, 1987.

McManus, J., R. Francois, J.-M. Gherardi, L. Keigwin, and S. Brown-Leger, Collapse and rapid resumption of atlantic meridional circulation linked to deglacial climate changes, *Nature*, *428*(6985), 834–837, 2004.

Mellor, G., and L. Kantha, An ice-ocean coupled model, *J. Geophys. Res.*, *94*(C8), 10,937–10,954, 1989.

Mitchell, J. F., N. Grahame, and K. Needham, Climate simulations for 9000 years before present: seasonal variations and effect of the laurentide ice sheet, *Journal of Geophysical Research: Atmospheres (1984–2012)*, *93*(D7), 8283–8303, 1988.

Mügler, I., et al., A multi-proxy approach to reconstruct hydrological changes and holocene climate development of nam co, central tibet, *Journal of Paleolimnology*, *43*(4), 625–648, 2010.

Müller, J., G. Massé, R. Stein, and S. T. Belt, Variability of sea-ice conditions in the fram strait over the past 30,000 years, *Nat. Geosci.*, *2*(11), 772–776, 2009.

Notz, D., Challenges in simulating sea ice in earth system models, *Wiley Interdisciplinary Reviews: Climate Change*, *3*, 509–526, doi:10.1002/wcc.189, 2012.

Notz, D., F. A. Haumann, H. Haak, J. H. Jungclaus, and J. Marotzke, Arctic sea-ice evolution as modeled by max planck institute for meteorology's earth system model, *Journal of Advances in Modeling Earth Systems*, *5*(2), 173–194, doi:10.1002/jame.20016, 2013.

Oerlemans, J., Continental ice sheets and the planetary radiation budget, *Quaternary Res.*, *14*(3), 349–359, 1980.

Otto-Bliesner, B. L., E. C. Brady, G. Clauzet, R. Tomas, S. Levis, and Z. Kothavala, Last glacial maximum and holocene climate in ccsm3, *J. Clim.*, *19*(11), 2526–2544, 2006.

Owens, W., and P. Lemke, Sensitivity studies with a sea ice-mixed layer-pycnocline model in the weddel sea, *J. Geophys. Res.*, *95*(C6), 9527–9538, 1990.

Parkinson, C., and W. Washington, A large-scale numerical model of sea ice, *J. Geophys. Res.*, *84*(C1), 311–337, 1979.

Peltier, W., Global glacial isostasy and the surface of the ice-age earth: the ice-5g (vm2) model and grace, *Annu. Rev. Earth Planet. Sci.*, *32*, 111–149, 2004.

Polyakov, I., U. Bhatt, H. Simmons, D. Walsh, J. Walsh, and X. Zhang, Multidecadal variability of north atlantic temperature and salinity during the twentieth century, *J. Clim.*, *18*(21), 4562–4581, 2005.

Proshutinsky, A., D. Dukhovskoy, M.-L. Timmermans, R. Krishfield, and J. L. Bamber, Arctic circulation regimes, *Phil. Trans. R. Soc. A*, *373*(2052), 20140,160, 2015.

Raddatz, T., C. Reick, W. Knorr, J. Kattge, E. Roeckner, R. Schnur, K.-G. Schnitzler, P. Wetzel, and J. Jungclaus, Will the tropical land biosphere dominate the climate–carbon cycle feedback during the twenty-first century?, *Clim. Dyn.*, *29*(6), 565–574, 2007.

Rasmussen, T. L., and E. Thomsen, Holocene temperature and salinity variability of the atlantic water inflow to the nordic seas, *The Holocene*, *20*(8), 1223–1234, 2010.

Redi, M., Oceanic isopycnal mixing by coordinate rotation, *J. Phys. Oceanogr.*, *12*, 1154–1158, 1982.

Reick, C., T. Raddatz, V. Brovkin, and V. Gayler, Representation of natural and anthropogenic land cover change in MPI-ESM, *J. Adv. Model. Earth Syst.*, *5*(3), 459–482, 2013.

Renssen, H., H. Goosse, T. Fichefet, and J. Campin, The 8.2 kyr bp event simulated by a global atmosphere-sea, *Geophysical Research Letters*, *28*(8), 1567–1570, 2001.

Renssen, H., H. Goosse, and T. Fichefet, Modeling the effect of freshwater pulses on the early holocene climate: The influence of high-frequency climate variability, *Paleoceanography*, *17*(2), 10–1, 2002.

Renssen, H., H. Goosse, T. Fichefet, V. Brovkin, E. Driesschaert, and F. Wolk, Simulating the holocene climate evolution at northern high latitudes using a coupled atmosphere-sea ice-ocean-vegetation model, *Clim. Dyn.*, *24*(1), 23–43, 2005.

Renssen, H., H. Seppä, O. Heiri, D. Roche, H. Goosse, and T. Fichefet, The spatial and temporal complexity of the holocene thermal maximum, *Nature Geoscience*, *2*(6), 411–414, 2009.

Rimbu, N., G. Lohmann, J.-H. Kim, H. Arz, and R. Schneider, Arctic/north atlantic oscillation signature in holocene sea surface temperature trends as obtained from alkenone data, *Geophys. Res. Lett.*, *30*(6), 2003.

Roeckner, E., L. Dümenil, E. Kirk, F. Lunkeit, M. Ponater, B. Rockel, R. Sausen, and U. Schlese, The Hamburg version of the ECMWF model (ECHAM), *Tech. Rep.*, *13*, World Meteorol. Org., Geneva, Switzerland, 1989.

Royer, J., S. Planton, and M. Déqué, A sentitivity experiment for the removal of arctic sea ice with the french spectral general circulation model, *Clim. Dyn.*, *5*, 1–17, doi: 10.1007/BF00195850, 1990.

Rühlemann, C., S. Mulitza, G. Lohmann, A. Paul, M. Prange, and G. Wefer, Intermediate depth warming in the tropical atlantic related to weakened thermohaline circulation: Combining paleoclimate and modeling data for the last deglaciation, *Paleoceanography*, *19*(PA1025), PA1025, doi:10.1029/2003PA000948, 2004.

Schlesinger, M. E., and N. Ramankutty, An oscillation in the global climate system of period 65-70 years, *Nature*, (367), 723–726, 1994.

Schmidt, G. A., et al., Configuration and assessment of the GISS ModelE2 contributions to the CMIP5 archive, *J. Adv. Model. Earth Syst.*, *6*(1), 141–184, 2014.

Schneck, R., C. H. Reick, and T. Raddatz, Land contribution to natural CO2 variability on time scales of centuries, *J. Adv. Model. Earth Syst.*, *5*(2), 354–365, 2013.

Scholz, P., G. Lohmann, Q. Wang, and S. Danilov, Evaluation of a finite-element sea-ice ocean model (fesom) set-up to study the interannual to decadal variability in the deep-water formation rates, *Ocean Dyn.*, *63*(4), 347–370, 2013.

Scholz, P., D. Kieke, G. Lohmann, M. Ionita, and M. Rhein, Evaluation of labrador sea water formation in a global finite-element sea-ice ocean model setup, based on a comparison with observational data, *Journal of Geophysical Research: Oceans*, *119*(3), 1644–1667, 2014.

Semmler, T., R. McGrath, and S. Wang, The impact of arctic sea ice on the arctic energy budget and on the climate of the northern mid-latitides, *Clim. Dyn.*, *39*, 2675–2694, doi:10.1007/s00382-012-1353-9, 2012.

Semtner, A., A model for the thermodynamic growth of sea ice in numerical investigations of climate, *J. Phys. Oceanogr.*, *6*(3), 379–389, 1976.

Sidorenko, D., Q. Wang, S. Danilov, and J. Schröter, Fesom under coordinated ocean-ice reference experiment foring, *Ocean Dyn.*, *61*, 881–890, doi:10.1007/s10236-011-0406-7, 2011.

Sidorenko, D., et al., Towards multi-resolution global climate modeling with echam6-fesom. part i: Model formulation and mean climate, *Clim. Dyn.*, doi:10.1007/s00382-014-2290-6, 2014.

Smedsrud, L., Grease-ice thickness parameterization, *Ann. Glaciol.*, *52*(57), 77–82, 2011.

Smedsrud, L., and R. Skogseth, Field measurements of arctic grease ice properties and processes, *Cold Reg. Sci. Technol.*, *44*(3), 171–183, 2006.

Sowers, T., R. B. Alley, and J. Jubenville, Ice core records of atmospheric n2o covering the last 106,000 years, *Science*, *301*(5635), 945–948, 2003.

Steele, M., Sea ice melting and floe geometry in a simple ice-ocean model, *Journal of Geophysical Research: Oceans (1978–2012)*, *97*(C11), 17,729–17,738, 1992.

Steele, M., and T. Boyd, Retreat of the cold halocline layer in the arctic ocean, *Journal of Geophysical Research: Oceans*, *103*(C5), 10,419–10,435, 1998.

Stevens, B., et al., Atmospheric component of the MPI-M Earth System Model: ECHAM6, *Adv. Model. Earth Syst.*, *5*(2), 146–172, 2013.

Stommel, H., Thermohaline convection with two stable regimes of flow, *Tellus*, *13*(2), 224–230, 1961.

Storch, J.-S. v., C. Eden, I. Fast, H. Haak, D. Hernández-Deckers, E. Maier-Reimer, J. Marotzke, and D. Stammer, An estimate of the lorenz energy cycle for the world ocean based on the STORM/NCEP simulation, *J. Phys. Oceanogr.*, *42*(12), 2185–2205, 2012.

Sun, C., J. Li, and F.-F. Jin, A delayed oscillator model for the quasi-periodic multi-decadal variability of the nao, *Climate Dynamics*, *45*(7-8), 2083–2099, 2015.

Sundqvist, H., E. Berge, and J. E. Kristjánsson, Condensation and cloud parameterization studies with a mesoscale numerical weather prediction model, *Mon. Weather Rev.*, *117*(8), 1641–1657, 1989.

Taylor, K. E., R. J. Stouffer, and G. A. Meehl, An overview of cmip5 and the experiment design, *Bull. Amer. Meteor. Soc.*, *93*(4), 485–498, 2012.

Thompson, D. W., and J. M. Wallace, Regional climate impacts of the northern hemisphere annular mode, *Science*, *293*(5527), 85–89, 2001.

Thornalley, D. J., H. Elderfield, and I. N. McCave, Holocene oscillations in temperature and salinity of the surface subpolar north atlantic, *Nature*, *457*(7230), 711–714, 2009.

Timmermann, R., S. Danilov, J. Schröter, C. Böning, D. Sidorenko, and K. Rollenhagen, Ocean circulation and sea ice distribution in a finite element global sea ice-ocean model, *Ocean Model.*, *27*, 114–129, 2009.

Vancoppenolle, M., T. Fichefet, H. Goosse, S. Bouillon, G. Madec, and M. A. M. Maqueda, Simulating the mass balance and salinity of arctic and antarctic sea ice. 1. model description and validation, *Ocean Model.*, *27*(1-2), 33–53, 2010.

Vavrus, S., J. Walsh, W. Chapman, and D. Portis, The behavior of extreme cold air outbreaks under greenhouse warming, *International Journal of Climatology*, *26*(9), 1133–1147, 2006.

Visbeck, M., H. Cullen, G. Krahmann, and N. Naik, An ocean model's response to north atlantic oscillation-like wind forcing, *Geophysical research letters*, *25*(24), 4521–4524, 1998.

Visbeck, M., E. P. Chassignet, R. G. Curry, T. L. Delworth, R. R. Dickson, and G. Krahmann, The ocean's response to north atlantic oscillation variability, *The North Atlantic Oscillation: climatic significance and environmental impact*, pp. 113–145, 2003.

Voldoire, A., et al., The CNRM-CM5. 1 global climate model: description and basic evaluation, *Clim. Dyn.*, *40*(9-10), 2091–2121, 2013.

Von Grafenstein, U., H. Erlenkeuser, J. Müller, J. Jouzel, and S. Johnsen, The cold event 8200 years ago documented in oxygen isotope records of precipitation in europe and greenland, *Climate dynamics*, *14*(2), 73–81, 1998.

Wang, Q., S. Danilov, D. Sidorenko, R. Timmermann, C. Wekerle, X. Wang, T. Jung, and J. Schröter, The finite element sea ice-ocean model (fesom): formulation of an unstructured-mesh ocean general circulation model, *Geosci. Model Dev. Discuss.*, *6*, 3893–3976, 2013.

Wang, Z., Y. Lu, D. G. Wright, and F. Dupont, Sea ice sensitivity to the parameterisation of open water area, *J. Oper. Oceanogr.*, *3*(2), 3–9, 2010.

Watanabe, S., et al., MIROC-ESM 2010: Model description and basic results of CMIP5-20c3m experiments, *Geosci. model dev.*, *4*, 845–872, 2011.

Weber, S., The impact of orbital forcing on the climate of an intermediate-complexity coupled model, *Global and Planetary Change*, *30*(1), 7–12, 2001.

Weber, S., and J. Oerlemans, Holocene glacier variability: three case studies using an intermediate-complexity climate model, *The Holocene*, *13*(3), 353–363, 2003.

Weber, S., T. Crowley, and G. Van der Schrier, Solar irradiance forcing of centennial climate variability during the holocene, *Climate Dynamics*, *22*(5), 539–553, 2004.

Wei, W., and G. Lohmann, Simulated atlantic multidecadal oscillation during the holocene, *J. Clim.*, *25*(20), 6989–7002, 2012.

Winsor, P., and G. Björk, Polynya activity in the arctic ocean from 1958-1997, *J. Geophys. Res.*, *105*(C4), 8789–8803, 2000.

Woollings, T., A. Hannachi, and B. Hoskins, Variability of the north atlantic eddy-driven jet stream, *Quarterly Journal of the Royal Meteorological Society*, *136*(649), 856–868, 2010.

Wu, T., R. Yu, and F. Zhang, A modified dynamic framework for the atmospheric spectral model and its application, *J. Atmos. Sci.*, *65*(7), 2235–2253, 2008.

Wu, T., R. Yu, F. Zhang, Z. Wang, M. Dong, L. Wang, X. Jin, D. Chen, and L. Li, The Beijing Climate Center atmospheric general circulation model: description and its performance for the present-day climate, *Clim. Dyn.*, *34*(1), 123–147, 2010.

Xu, X., M. Werner, M. Butzin, and G. Lohmann, Oceanic d18o variation and its relation to salinity in the mpi-om ocean model, *Earth System Science: Bridging the Gaps between Disciplines Perspectives from a Multi-disciplinary Helmholtz Research School*, pp. 70–74, 2013.

Yukimoto, S., et al., A new global climate model of the Meteorological Research Institute: MRI-CGCM3-model description and basic performance, *J. Meteorol. Soc. Jpn.*, *90*(0), 23–64, 2012.

Zhang, J., and D. Rothrock, Effect of sea ice rheology in numerical investigations of climate, *Journal of Geophysical Research: Oceans*, *110*(C8), 2005.

Zhang, R., Can the atlantic ocean drive the observed multidecadal variability in northern hemisphere mean temperature?, *Geophys. Res. Lett.*, *34*(02709), doi: 10.1029/2006GL028683, 2007.

Zhang, R., Coherent surface-subsurface fingerprint of the atlantic meridional overturning circulation, *Geophys. Res. Lett.*, *35*(L20705), doi:10.1029/2008GL035463, 2008.

Zhang, R., Mechanisms for low-frequency variability of summer arctic sea ice extent, *Proceedings of the National Academy of Sciences*, *112*(15), 4570–4575, 2015.

Zhang, X., G. Lohmann, G. Knorr, and C. Purcell, Abrupt glacial climate shifts controlled by ice sheet changes, *Nature*, 2014.

Zhang, Y., H. Renssen, and H. Seppä, Effects of melting ice sheets and orbital forcing on the early holocene warming in extratropical northern hemisphere, *Climate of the Past Discussions*, *11*, 5345–5399, 2015.

Zhao, Y., et al., A multi-model analysis of the role of the ocean on the african and indian monsoon during the mid-holocene, *Clim. Dyn.*, *25*(7-8), 777–800, 2005.

Zheng, W., and Y. Yu, Paleoclimate simulations of the mid-holocene and last glacial maximum by fgoals, *Adv. Atmos. Sci.*, *30*, 684–698, 2013.

Acknowledgements

I would like to acknowledge everyone who has assisted me throughout my doctoral studies over the years. I would first like to acknowledge my adviser, Prof. Gerrit Lohmann, for agreeing to serve as my adviser and for his patience and feedback during my PhD period and as I completed my dissertation. Additionally, I would like to thank all of my committee members for agreeing to serve on my dissertation committee. I truly appreciate all of their time and assistance as I navigated this process!

I want to thank Dmitry Sidorenko, Patrick Scholz and Qiang Wang for their technical help with the model ECHAM6-FESOM, and thank Monica Ionita-Scholz, Jiping Liu for their helpful discussions, and Stefanie Klebe for her friendly review. I also want to thank my colleagues from the Paleoclimate Dynamic group, for the inspiring working environment.

A very special thanks is due to my husband Hu Yang for his patience, assistance, support and faith in me. Without his continuous moral support, encouragement and love I could have never completed this dissertation. I am also grateful to my little daughter Coco, who motivated me with her enduring smile and love.

Further acknowledgement and thanks is due to my parents for their encouragement and continued support over the years and their enthusiasm as I neared my goal.

This work is funded by China Scholarship Council (CSC) and Helmholz project PACES.